THE HONG KONG POLYTECHNIC UNIVERSITY
香港理工大學
Pao Yue-kong Library
包玉剛圖書館

Copyright Undertaking

This thesis is protected by copyright, with all rights reserved.

By reading and using the thesis, the reader understands and agrees to the following terms:

1. The reader will abide by the rules and legal ordinances governing copyright regarding the use of the thesis.
2. The reader will use the thesis for the purpose of research or private study only and not for distribution or further reproduction or any other purpose.
3. The reader agrees to indemnify and hold the University harmless from and against any loss, damage, cost, liability or expenses arising from copyright infringement or unauthorized usage.

IMPORTANT

If you have reasons to believe that any materials in this thesis are deemed not suitable to be distributed in this form, or a copyright owner having difficulty with the material being included in our database, please contact lbsys@polyu.edu.hk providing details. The Library will look into your claim and consider taking remedial action upon receipt of the written requests.

Pao Yue-kong Library, The Hong Kong Polytechnic University, Hung Hom, Kowloon, Hong Kong

http://www.lib.polyu.edu.hk

RESEARCH ON CONTROL STRATEGY FOR PMSM DRIVES BASED ON FINITE SET MODEL PREDICTIVE CONTROL

XIAOMEI TANG

PhD

The Hong Kong Polytechnic University

2025

The Hong Kong Polytechnic University

Department of Electrical and Electronic Engineering

Research on Control Strategy for PMSM Drives Based on Finite Set Model Predictive Control

Xiaomei Tang

A thesis submitted in partial fulfillment of the requirements for the degree of Doctor of Philosophy

April 2025

CERTIFICATE OF ORIGINALITY

I hereby declare that this thesis is my own work and that, to the best of my knowledge and belief, it reproduces no material previously published or written, nor material that has been accepted for the award of any other degree or diploma, except where due acknowledgment has been made in the text.

______________________ (Signed)

Xiaomei TANG (Name of student)

ABSTRACT

The Permanent Magnet Synchronous Motor (PMSM) has garnered extensive research and application in fields such as the defense industry and transportation due to its advantages, including high efficiency, high power density, high torque-to-current ratio, and a wide speed regulation range. Concurrently, with the advancement of powerful and fast microprocessors, Model Predictive Control (MPC) has emerged as a promising control strategy for AC motors. MPC features a straightforward control structure, excellent dynamic response, and the ability to easily account for system nonlinearities and constraints, making it particularly suitable for achieving high-performance control of PMSMs. However, the application of existing MPC algorithms to PMSM control presents a series of challenges, such as significant output ripples and elevated common-mode voltages, which can lead to decreased prediction accuracy and control performance. To address these issues, this thesis focuses on PMSMs as the research subject, employing finite set predictive control system theory and comprehensively applying modern control concepts such as hysteresis to conduct in-depth research on high-performance current control strategies for electric drives. The main contributions of this work are summarized as follows:

Firstly, the mathematical models of PMSM and traditional two-level inverter are introduced, and the basic principle and solution process of finite-set MPC (FS-MPC) are described in detail. FS-MPC is combined with PMSM current control, and the entire controller replaces the current loop of traditional field-oriented control, and the cost

function is designed according to the current tracking reference value. Building on this classical strategy's simulation validation, the primary challenges and limitations are discussed through theoretical derivation, encompassing dynamic and steady-state effects, output ripples, and online computation requirements.

Secondly, to address the non-fixed and elevated switching frequency issues associated with FS-MPC under various operational conditions, a multi-vector switching sequence optimization is introduced into the classical control strategy. Additionally, two voltage generation methods that avoid utilizing zero vectors have been designed to suppress common-mode voltage and mitigate adverse effects such as shaft currents and electromagnetic interference. Experimental results demonstrate that this strategy can effectively accommodate the motor's varied operational states, combining the favorable steady-state performance of the multi-vector strategy with the rapid transient response of the single-vector strategy; specific pulse generation methods can effectively eliminate common-mode voltage.

Furthermore, in light of the prolonged computation times and high implementation complexities associated with the three-level FS-MPC control strategy in practical hardware execution, a simplified sub-sector division has been established. A rapid optimization search method has been devised by designing a novel cost function and narrowing the traditional enumeration optimization search range. Comparative simulations with typical schemes from the literature indicate that the proposed approach is both simple to implement and capable of quickly tracking given values under dynamic conditions.

Additionally, employing a pre-refined candidate vector set as the core framework, an enhanced multi-vector control strategy is proposed, which achieves neutral point potential balancing and common-mode voltage suppression. This strategy also considers optimal dwell times and the composite effects of reconstructed vectors across different sectors. Experimental results validate that this scheme can achieve satisfactory dynamic and static performance within a short execution time, while lowering the switching frequency of the three-level inverter and enhancing the operational efficiency of the drive system.

Finally, a set of coherent voltage vectors (CVVs) with movable starting points is introduced to replace the basic candidates. The pulse train of the optimal CVV is generated by single-carrier modulation, and capacitor charge balancing in different sectors can be included in the zero-sequence component injection. The proposed CVV-MPC is characterized by simple implementation and satisfactory performance under low switching frequency. Comparative experiments are conducted to verify the effectiveness and superiority of the proposed method.

PUBLICATION ARISING FROM THE THESIS

[1] **X. Tang**, S. Niu, " Coherent Vector Based Model Predictive Control with Zero-Sequence Component Injection for Three-Level NPC Inverter Fed PMSM Drives," in IEEE Transactions on Power Electronics. (accept)

[2] **X. Tang**, S. Niu, K. T. Chau, X. Yuan and W. L. Chan, "Model Predictive Control of Three-Level NPC Inverter-Fed PMSM Drives Based on a Novel Vector-Selection Scheme," in IEEE Journal of Emerging and Selected Topics in Power Electronics, doi: 10.1109/JESTPE.2024.3520912.

[3] **X. Tang**, X. Yuan, S. Niu and K. T. Chau, "High-Efficient Multivector Model Predictive Control With Common-Mode Voltage Suppression," in IEEE Journal of Emerging and Selected Topics in Power Electronics, vol. 12, no. 3, pp. 2674-2685, June 2024, doi: 10.1109/JESTPE.2024.3380636.

[4] **X. Tang**, S. Niu and X. Yuan, "Low Complexity Model Predictive Control Method for Three-Level Converters with Fixed Switching Frequency Mode," IECON 2023- 49th Annual Conference of the IEEE Industrial Electronics Society, Singapore, Singapore, 2023, pp. 1-6, doi: 10.1109/IECON51785.2023.10312318.

[5] H. Lin, S. Niu, Y. Chen, W. Wang, **X. Tang**, "Three-Stage Duty Cycle-Based Deadbeat Predictive Torque Control for Three-Phase SPMSMs With CMV Reduction," in IEEE Transactions on Power Electronics, vol. 38, no. 9, pp. 11385-11398, Sept. 2023, doi: 10.1109/TPEL.2023.3288184.

[6] **X. Tang**, S. Niu and K. T. Chau, " Model Predictive Control with Single-Phase Current Sensor of Three-Level NPC Inverter-Fed PMSM Drives Considering Current Reconstruction," in IEEE Transactions on Power Electronics. (submitted)

ACKNOWLEDGMENTS

I would like to express my heartfelt gratitude to all those who have supported me throughout my PhD journey. This work would not have been possible without the guidance, encouragement, and assistance of many individuals.

First and foremost, I would like to extend my deepest appreciation to my chief supervisor, Professor Shuangxia Niu. Your invaluable guidance, insightful feedback, and unwavering support have been instrumental in shaping my research and academic growth. Your passion for motor design and control has inspired me to push the boundaries of my knowledge and strive for excellence. Your constructive feedback, coupled with your encouraging demeanor, provided me with the confidence to pursue innovative ideas and challenges. Thank you for your patience and for believing in my potential, even during the most demanding moments of this journey.

I would like to extend my heartfelt thanks to Dr. Xin Yuan, Professor K.T. Chau, Professor Weinong Fu, Dr. Xiaodong Zhang and Dr. Xing Zhao. Thank you for your meticulous attention to detail and for challenging me to refine my ideas with critical precision. Your deep insights and research skills have had a profound impact on my work. Your commitment to academic rigor has inspired me greatly. Your selfless assistance and wealth of experience have been instrumental in my academic growth.

I also wish to acknowledge my exceptional colleagues and friends in our research group, most notably, Dr. Mingyuan Jiang, Dr. Hongjian Lin, Dr. Yixiao Luo, Dr. Sigao Wang, Dr. Huihuan Wu, Dr. Weiyu Wang, Dr. Yao Wang, Dr. Zhenghao Li, Dr. Jifu

Jiang, Dr. Litao Dai, Dr. Zhenyao Sun, Dr. Mingjin Hu, Dr. Zekai Lyu, Dr. Yuanxi Chen, Dr. Yanding Bi, Dr. Jiahui Huang, Dr. Songyan Niu, Mr. Liang Li, , Mr. Ziqi Huang, Ms. Feifan Ni, Mr. Wenjie Wu, Mr. Junkai Wen, Mr. Hui Wu, Mr. Longfei Xiao,Mr. Zhiwei Xue, Ms. Shiyue Zheng, Ms. Lin Liu, Mr. Hang Yin and Mr. Yuxuan Liu. Each of you has played a pivotal role in creating an inspiring atmosphere that has fostered my growth as a researcher. Your diverse perspectives and collaborative nature have made this journey truly remarkable.

Finally, I want to extend my deepest gratitude to my family and friends, whose unwavering love and encouragement have been my steadfast anchor. Your belief in my abilities has provided me with the strength to overcome obstacles and pursue my dreams with confidence. To my family, thank you for your endless support and sacrifices, and for always cheering me on.

This thesis is not merely a reflection of my efforts but rather a culmination of the collective wisdom and support of those around me. Thank you all for being integral to this journey.

TABLE OF CONTENTS

LIST OF FIGURES

CHAPTER 1. INTRODUCTION

1.1. Research Background

Over the past decades, high-performance servo drives have been increasingly used in a variety of fields, thanks to greatly improved servo control performance, which has effectively increased productivity [1]. Among them, Permanent Magnet Synchronous Motor (PMSM) is characterized by high power density, wide speed range, and the ability to provide large torque and occupy a small size, which is suitable for various industrial drives [2]-[6]. As a result, PMSMs can be used in a wide variety of applications, including general purpose industrial drives [7], precision machine tools, pumps and fans, as well as in environments with stringent dimensional and environmental requirements, such as automotive and aerospace [8],[9]. High performance servo control requires precise control of motor speed, current and torque [10].

While the PMSM structure is constantly being optimized and innovated with specific application scenarios [11]-[14], PMSM high-performance control technology is also developing rapidly [15]. Currently, the two control schemes that are relatively mature and have been widely used in industry are field-oriented vector control strategy (FOC) and direct torque control strategy (DTC) [16]-[19]. FOC mainly realizes the independent control of the stator current excitation component and the torque component through coordinate transformation [20], thereby achieving the decoupling of magnetic field and torque control [21]. Its specific implementation generally adopts a multi-loop cascade structure based on PI controller, which has good steady-state tracking performance [22], but has defects such as integral saturation, difficulty in handling system constraints, and difficulty in adjusting controller parameters during multi-objective collaborative control, making it difficult to guarantee dynamic performance in the full speed range [23]. Compared with FOC, DTC directly controls the torque and flux [24], uses the torque and flux errors as the input of the preset switching table, and directly outputs the appropriate switching state [25]. It has a faster dynamic response speed, but there are problems such as large torque and flux fluctuations and non-fixed switching frequency [26]-[29].

In traditional control scenarios, the control performance indicators of PMSM mainly focus on its dynamic response speed and steady-state error [30]-[33]. At present, the requirements of emerging industries for PMSM control performance are more diversified, including system speed regulation range, operating efficiency, noise and vibration, fault diagnosis, *etc* [34]-[39]. It is difficult to meet so many requirements only through hardware [40]. Therefore, more and more advanced control technologies with relatively complex algorithms and large computational complexity have been introduced into the field of motor control by domestic and foreign scholars for research, such as adaptive control [41], fuzzy control [42], neural network control [43], model predictive control, *etc* [44].

Among them, Model Predictive Control (MPC) has garnered significant attention in recent years [45]-[49]. Compared to other control methods, MPC is capable of integrating the characteristics of power converters and drive systems within hybrid nonlinear systems [50], as well as managing a finite number of switching states and constraint conditions, thereby simplifying the control algorithms [51]-[53]. Currently, MPC has been applied in the field of motor control and has achieved notable results [54]. However, in general, the application of MPC algorithms in practical systems is still in its nascent stages. Specifically, in the context of Permanent Magnet Synchronous Motors (PMSMs), further research is needed to enhance control performance, improve system stability [55], and adapt to varying parameters [56]-[58]. Therefore, the continued exploration of MPC applications in motor control is very promising [59]-[64].

The control technology for two-level inverters has become relatively mature, with widespread product applications in the low-voltage, low-power variable frequency domain [65], demonstrating certain technical advantages and market share [66]-[70]. As the demand for installed capacity continues to grow, enterprises are increasingly adopting the method of stacking multiple two-level inverters at the input of high-power variable frequency speed control systems [71]. This approach not only reduces the overall efficiency of the system but also compromises reliability and necessitates the use of expensive, energy-consuming transformers [72]-[74]. It is evident that the development of two-level inverters has become insufficient to meet these requirements; therefore, multi-level inverters have emerged as a key solution to address these challenges [75]-[78]. Compared with the traditional two-level inverter, the total harmonic distortion (THD) of the output waveform of the three-level neutral-point-clamped (3L-NPC) inverter is reduced under the same switching frequency [79]. This is because the output voltage waveform of the three-level inverter is ladder-shaped and closer to a sine wave [80]. At the same time, multi-level inverters also have the advantages of small voltage change rate *dv*/*dt* and minor voltage stress of power devices [81]-[83]. Therefore, 3L-NPC is widely used in the field of high-voltage, high-capacity, and high-accurate motor drive [84].

1.2. State of The Art in MPC Strategies

There are various forms of MPC strategies in drive systems, among which the one regarded as the base initiator is the single-vector based MPC. In this category of strategies, only one basic voltage vector is selected from a finite number of candidates sets in each control cycle [85]. The restricted utilization of voltage vectors leads to the switching frequency of the converter output being unfixed. In the two-stage optimization-based MPC scheme of [86], the interleaved carriers are applied to conveniently achieve the fixed switching frequency. While in [59] and [87], the suitable switching sequences are designed and utilized as candidates for optimal pools. Furthermore, a single vector-based approach causes inaccurate tracking with the desired value which is far from satisfying performance requirements [60]. To address this issue, a considerable amount of research work has been carried out, which can be summarized into two paths: one is to expand the candidate sets with virtual vectors, and the other is discrete space vector modulation [88]-[90]. Essentially, two or three different vectors are applied in one entire control period to synthesize the vector circle more accurately.

In [91], a method of PMSM drive that adopted one nonzero vector and one unrestricted vector is presented. The latter vector is confirmed in a border range and the novel cost function is a kind of direct voltage selection mode. In order to achieve better steady-state performance, three vectors are allocated symmetrically, and the optimal vector duration ratio is calculated [62]. In [92], 12 new virtual vectors were constructed by basic voltage vectors to improve the accuracy of converter output. The duty cycle scheme is formed by introducing a zero vector to adjust the magnitude of the virtual vector.

The above-mentioned approaches can reduce the tracking error and current THD, but whether based on multiple vectors or virtual vectors, the use of zero vectors is inevitable. The similarity between these different variants of MPC is that they are required to determine not only the optimal combination of output variables but also every variable's action time, which is computationally intensive.

1.3. State of The Art in Three-level Inverter Motor Drive System

The situation will be more complex when MPC is extended to the three-level inverter topology, and a number of strategies have been proposed for this scenario. In the conventional FS-MPC introduced by Rodriguez *et al.* [93], all 27 switching actions generated by the 3L-NPC inverter are predicted by the discrete-time model in each control cycle. In the next period, the optimal voltage vector that minimizes the cost function will be applied to the control system. Therefore, FS-MPC often consumes excessive computational time and thus deteriorate system dynamic performance. Several solutions have been adopted to overcome the drawbacks. Zhang *et al.* [72] proposed the deadbeat-based method, which avoids predictions for 27 stator voltage or current in each control cycle. However, the computational time is still considerable when carrying out cost function calculations.

All the aforementioned methods adopt only one voltage vector in one entire control cycle, which leads to unfixed switching frequency and large current ripple. Accordingly, a dual-vector control mode is applied in [94]. It enhanced the overall inverter performance based on the current error area minimization. Xiong *et al*. constructed virtual vectors and employed a discrete time disturbance observer, which achieved good steady-state and dynamic performance [95]. Alhosaini *et al*. presented the modulation of discrete space vectors and effectively reduced the output current ripples [96].

To optimize the duty cycle for each of the 24 redivided sectors, Donoso *et al.* made use of the numerical values of cost functions [97]. However, these MPC strategies that go beyond taking a single vector have a complex vector evaluation process that also requires calculating the duration of each vector combination. To improve the computational efficiency, a preselection scheme is proposed to select the optimal vectors, and the evaluation structure is rebuilt in [73]. Two-stage optimization based on virtual VVs is employed in [98] to reduce the computation burden. In [57], the deadbeat current control principle is introduced to eliminate the iterative computations for a nine-phase open-end winding PMSM.

For a 3L-NPC inverter, operating with the unbalanced neutral point potential (NPP) will affect the reliability and lifetime of the PMSM drive system. To handle this key issue, a hexagon candidate region FS-MPC is proposed in [72], and the NPP balancing is incorporated into cost function calculation. However, the weighting factors are required to be fine tuned by trial and error, which consumes a lot of time and sacrifices the fast dynamic response. Yang *et al*. balanced the NPP by selecting proper redundant small voltage vectors [99]. The candidate voltage vectors to be evaluated are effectively reduced, and the weighting factors are eliminated as well. Yang *et al*. applied one virtual and three real vectors in one control cycle [100]. NPP balance is achieved by duration time adjustment of virtual and redundant vectors. Zhou *et al*. decoupled the control process into two stages in each control period and considered the nonlinearity of the voltage vectors caused by the unbalanced NPP [101].

Another critical issue with different types of inverters driving electric machines is that they inherently produce a common-mode voltage (CMV). If large CMV is presented in the PMSM drive system, overvoltage stress to the winding insulation is raised, and electromagnetic interference (EMI) is generated with neighboring devices. EMI causes high-frequency overload bearing current, which needs to be suppressed to promote 3L-NPC inverter performance. The hardware increment, such as separate rectifiers and filters, will reduce overall system efficiency and increase maintenance costs [102], [103].

In the software-based technique, scholars have conducted rich research on suppressing CMV through control algorithms. In [61], the CMV suppression item is added to the cost function of MPC, but this soft screening mechanism of the voltage vector cannot wholly suppress the CMV spike. Nevertheless, the designed cost function causes a compromise of the main control target and reduces the current and torque performance. In the MPC scheme of [104], only 6 nonzero basic vectors are used, and the zero vectors are abandoned; thereby, the CMV is suppressed. However, its current and torque fluctuations are increased compared with the conventional MPC. In [105], two nonzero voltage vectors are selected from the control set and utilized in one control cycle. However, due to the reduced number of usable switching states, it is only possible to synthesize virtual vectors with larger amplitudes (larger than $U_{dc}/3$).

In [106], two active vectors in opposite directions as equivalent zero vectors, replacing the zero vectors in the conventional three-vector synthesis method [62], which can better suppress current and torque ripples. However, four nonzero vectors are used to synthesize the target voltage vector, which leads to a high switching frequency of the converter [107], significant loss, and difficulty in heat dissipation. Therefore, this algorithm is subject to these restrictions on various occasions. Qin *et al*. [108] divided space vectors into large, medium, and zero vectors and selected vectors corresponding to one sixth CMV of the DC-link voltage. In [109], only the non zero vectors are applied, and the dead-time effects of the inverter are considered.

However, in the above-mentioned CMV elimination schemes, the NPP balancing of NPC-type inverter is not taken into consideration. The most common solution of this issue is redundant vector duration time adjustment combined with space vector modulation theory [74]. Liu *et al*. [110] proposed a double signal PWM technique that can control the NPP and reduce CMV simultaneously. However, the switching losses inside the inverter are increased. In [104], a series of virtual vectors are synthesized, and appropriate redundant vectors are selected based on the neutral point potential deviation. However, the number of candidate vectors is large, and the output is not stable enough. Yang *et al*. [111]– [113] added NPP error to the cost function as a constraint and solved the task of selecting the corresponding weighting factors for the multi-objective cost function. However, as mentioned above, weighting factor design in the cost function is complicated, especially when the number of control objectives increases.

Although these recently emerged studies have been able to enhance steady-state performance while balance neutral point voltage, the computational cost will further increase. For example, if double vectors are applied in the entire control cycle, there are totally 729 (27^2) possible combinations to be enumerated and evaluated. When the consideration of neutral voltage balance is included, the complexity of this assumed double-vector strategy will increase exponentially. Complex formulation to solve the optimization problem will deteriorate the system's dynamic performance and hinder its practical application.

1.4. Research Motivation and Main Work

So far, to reduce the CMV without using hardware devices or weighting factors, the existing MPC studies adopt multiple voltage vectors to synthesize the reference vector [114]. However, the cost of the current methods is to sacrifice the fast response capability, and the switching frequency and switching loss are higher. How to realize the tradeoff between CMV suppression and the full range of dynamic and static control effects has become a challenge to be solved. This thesis is motivated toward the development of a high-efficient multivector MPC method for suppressing CMV. It combines the advantages of the one optimal vector FS-MPC method and the multivector synthesis method based on the equivalent zero vector without causing much rise in converter switching frequency. The main contributions of this thesis can be listed as follows.

1) The proposed method's high efficiency is first reflected in quickly judging the dynamic status and maximum output of the inverter. The existing indicators for judging the motor working conditions are the q-axis current slopes [90], which calculation is complex and time-consuming. This thesis creatively obtains the reference voltage amplitude for dynamic analysis and the single-vector method ensures maximum output range of the inverter. The experimental results demonstrate that the proposed method can achieve fast tracking when the speed and load change suddenly.

2) A novel multivector modulation scheme is designed to ensure that the drive system maintains highly efficient operation during the steady state. Previous studies fail to integrate switching sequences optimized and voltage vector selection [92], the phase angle variation mechanism is also not fully utilized in the design. The proposed method not only limits multiphase jump, but also requires no action between cycles,

and the number of actions within the cycle is fixed. Experiments prove that the proposed method achieves smooth and accurate output at a lower switching frequency.

3) Under various operating conditions, this thesis adopts a highly efficient CMV suppression strategy without zero vectors. In steady-state, two adjacent vectors and two nonadjacent vectors are selected from the candidate set and arranged into a specific order. Superior to the approach in [97], zero vectors are not simply abandoned but managed to be synthesized efficiently. It is experimentally verified that the dynamic and steady-state outputs are not sacrificed while completely restricting the CMV within $\pm U_{dc}/6$.

Existing three-level FS-MPC methods usually design the cost function and traverse the candidate vectors to find the optimization. However, compared to the two-level inverter system, which has only 8 voltage vectors, there are 27 basic voltage vectors, even without considering the CMV and NPP imbalance features. Furthermore, in the $\alpha\beta$-plane, voltage vectors at the same position may correspond to different CMV amplitudes and multiple neutral point currents [115], [116]. To fill the abovementioned gap, this thesis simplifies the process of voltage vectors selection and takes advantage of their CMV and NPP attributes. The main contributions of this work are as follows:

1) Since the three-level inverters provide abundant voltage vectors, regarding the computational burden of the system [102], an efficient mapping rule is introduced to narrow the candidate area into sub-hexagons. Numerical prediction and optimization

stages are omitted, and a substantial amount of calculation time is saved. The vector operation time is determined by the cost function so as to minimize the tracking error.

2) The proposed scheme does not directly exclude the basic vectors with large CMV amplitudes [117], but rather reconstructs them into a set of vectors with equivalent outputs based on the current situation and regulation requirements. Then, in conjunction with the other vectors in the sub-hexagon at which they are located, the CMV suppression does not affect the other control effects in the vast majority of cases.

3) Without the need to model DC-bus capacitor charging and discharging, nor utilizing the opposite characteristics of the redundant vectors [105], a hysteresis controller is comprehensively designed based on the multiple characteristics of the space voltage vectors. It fully mobilizes various voltage vector resources and expands the bidirectional range to non-redundant vectors to collaboratively suppress NPP fluctuations and CMV.

1.5. Thesis Outline

This thesis primarily focuses on the design of a current inner loop controller for PMSM based on the FS-MPC theory, aimed at improving the shortcomings of traditional PI controllers, such as slow dynamic response and difficulties in parameter tuning. Furthermore, it conducts an in-depth analysis of the issues associated with the sensitivity of traditional FS-MPC to model parameters and the significant output current ripple observed in conventional two-level drive systems. Relevant improvement strategies are proposed to address these shortcomings, and the effectiveness of these strategies is verified through simulations and experiments. The structure of this thesis is organized as follows:

Chapter 1 introduces the research background and significance of the topic, summarizing several commonly used control strategies for PMSMs. It reviews the development of predictive control and the current state of FS-MPC research, as well as its application directions, and concludes with a brief overview of the main research contributions of this thesis.

Chapter 2 presents the characteristics of PMSMs, focusing on the surface-mounted PMSM as the subject of study. It includes a mathematical modeling analysis conducted in the synchronous rotating coordinate system. The basic principles and control procedures of FS-MPC are introduced, with its application to the current loop discussed to enhance the dynamic performance of the system. The chapter concludes with the simulation setup and analysis of a single-vector control system.

Chapter 3 briefly introduces the deadbeat principle of reference voltage vector calculation and provides a detailed introduction to the causes of CMV. To address the issue of adjusting control strategies under different operating conditions in traditional FS-MPC, the relationship between the motor's rotational sectors and the switching of phase current is derived. Based on this, a multi-vector MPC utilizing specific vector switching rules is proposed, which improves the control performance of the system in steady and dynamic conditions. The chapter also details the construction of the experimental platform and comparative analysis.

Chapter 4 introduces the basic topology of the 3L-NPC inverter and its space vector distribution in the PMSM drive system. To alleviate the computational burden, a novel position determination method is proposed, which maps the reference voltage vector onto sub-hexagons, referred to as RFS-MPC. Simulations demonstrate that this method simplifies the optimization process while maintaining superior control performance

Chapter 5 discusses the principles, calculation methods, and hazards of neutral-point potential (NPP) and CMV generation. It then presents a combined suppression method for CMV and NPP based on voltage vector reconstruction. This method is not only flexible in control but also reduces parameter dependence through the proposed hysteresis strategy. An experimental hardware platform is established, and the proposed control method is verified experimentally, demonstrating its correctness and effectiveness.

Chapter 6 presents the proposed CVV-MPC method, including delay compensation, calculation of coherent voltage vectors, neutral point capacitor voltage balance, and generation of switching signals. The experimental studies and comparative analysis of different MPC methods are given, and the conclusions are drawn.

Chapter 7 summarizes the work completed in this thesis, highlights the limitations encountered during the research, and offers perspectives for future research endeavors.

CHAPTER 2. MODELING AND OPERATION MECHANISM ANALYSIS OF PERMANENT MAGNET SYNCHRONOUS MOTOR MODEL PREDICTIVE CONTROL

2.1. Introduction

The focus of this thesis is on permanent magnet synchronous motor (PMSM) systems driven by two-level and three-level voltage source inverters. The motors are controlled with various constraints on the operation process, such as switching frequency, current error, etc., in addition to the requirements on steady state performance and dynamic response. It is difficult to realize so many constraints by hardware alone, and the finite control set model predictive control technique is not only effective for nonlinear and strongly coupled control systems, but also easy to integrate various nonlinear constraints into the control algorithms, so that various constraints in the control of motors can be handled at the algorithmic level. Therefore, this chapter first introduces the mathematical model of the PMSM and the topology of the two-level inverter and outlines the basic principles and implementation points of the MPC. Then, the finite set model predictive control is applied to the current loop of a permanent magnet synchronous motor, and its dynamic and steady state performances are simulated and analyzed. Subsequently, MPC-related issues, including online calculation of load and parameter robustness, are discussed, providing a theoretical basis for the subsequent research in this thesis.

2.2. Mathematical Model of Permanent Magnet Synchronous Motor

The Permanent Magnet Synchronous Motor (PMSM) primarily consists of several key components, including the stator, rotor, shaft, and housing. It can be categorized into three main types: Surface-Mounted PMSM (SPMSM), Embedded PMSM (EPMSM), and Interior PMSM (IPMSM).

The SPMSM features a simple structure with its permanent magnets located on the outer surface of the rotor core. Due to its low manufacturing costs, small rotational inertia, and reduced harmonic content in the magnetic flux, it is widely utilized in industrial applications. In contrast, the EPMSM has its permanent magnets positioned within the surface of the rotor, resulting in a high air gap magnetic flux density capable of generating substantial electromagnetic torque. However, this design is associated with increased structural complexity, higher manufacturing costs, and greater magnetic leakage. The IPMSM incorporates its permanent magnets within the rotor core, offering advantages such as robustness, excellent dynamic performance, and high power density. Nonetheless, it also suffers from increased structural complexity, elevated magnetic leakage coefficients, and significantly higher manufacturing costs compared to the SPMSM. Considering the advantages and disadvantages of these three PMSM types, the PMSM drive system designed in this study adopts the Surface-Mounted PMSM as the target for control.

2.2.1. Commonly Used Coordinate Systems and Coordinate Transformations

Taking the A-axis as the reference axis, the commonly used motor coordinate systems are as follows: 1) Three-phase stationary coordinate system (ABC coordinate system): The three-phase symmetric stator windings of the PMSM are aligned with the A, B, and C axes, which are spaced 120° apart in space; 2) Two-phase stationary coordinate system (*α-β* coordinate system): The *α*-axis coincides with the A-axis, and the *β*-axis leads the *α*-axis by 90°; 3) Two-phase rotating coordinate system (*d-q* coordinate system): The magnetic field direction of the rotor permanent magnet is along the *d*-axis, and the *q*-axis leads the *d*-axis by 90°.

Next, the transformation between different coordinate systems, namely the Clarke transform and Park transform, will be introduced. The Clarke transformation converts variables from the ABC coordinate system to the *α-β* coordinate system, and the Park transformation is the transformation of variables in the *α-β* coordinate system to the *d-q* coordinate system.

The matrix form of the Clark transform is:

$$\begin{bmatrix} u_\alpha \\ u_\beta \end{bmatrix} = \begin{bmatrix} 1 & -\dfrac{1}{2} & -\dfrac{1}{2} \\ 0 & \dfrac{\sqrt{3}}{2} & -\dfrac{\sqrt{3}}{2} \end{bmatrix} \begin{bmatrix} u_A \\ u_B \\ u_C \end{bmatrix} \tag{2.1}$$

If based on the principle of constant amplitude, the right matrix of (2.1) needs to be preceded by the factor 2/3, and if based on the principle of constant power, the right matrix of (2.1) needs to be preceded by the factor $\sqrt{2/3}$. Its inverse transformation is:

$$\begin{bmatrix} u_A \\ u_B \\ u_C \end{bmatrix} = \begin{bmatrix} 1 & 0 \\ -\frac{1}{2} & \frac{\sqrt{3}}{2} \\ -\frac{1}{2} & -\frac{\sqrt{3}}{2} \end{bmatrix} \begin{bmatrix} u_\alpha \\ u_\beta \end{bmatrix} \tag{2.2}$$

Similarly, if based on the principle of constant amplitude, the right matrix of (2.2) needs to be preceded by the factor 2/3, and if based on the principle of constant power, the right matrix of (2.2) needs to be preceded by the factor $\sqrt{2/3}$.

The matrix form of the Park transform is:

$$\begin{bmatrix} u_d \\ u_q \end{bmatrix} = \begin{bmatrix} \cos\theta & \sin\theta \\ -\sin\theta & \cos\theta \end{bmatrix} \begin{bmatrix} u_\alpha \\ u_\beta \end{bmatrix} \tag{2.3}$$

Its inverse transformation is:

$$\begin{bmatrix} u_\alpha \\ u_\beta \end{bmatrix} = \begin{bmatrix} \cos\theta & -\sin\theta \\ \sin\theta & \cos\theta \end{bmatrix} \begin{bmatrix} u_d \\ u_q \end{bmatrix} \tag{2.4}$$

2.2.2. Mathematical Model of PMSM in Stationary Coordinate System

Due to the complexity of the PMSM mathematical model, simplifications are often necessary for control purposes, where certain secondary influencing factors are typically neglected. The main assumptions are as follows [37]: 1) The motor's magnetic circuit characteristics are assumed to follow a linear relationship, ignoring core saturation effects; 2) Eddy current and hysteresis losses are neglected; 3) The damping windings in the rotor are disregarded; 4) The effects of external factors such as temperature, humidity, and mechanical wear on the motor's performance and characteristics are ignored.

The motor voltage equation in the three-phase stationary coordinate system can be expressed as:

$$\begin{bmatrix} u_A \\ u_B \\ u_C \end{bmatrix} = \begin{bmatrix} R_s & 0 & 0 \\ 0 & R_s & 0 \\ 0 & 0 & R_s \end{bmatrix} \begin{bmatrix} i_A \\ i_B \\ i_C \end{bmatrix} + \begin{bmatrix} \frac{d\psi_A}{dt} \\ \frac{d\psi_B}{dt} \\ \frac{d\psi_C}{dt} \end{bmatrix} \tag{2.5}$$

where a, u_B, u_C are the phase voltages of the three-phase stator; i_A, b_{id}, i_C are the phase currents of the three-phase stator; ψ_A, ψ_B, ψ_C are the three-phase stator flux linkages; R_s is the stator resistance.

The flux linkage equation is:

$$\begin{bmatrix} \psi_A \\ \psi_B \\ \psi_C \end{bmatrix} = \begin{bmatrix} L_{AA} & L_{AB} & L_{AC} \\ L_{BA} & L_{BB} & L_{BC} \\ L_{CA} & L_{CB} & L_{CC} \end{bmatrix} \begin{bmatrix} i_A \\ i_B \\ i_C \end{bmatrix} + \begin{bmatrix} \psi_{fA} \\ \psi_{fB} \\ \psi_{fC} \end{bmatrix} \tag{2.6}$$

where L_{AA}, L_{BB}, and L_{CC} represent the self-inductances of the stator three-phase windings, while L_{AB}, L_{BA}, L_{BC}, L_{CB}, L_{AC}, and L_{CA} are the mutual inductances between the stator three-phase windings. ψ_{fA}, ψ_{fB}, and ψ_{fC} represent the flux linkage of the permanent magnet field in the three-phase stator windings.

The flux linkages generated by the permanent magnet in the A, B, and C phase stator windings can also be expressed as:

$$\begin{bmatrix} \psi_{fA} \\ \psi_{fB} \\ \psi_{fC} \end{bmatrix} = \psi_f \begin{bmatrix} \cos\theta \\ \cos\left(\theta - 120^\circ\right) \\ \cos\left(\theta + 120^\circ\right) \end{bmatrix} \tag{2.7}$$

where ψ_f represents the rotor flux linkage amplitude, and θ denotes the angle between the stator and rotor flux linkages.

The electromagnetic torque T_e of the PMSM is the partial derivative of the magnetic field stored energy W_m with respect to the mechanical angle θ_m:

$$T_e = \frac{1}{2} p_n \frac{\partial}{\partial \theta_m} \left(i_A \psi_A + i_B \psi_B + i_C \psi_C \right) \tag{2.8}$$

where p_n represents the number of pole pairs of the motor, θ_m denotes the mechanical angle, and T_e represents the electromagnetic torque.

Substituting (2.5) and (2.6) into (2.1) yields the voltage equation and the flux linkage equation for the PMSM in the α-β coordinate system. The stator voltage is

$$\begin{bmatrix} u_\alpha \\ u_\beta \end{bmatrix} = \begin{bmatrix} R_s & 0 \\ 0 & R_s \end{bmatrix} \begin{bmatrix} i_\alpha \\ i_\beta \end{bmatrix} + \begin{bmatrix} \dfrac{d\psi_\alpha}{dt} \\ \dfrac{d\psi_\beta}{dt} \end{bmatrix} \tag{2.9}$$

where u_α, u_β denote the stator voltage of PMSM in α-axis and β-axis respectively, i_α, i_β denote the stator current in α-axis and β-axis respectively, and ψ_α, ψ_β denote the stator magnetic flux linkage in α-axis and β-axis respectively, and its flux linkage expression can be obtained by the inverse Park transform of the flux linkage equation of the PMSM under the d-q axis system with the following expression:

$$\begin{bmatrix} \psi_\alpha \\ \psi_\beta \end{bmatrix} = \begin{bmatrix} \cos\theta & -\sin\theta \\ \sin\theta & \cos\theta \end{bmatrix} \begin{bmatrix} L_d i_d + \psi_f \\ L_q i_q \end{bmatrix} \tag{2.10}$$

The electromagnetic torque can be expressed as

$$T_e = \frac{3}{2} p_n \left(\psi_\alpha i_\beta - \psi_\beta i_\alpha \right) \tag{2.11}$$

where T_e represents the electromagnetic torque; p_n represents the number of pole pairs; and ψ_α and ψ_β denote the stator flux linkage in the α-axis and β-axis, respectively.

2.2.3. Mathematical Model of PMSM in Synchronous Rotating Coordinate System

Substituting equations (2.9) and (2.10) into (2.3) yields the stator voltage and flux linkage equations of PMSM in the *dq* coordinate system. The stator voltage equation can be expressed as:

$$\begin{bmatrix} u_d \\ u_q \end{bmatrix} = R_s \begin{bmatrix} i_d \\ i_q \end{bmatrix} + \omega_e \begin{bmatrix} -\psi_q \\ \psi_d \end{bmatrix} + \begin{bmatrix} \dfrac{d\psi_d}{dt} \\ \dfrac{d\psi_q}{dt} \end{bmatrix} \tag{2.12}$$

where u_d and u_q represent the stator voltages in the *d*-axis and *q*-axis, respectively; i_d and i_q represent the stator currents in the *d*-axis and *q*-axis, respectively; R_s represents the stator resistance; ψ_d and ψ_q represent the stator flux linkages in the *d*-axis and *q*-axis, respectively.

The stator flux linkage equations are expressed as:

$$\begin{bmatrix} \psi_d \\ \psi_q \end{bmatrix} = \begin{bmatrix} L_d & 0 \\ 0 & L_q \end{bmatrix} \begin{bmatrix} i_d \\ i_q \end{bmatrix} + \begin{bmatrix} \psi_f \\ 0 \end{bmatrix} \tag{2.13}$$

where L_d and L_q represent the inductances in the *d*-axis and *q*-axis, respectively; ψ_f represents the permanent magnet flux linkage. Substituting (2.13) into (2.12), the stator voltage equation is obtained as:

$$\begin{bmatrix} u_d \\ u_q \end{bmatrix} = R_s \begin{bmatrix} i_d \\ i_q \end{bmatrix} + \begin{bmatrix} L_d & 0 \\ 0 & L_q \end{bmatrix} \begin{bmatrix} \dfrac{di_d}{dt} \\ \dfrac{di_q}{dt} \end{bmatrix} + \omega_e \begin{bmatrix} 0 & -L_q \\ L_d & 0 \end{bmatrix} \begin{bmatrix} i_d \\ i_q \end{bmatrix} + \omega_e \begin{bmatrix} 0 \\ \psi_f \end{bmatrix} \tag{2.14}$$

The electromagnetic torque equation is:

$$T_e = \frac{3}{2} p_n i_q \left[\left(L_d - L_q \right) i_d + \psi_f \right] \tag{2.15}$$

Mechanical equations of motion for a motor:

$$T_e - T_L - B\omega_m = J\frac{d\omega_m}{dt} \tag{2.16}$$

$$\frac{d\theta_m}{dt} = \omega_m \tag{2.17}$$

where T_e denotes the electromagnetic torque; T_L denotes the load torque; p_n denotes the number of motor pole pairs; B denotes the damping coefficient; J denotes the rotational inertia; and ω_m denotes the mechanical angular velocity. SPMSM exists stator inductance L_d=L_q, so the electromagnetic torque can be expressed as:

$$T_e = \frac{3}{2}P_n\psi_f i_q \tag{2.18}$$

When $i_d = 0$, from (2.18), it can be seen that the electromagnetic torque of the SPMSM at this point depends solely on i_q. Therefore, torque control can be achieved simply by controlling i_q.

2.3. Mathematical Modeling of Two-level Inverters and CMV

Motors are often driven using a three-phase two-level inverter circuit as shown in Fig. 2. 1, where U_dc is the dc bus voltage, N is the neutral point of the motor stator winding, and O is the middle point of the dc side.

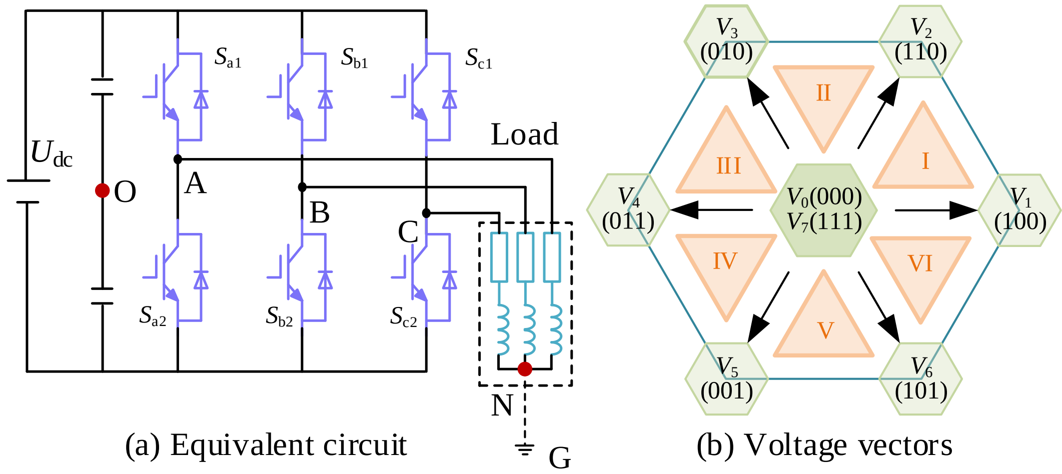

Fig. 2. 1. Topology and voltage vectors. (a) Equivalent circuit. (b) Voltage vectors.

The switching state of each bridge arm power converter can be defined as S_x (x= 1, ⋯, 6), and the conversion from dc to ac is often performed in compensation mode to avoid dc supply short circuit. The state of one-phase bridge arm can be indicated by the switching signals S_a, S_b, S_c. If "1" is used to indicate that the upper bridge arm is open and "0" is used to indicate that the lower bridge arm is open, then the upper bridge arm conduction of phase A is indicated as $S_a = 1$. The three bridge arm switching tubes are flexible, and there are a total of $2^3 = 8$ switching combinations, which are shown in Table 2.1. They can form 8 discrete switching states, corresponding to the voltage vectors V_0 to V_7 in **Error! Reference source not found.**(b).

In the $\alpha\beta$ coordinate system, the three-phase output voltage can be expressed as

$$\begin{bmatrix} u_\alpha \\ u_\beta \end{bmatrix} = \frac{2}{3}\begin{bmatrix} 1 & -\frac{1}{2} & -\frac{1}{2} \\ 0 & \frac{\sqrt{3}}{2} & -\frac{\sqrt{3}}{2} \end{bmatrix}\begin{bmatrix} u_{an} \\ u_{bn} \\ u_{cn} \end{bmatrix} \tag{2.19}$$

TABLE 2.1

INVERTER SWITCHING STATE

	$\boldsymbol{u}_0$	$\boldsymbol{u}_1$	$\boldsymbol{u}_2$	$\boldsymbol{u}_3$	$\boldsymbol{u}_4$	$\boldsymbol{u}_5$	$\boldsymbol{u}_6$	$\boldsymbol{u}_7$
S_a	0	1	1	0	0	0	1	1
S_b	0	0	1	1	1	0	0	1
S_c	0	0	0	0	1	1	1	1

When expressed in terms of the upper bridge arm switching state, the output voltage can be expressed as:

$$\begin{aligned}\begin{bmatrix} u_\alpha \\ u_\beta \end{bmatrix} &= \frac{2}{3}\begin{bmatrix} 1 & -\frac{1}{2} & -\frac{1}{2} \\ 0 & \frac{\sqrt{3}}{2} & -\frac{\sqrt{3}}{2} \end{bmatrix}\left\{\begin{bmatrix} u_a \\ u_b \\ u_c \end{bmatrix} - \begin{bmatrix} u_n \\ u_n \\ u_n \end{bmatrix}\right\} \\ &= \frac{2}{3}U_{dc}\begin{bmatrix} 1 & -\frac{1}{2} & -\frac{1}{2} \\ 0 & \frac{\sqrt{3}}{2} & -\frac{\sqrt{3}}{2} \end{bmatrix}\begin{bmatrix} S_a \\ S_b \\ S_c \end{bmatrix}\end{aligned} \tag{2.20}$$

The CMV is defined as the potential between the load neutral point and the center of the dc-bus, $V_{\mathrm{CMV}} = \left(U_{\mathrm{AO}} + U_{\mathrm{BO}} + U_{\mathrm{CO}}\right)/3$, and it can be calculated as follows:

$$\begin{cases} U_{\mathrm{AO}} = U_{\mathrm{dc}}\left(S_a - 1/2\right) \\ U_{\mathrm{BO}} = U_{\mathrm{dc}}\left(S_b - 1/2\right) \\ U_{\mathrm{CO}} = U_{\mathrm{dc}}\left(S_c - 1/2\right) \end{cases} \tag{2.21}$$

where U_{AO}, U_{BO}, and U_{CO} are the three-phase terminal voltages.

Table 2.2 shows the amplitudes of corresponding CMV generated by six active vectors and two zero vectors. It can be seen that the use of zero vector results in higher

CMV. To suppress the CMV, two zero vectors V_0 and V_7 should be avoided whenever possible.

TABLE 2.2

CMV AMPLITUDE CORRESPONDING TO EACH VOLTAGE VECTOR

Voltage Vectors	V_{CMV}
V_0(000)	$-U_{dc}/2$
V_7(111)	$U_{dc}/2$
V_1(100), V_3(010), V_5(001)	$-U_{dc}/6$
V_2(110), V_4(011), V_6(101)	$U_{dc}/6$

2.4. Basic Principles of Finite Set Model Predictive Control Strategy

Model Predictive Control (MPC), as an advanced control algorithm, does not refer to a specific control algorithm with a defined structure, but rather to a class of model-based closed-loop optimization control strategies. The core idea of the algorithm is: at the current control instant, the system's behavior over a finite future time horizon is predicted using a dynamic mathematical model, called the prediction model. Then, different control sequences within this time horizon are evaluated, and the optimal control sequence is determined by a predefined cost function.

The principle is illustrated in Fig. 2. 2. At kth instant, the system's mathematical model is used to predict the state variables $x(k+1), x(k+2), \cdots, x(k+N)$ at the future time steps ($k+1, k+2, \cdots, k+N$). Control inputs $u(k), u(k+1), \cdots, u(k+N-1)$ are selected at these time steps to ensure that the system state variables x continually move closer to the reference trajectory x^*. In each sampling period, new feedback variables are measured, the system's new state is predicted, and the value function is minimized. The entire prediction process yields a series of optimal control inputs, but only the first control input, $u(k) = u_{opt}(k)$, is applied.

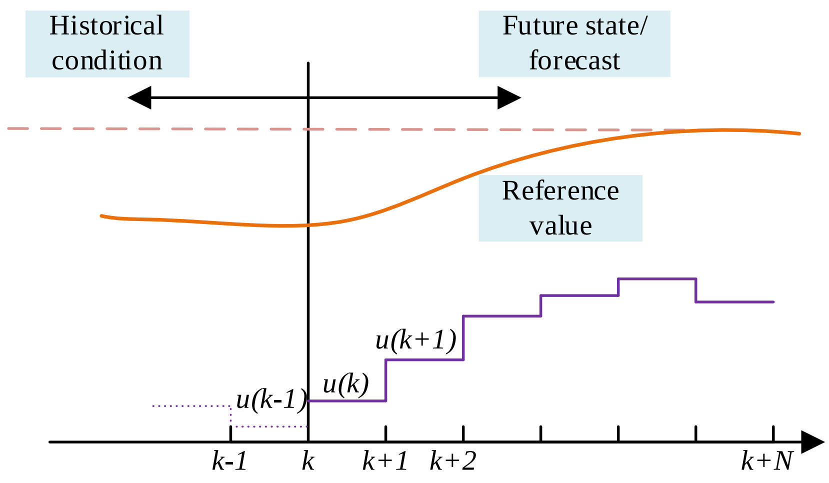

Fig. 2. 2. Operating principle of MPC.

The MPC control block diagram, as shown in Fig. 2. 3, mainly consists of three major components: the prediction model, cost function optimization, and measurement feedback loop. A general state equation for a discrete system can be represented as follows, which serves as the prediction model to forecast the future state variables of the controlled system:

$$\begin{cases} x(k+1) = Ax(k) + Bu(k) \\ y(k) = Cx(k) + Du(k) \end{cases} \tag{2.22}$$

The optimization of the cost function requires the definition of an appropriate cost function to select the optimal control input. The cost function should fully consider the reference values of the discrete system, the state variables, and future operations, as follows:

$$J = f(x(k), u(k), ..., u(k+N)) \tag{2.23}$$

where $x(k)$ is the state variable, and $u(k),\ldots, u(k+N)$ represents the N control inputs chosen over a predetermined time period N. However, the controller only outputs the first element of the optimized sequence as the optimal input. The sequence is as follows:

$$u(k)_{opt} = [1\ 0 ... 0] \arg \quad \min_u J \tag{2.24}$$

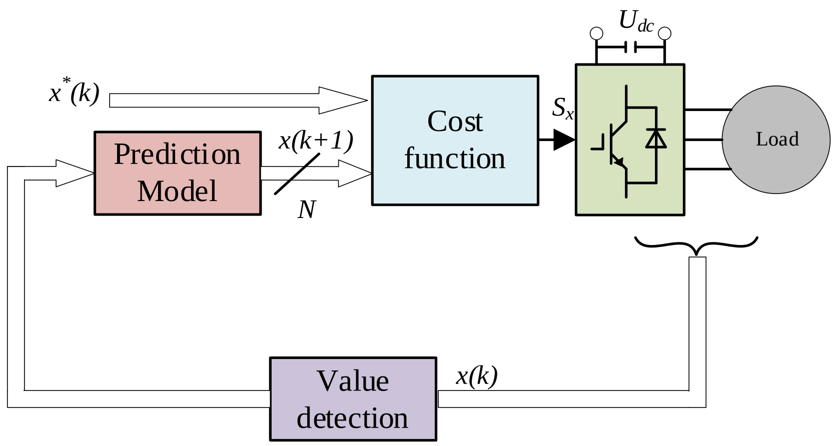

Fig. 2. 3. General structure block diagram of MPC.

By continuously updating measurements to obtain the latest data and determining the corresponding optimal control input for each case, an optimization process is required in each control cycle. This is known as the rolling optimization strategy.

There are various types of MPC algorithms, with multiple forms of implementation. One of the most researched and applied MPC methods at present is Finite Set MPC (FS-MPC). In this thesis, the FS-MPC algorithm is applied to motor drive systems, where the control input set is restricted to a finite number of switch combinations of the inverter. The complex optimization problem of solving the cost function is transformed into an integer programming problem, and the optimal solution to the value function is determined through an exhaustive search method.

In the control process of a motor, in addition to the requirements for steady-state performance and dynamic response, the operation is also subject to various constraints, such as voltage, current, etc. It is difficult to achieve so many constraints solely through hardware. However, FS-MPC not only performs well for nonlinear, strongly coupled control systems but also easily integrates various nonlinear constraints into the control algorithm. This allows for handling various constraints in motor control at the algorithmic level. Despite the simplicity of the control principle and the ease of setting constraints, FS-MPC also has some inherent drawbacks. For instance, compared to classical controllers (such as PI controllers), it requires more computational resources, places higher demands on controller performance, and the accuracy of the mathematical model of the controlled system directly affects the control performance.

2.5. Conventional Current Control of PMSM Based on FS-MPC

In this thesis, we study the model predictive current control with SPMSM (L_d=L_q=L_s) as the object to be controlled, and at the same time, in order to facilitate the controller design and optimization at a later stage, the mathematical model of the SPMSM under the synchronous rotating coordinate system *d-q* axis as in Chapter 2.2.3 is used, and it is obvious that (2.14) expresses the continuous state equations of a system; however, in the actual digital control system, a continuous state equation should be discretized so that it can be processed by the microprocessor. Assuming that the control period of the system is T_s, a first-order discretization of (2.14) with the leading Eulerian term yields

$$\begin{cases} i_d(k+1) = i_d(k) + \dfrac{T_s}{L}\left[u_d(k) - R_s i_d(k) + E_d(k)\right] \\ i_q(k+1) = i_q(k) + \dfrac{T_s}{L}\left[u_q(k) - R_s i_q(k) + E_q(k)\right] \end{cases} \tag{2.25}$$

$$\begin{cases} E_d(k) = \omega_e(k) L i_q(k) \\ E_q(k) = -\omega_e(k) L i_d(k) - \omega_e(k)\psi_f \end{cases} \tag{2.26}$$

Conventional current FS-MPC for SPMSM replaces the *dq*-axis current inner loop in the vector control system with the model predictive controller and retains the speed loop PI controller. Since the two-level three-phase inverter can output 2 zero vectors and 6 active voltage vectors, a total of 8 basic voltage vectors. Substituting the 8 basic voltage vectors of the inverter into (2.14) can generate 8 consequent future load current behaviors. Among these available voltage vectors, the voltage vector corresponding to the current prediction value that minimizes the cost function is selected as the optimal value. The classical cost function to measure errors between the predicted load currents and the reference value is as follows:

$$g = \left|i_d^* - i_d(k+1)\right|^2 + \left|i_q^* - i_q(k+1)\right|^2 \tag{2.27}$$

where i_d^* and i_q^* are the expected values of motor *dq*-axis current, which is given by the speed outer loop after PI control.

Thus, the optimization process utilized by the conventional method is computationally burdensome. The only selected voltage vector is applied during one entire sampling period which also leads to a higher current ripple at steady-state. Deadbeat control is a discrete control technology that makes the controlled quantity reach the desired value within one control cycle [62]. According to the deadbeat control principle, the *d*-*q* axis currents track the given value without error at the next instant. The reference voltage can be deduced according to (2.25)

$$\begin{cases} i_d(k+1) = i_d^* \\ i_q(k+1) = i_q^* \end{cases} \tag{2.28}$$

$$\begin{cases} u_d(k+1) = Ri_d(k) + L\left[i_d^* - i_d(k)\right]/T_s - \omega_e L i_q(k) \\ u_q(k+1) = Ri_q(k) + L\left[i_q^* - i_q(k)\right]/T_s + \omega_e\left[L i_d(k) + \psi_f\right] \end{cases} \tag{2.29}$$

d-*q* axis reference voltages can be transformed into *α*-*β* plane through the inverse Park transformation

$$\begin{bmatrix} u_\alpha(k+1) \\ u_\beta(k+1) \end{bmatrix} = \begin{bmatrix} \cos\theta & -\sin\theta \\ \sin\theta & \cos\theta \end{bmatrix} \begin{bmatrix} u_d(k+1) \\ u_q(k+1) \end{bmatrix}. \tag{2.30}$$

The cost function is modified to

$$g = \left|u_\alpha^i - u_\alpha(k+1)\right|^2 + \left|u_\beta^i - u_\beta(k+1)\right|^2 \tag{2.31}$$

As shown in Fig. 2. 4, under this method, it only needs to predict one voltage vector during one sampling period. The simplified cost function (2.31) can be regarded as the distance between predictive vector and basic vectors. Finally, the phase angle of reference voltage can be calculated as

$$\theta_{\text{ref}} = \arctan\left(u_\alpha(k+1)/u_\beta(k+1)\right). \tag{2.32}$$

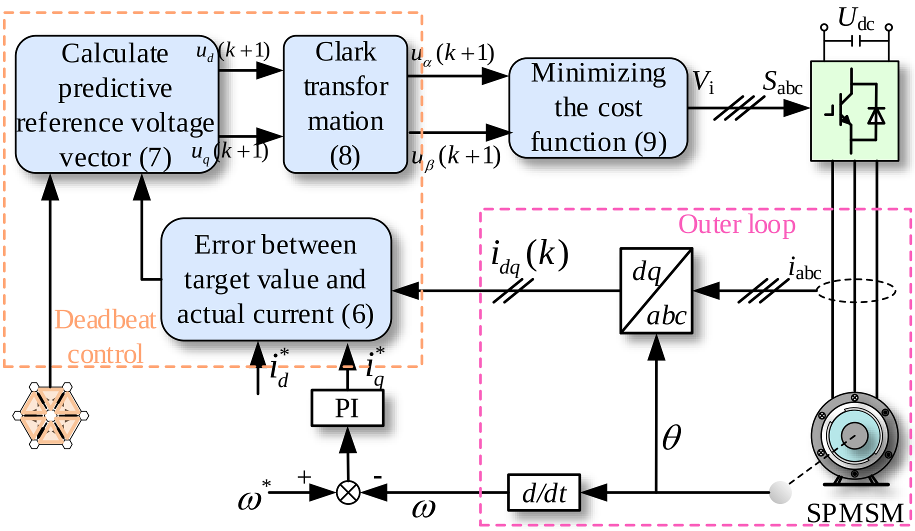

Fig. 2. 4. Control diagram of the conventional FS-MPC by predicting one voltage vector.

2.6. Simulation Results and Limitation Analysis

Simulation analysis was conducted for the FS-MPC system of the PMSM discussed in this chapter. The control object is a surface-mounted PMSM with four pole pairs, and its parameters are detailed in Table 2.3. Simulation waveforms for no-load operation, load operation, and sudden load changes are presented and compared with those obtained using traditional vector control strategies. The outer loop maintains a speed controller with a Proportional-Integral (PI) component, consistent with FOC, while the current inner loop relies on the FS-MPC algorithm for its implementation.

TABLE 2.3

PARAMETERS OF PMSM

Parameter	Value
Stator resistance R_s	0.74 Ω
Stator inductance L_s	2.96 mH
Rated torque T_e	5 Nm
Rated power P_N	200 W
Rotor flux linkage ψ_f	0.055 Wb
Rotational inertia J	0.004 $kg \cdot m^2$

Under the predictive current control, the relevant performance of the motor is illustrated in Fig. 2. 5. The simulation time step is set to 100 μs, and the PI parameters for the speed loop are k_p = 2 and k_i = 50. The effects of delays are not considered in the simulation. Firstly, the motor is started from standstill with no load at t=0 s to a speed of 1000rpm. At t=0.2s, the motor's given speed is increased to 1200rpm, and the given speed is suddenly reduced to 1000r/min at 0.4s. At t=0.6 s, a load torque of 5 Nm is applied to the motor, the overall simulation time is 1s.

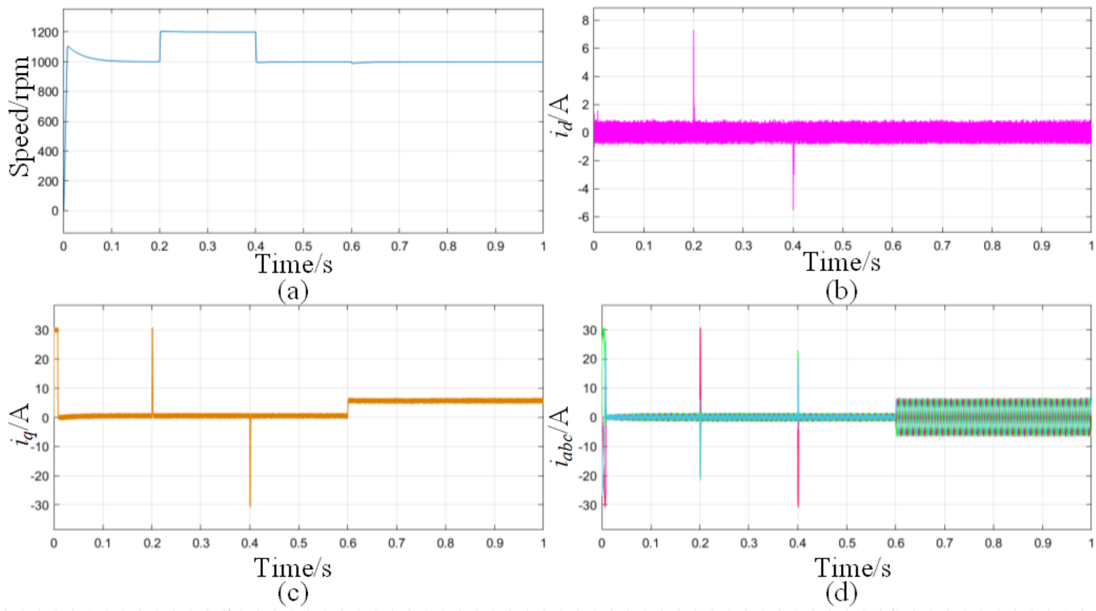

Fig. 2. 5. Simulation waveforms of FS-MPC.

Fig. 2. 5(a) presents the speed curve during the motor startup, accelerate/decelerate, and loading process. It can be observed that the speed quickly tracks the setpoint with nearly no overshoot, and the rise time is approximately 58.637 ms. Both accelerate and decelerate speed responses exhibit a good slope. After applying the load, the speed decreases by about 0.7 rpm.

Fig. 2. 5 (b) and (c) shows the *dq*-axis current ripple throughout the operation. In steady state, the *d*-axis ripple is approximately 0.375 A, and the *q*-axis ripple is about 0.188 A, with a rise time of approximately 1.59 ms. Fig. 2. 5(d) illustrates the three-phase current in different states. Combining this with Fig. 2. 5(b), it can be seen that whether during startup or in accelerate/decelerate operation, the phase currents all return to sinusoidal form very quickly.

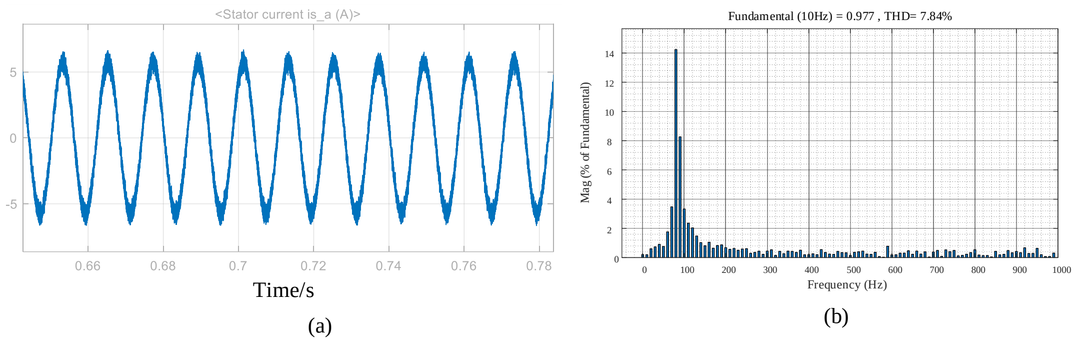

Fig. 2. 6. Steady-state phase current analysis.

Fig. 2. 6 (a) and 2.6(b) present the A-phase stator current and its harmonic spectrum analysis in steady state, where the harmonic content of the current is approximately 7.84%. Fig. 2. 7 illustrates the switching waveforms of the three-phase bridge throughout the operation. It can be observed that in the FS-MPC algorithm, there is no direct correlation between the switching states at consecutive time instances; rather, the switching state is determined by selecting the one that minimizes the cost function. The selection of switching vectors at two consecutive moments may be adjacent, non-adjacent, or may remain unchanged.

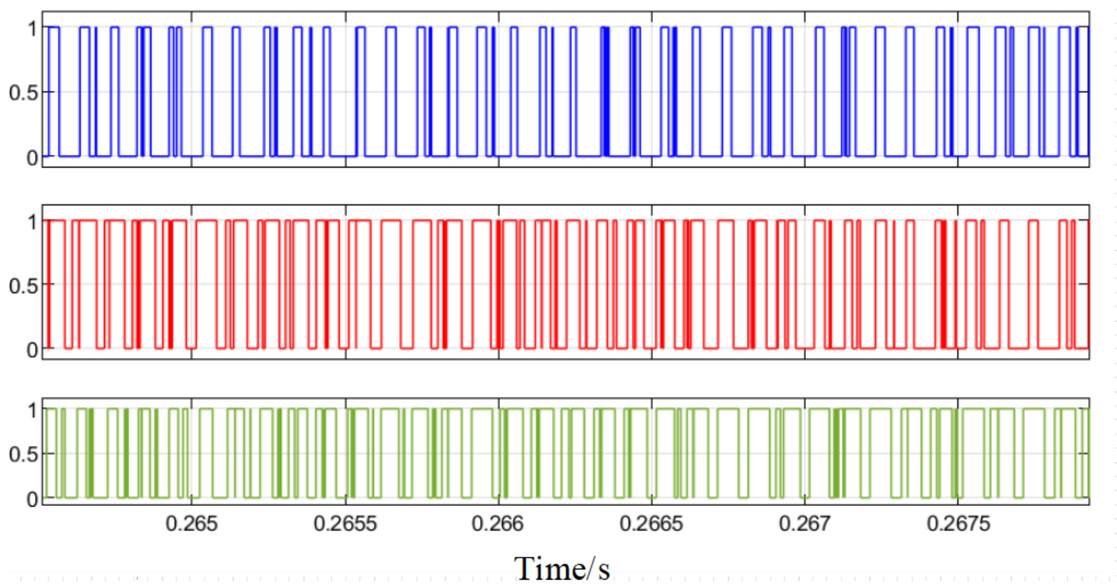

Fig. 2. 7. FS-MPC Three-phase output state.

Compared to traditional Field Oriented Control (FOC) algorithms, the finite control set model predictive control eliminates the modulation module, directly applying the switching signals to the inverter. This undoubtedly increases the harmonic content of the current while also accelerating system response. From a holistic perspective, the optimization process of the FS-MPC control algorithm utilizes an exhaustive method to obtain the optimal control voltage, which can be inefficient and computationally intensive.

In contrast to conventional vector control algorithms, model predictive control does not require tuning of current loop parameters as is necessary in vector control; rather, it directly controls the *dq*-axis currents via the cost function, seamlessly integrating various nonlinear constraints into the cost function. Additionally, by omitting the Space Vector Pulse Width Modulation (SVPWM) module found in FOC control, the FS-MPC simplifies the control; however, when using a single control voltage over an entire cycle and with longer sampling intervals, the steady-state performance may decline.

2.7. Conclusion

This chapter begins by introducing the fundamental structure and classification of Permanent Magnet Synchronous Motors (PMSMs). It then presents mathematical modeling and analysis of PMSMs under different coordinate systems. A detailed explanation of the mathematical principles and execution steps of the Finite Set Model Predictive Control (FS-MPC) algorithm is provided. Subsequently, based on the mathematical models of the three-phase PMSM and the two-level inverter, a cost function is designed in accordance with the control characteristics and system constraints of permanent magnet machines. This approach effectively achieves current control of the PMSM using the FS-MPC algorithm. Validation confirms that the algorithm is capable of current tracking, and the designed nonlinear function effectively limits the current amplitude, allowing the control algorithm to function without complex parameter designs. However, there are also limitations that need further resolution, such as significant steady-state fluctuations and excessive dependence on motor parameters.

CHAPTER 3. PROPOSED HIGH-EFFICIENT MULTIVECTOR MPC WITH CMV SUPPRESSION

3.1. Introduction

Multivector model predictive control (MPC) has gained many attractions in motor drive applications due to its accurate and stable control performance. However, two key challenges have limited the control development. First of all, the switching frequency is not fixed and remains at a high level under the full range of operating conditions. More seriously, the zero vectors applied to adjust the output amplitude will generate high common-mode voltage (CMV), resulting in axis current, electromagnetic interference, and a host of other adverse effects. To address the two main concerns, this chapter proposes a control strategy that can efficiently respond to different operating conditions for permanent magnet synchronous motors (PMSMs). First, the reference voltage is constructed by the deadbeat principle, and the motor operating condition is distinguished according to the amplitude of the reference voltage. Second, to inherit satisfactory performance in steady-state while exhibiting fast current tracking response simultaneously, two voltage generation approaches that avoid the use of zero vectors are designed. Finally, comparative experimental results are presented, and the effectiveness of the proposed strategy is verified.

3.2. Motor Running Status Judgment

In actual operation, the running status of the motor drive system is not static. The nonadjustable reference voltage vector generation method may cause the problem of output range mismatch. The block diagram is shown in Fig. 3. 1, by alternating between two voltage vector generation methods, it can respond to the output demand of different operating conditions. The inherent negative impact of CMV can be minimized and, at the same time, achieve better steady and dynamic control performance with low switching frequency.

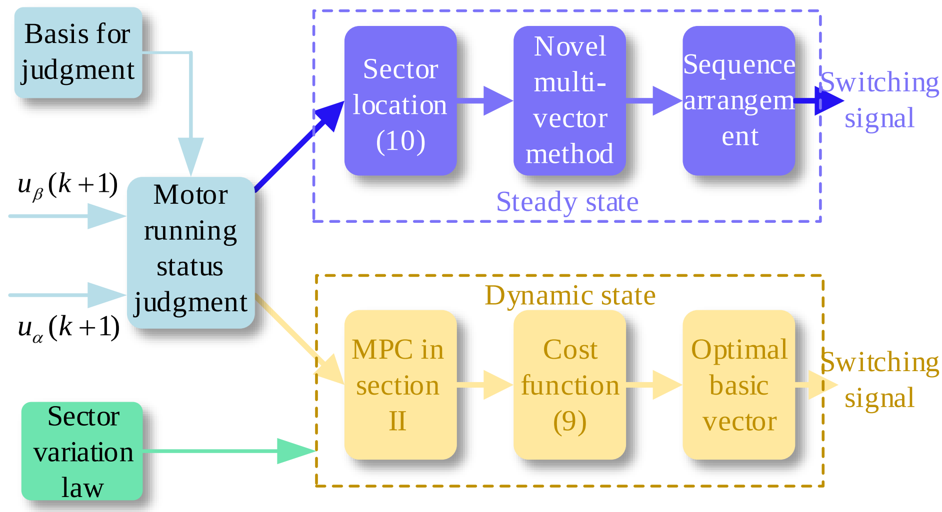

Fig. 3. 1. Block diagram of the proposed control strategy.

A sudden change of the speed or load may occur during the motor operation. This requires the fastest current change rate to dynamically respond to the value given. When the motor is in a steady state, the main control purpose is to obtain the smoothest possible output. Switching to the most appropriate control strategies requires first determining what condition the motor is working in. In this chapter, a switching threshold U_{sh} is introduced to apply the most reasonable voltage generation method within a control cycle according to the magnitude of different reference voltage vectors. Due to (3.1), the reference voltage vector changes abruptly to reach a new equilibrium regardless of the abrupt speed or torque change. Combined with the above analysis, it can be used as an indicator to judge the current operating state.

$$\begin{cases} u_d(k+1) = Ri_d(k) + L\left[i_d^* - i_d(k)\right]/T_s - \omega_e L i_q(k) \\ u_q(k+1) = Ri_q(k) + L\left[i_q^* - i_q(k)\right]/T_s + \omega_e\left[L i_d(k) + \psi_f\right] \end{cases} \tag{3.1}$$

In the case of different amplitudes of the reference voltage vector, the applicability of different methods is analyzed as shown in Fig. 3. 2. The vertices of the voltage vectors in the finite control set are on the edges of the positive hexagon, and the reference voltage vectors corresponding to the single-vector and multivector synthesis methods are $u_{s,1}^{\mathrm{ref}}$ and $u_{s,2}^{\mathrm{ref}}$, respectively.

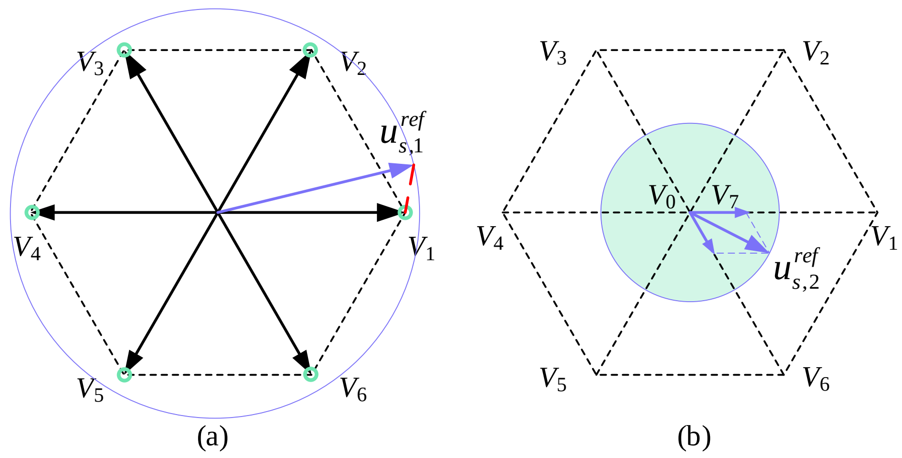

Fig. 3. 2. Range of output voltage vector of different methods. (a) Single-vector method. (b) Multivector synthesis methods.

Therefore, when the amplitude of the reference voltage vector is large, it is closer to the finite control set, and the control performance will remain good. When the amplitude is small, especially close to 0, its output fluctuation is relatively large. This is due to the fact that the use of zero vector is abandoned to suppress the CMV, which is quite different from the candidate set. While the multivector synthesis method accurately synthesizes the reference vector online, but correspondingly its switching frequency will also be very large. It is necessary to analyze the relationship between active vectors and output fluctuation. Fig. 3. 3 illustrates the α-axis current control performances of different voltage generation methods. Δi_α is the current ripple. At the beginning and end of the control cycle, α-axis currents can be expressed as

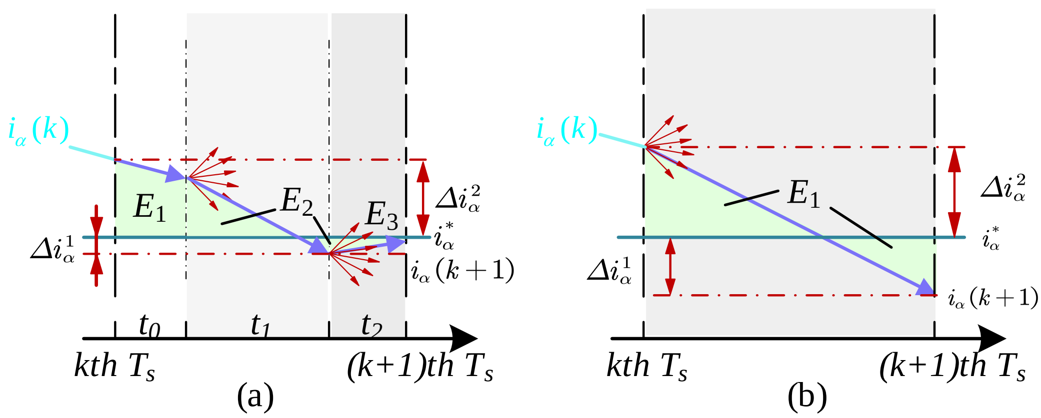

Fig. 3. 3. α-axis current behaviors with different voltage vectors. (a) Multivector synthesis. (b) Single vector FS-MPC.

$$\begin{cases} i_\alpha(k+1) = i_\alpha(k) + \delta_{\alpha 0} t_0 + \delta_{\alpha 1} t_1 + \delta_{\alpha 2} t_2 \\ \Delta i_\alpha^1 = i_\alpha^* - i_\alpha(k) \\ \Delta i_\alpha^2 = i_\alpha^* - i_\alpha(k+1) \end{cases} \tag{3.2}$$

where t_i are the durations of the candidate vectors. $\delta_{\alpha i}$ represent the current slopes under the different applied vectors and can be calculated as follows:

$$\begin{cases} \delta_{\alpha i} = \delta_{\alpha 0} + u_\alpha^i / L \\ \delta_{\beta i} = \delta_{\beta 0} + u_\beta^i / L \end{cases} \tag{3.3}$$

$$\delta_{\alpha i}=\left.\frac{\mathrm{d}i_{\alpha}}{\mathrm{d}t}\right|_{u_{\alpha}=u_{\alpha}^{i}}=\delta_{\alpha 0}+\frac{u_{\alpha}^{i}}{L}. \tag{3.4}$$

The effect of each voltage vector on the α-axis current is integrated over one control period, and the areas are defined as E_i. They can be expressed as

$$\begin{cases} t_2=T_s-t_0-t_1 \\ E_i=\int_{t_0}^{t_i}\left[\delta_{\alpha 0}t_0+\delta_{\alpha 1}t_1+\delta_{\alpha 2}\left(T_s-t_0-t_1\right)\right]^2 dt \end{cases} \tag{3.5}$$

Obviously, the fluctuation of the single vector method is more severe, and the area of E_i is larger. Fig. 3. 4 is the comparison of two voltage vector generation methods. It can be seen that the average switching frequency of the single-vector method is low, which output performance is also suitable for the situation where the reference voltage vector amplitude is large; the multivector synthesis method has a low ripple, but the switching frequency is high. A logic instruction M mentioned as follows is designed as the judgment criteria of the running status. The specific corresponding relationships and respective advantages are shown in Table 3.1.

$$\begin{cases} M=1,\ \text{if}\sqrt{Real\left(\boldsymbol{u}_{ref}\right)^2+Imag\left(\boldsymbol{u}_{ref}\right)^2}-U_{sh}\geq 0 \\ M=0,\ \text{if}\sqrt{Real\left(\boldsymbol{u}_{ref}\right)^2+Imag\left(\boldsymbol{u}_{ref}\right)^2}-U_{sh}<0 \end{cases} \tag{3.6}$$

To sum up, the proposed method flexibly selects one of the single-vector MPC in Chapter II or the novel multivector synthesis method according to the magnitude of the reference voltage. From the above space vector distribution, it can be seen that the maximum amplitude of the synthesized reference voltage vector is $U_{dc}/\sqrt{3}$, so the switching threshold U_{sh} range is from 0 to $U_{dc}/\sqrt{3}$.

TABLE 3.1

CORRESPONDING CONTROL STRATEGIES AND REASONS

FOR DIFFERENT OPERATING STATES

Judgment criteria *M*	Voltage vector generation method	Advantages and effects
1	Single-vector MPC in Chapter 2	Fast response, low switching frequency
0	Novel multi-vector synthesis method	Accurately track, low fluctuation

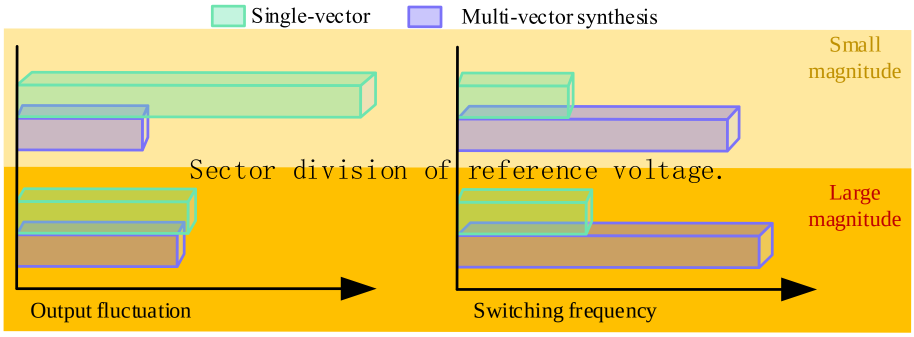

Fig. 3. 4. Comparison of different voltage vector generation methods.

3.3. Sector Variation Law of Reference Voltage Vector

The reason why the traditional MPC strategy has a large amount of calculation, and the switching frequency is not fixed is that there are too many voltage vectors that need to be calculated cyclically, and there is no specific relationship between these voltage vectors. Therefore, the amount of calculation can be reduced, and the switching frequency can be fixed from the perspective of sector variation law.

According to (2.14), when the SPMSM is running stably, u_d is proportional to the product of i_q and speed, and the direction is negative, at which time the voltage vector must be ahead of the current vector by a fixed angle and can be expressed as

$$\sigma_u = atan2\left(R_s i_q + \omega_e \psi_f, -\omega_e L i_q\right) \tag{3.7}$$

Thus, the three-phase symmetrical sinusoidal voltage is the ideal supply method and the trajectory of the reference voltage vector vertex is a circle and rotates counterclockwise at the SPMSM electrical angle ω_e

$$\begin{cases} u_A = U_{dc} e^{j0} \\ u_B = U_{dc} e^{j\frac{2}{3}\pi} \\ u_C = U_{dc} e^{j\frac{4}{3}\pi} \end{cases} \tag{3.8}$$

$$\boldsymbol{u}_{ref} = u_A + u_B + u_C = \frac{3}{2} U_{dc} e^{j\left(\omega t - \frac{\pi}{2}\right)} \tag{3.9}$$

According to the above analysis, the relationship between the angle of the reference voltage vector and the sector number is shown in Fig. 3. 5. Fig. 3. 6 shows the variation of the sector where the reference voltage vector is located in each control cycle. It can be seen from Fig. 3. 6(a) that the sector always changes in a fixed pattern. The reference voltage vector is rotated counterclockwise from Sector I to sector VI in the voltage vector diagram shown in Fig. 2. 1(b), cycling sequentially. Fig. 3. 6(b) shows the enlarged situation of Fig. 3. 6(a). It can be seen that as the control cycle changes, the sector either remains unchanged or is transformed only into the adjacent sector. For example, in Fig. 3. 6(b), the reference voltage vector switches back and forth between these two adjacent areas before completely switching from sector VI to sector I.

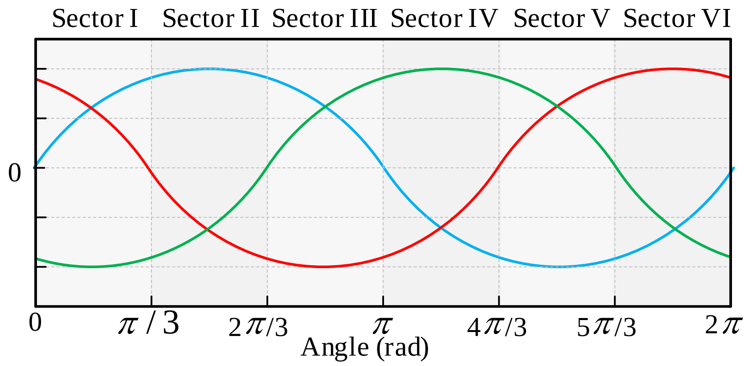

Fig. 3. 5. Sector division of reference voltage.

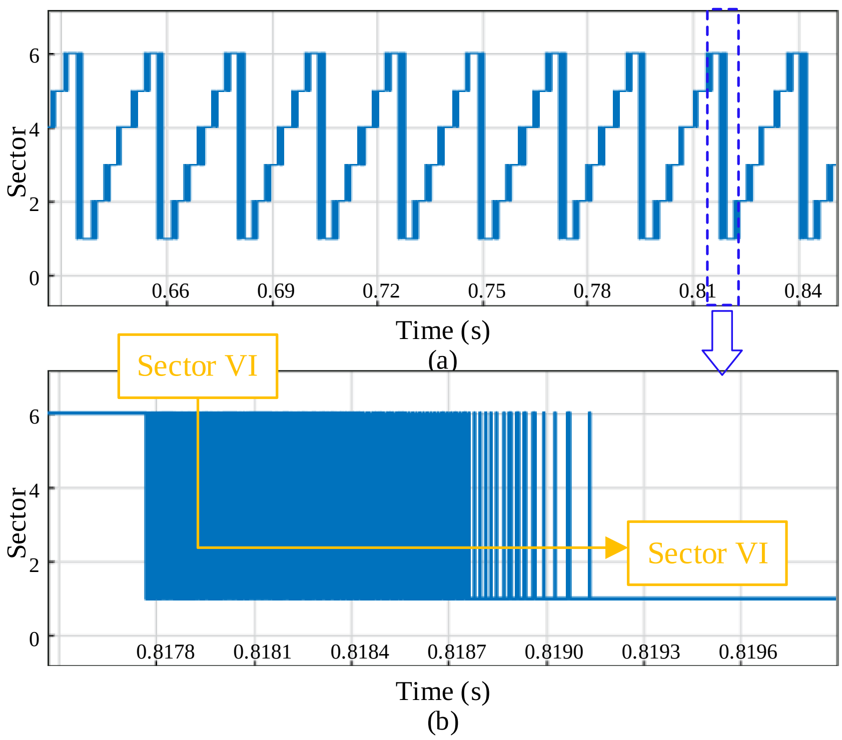

Fig. 3. 6. Sector change waveform in actual operation. (a) Fixed switching pattern. (b) Zoomed-in display.

3.4. Optimized CMV Steady-State Strategy Without Zero Vector

3.4.1. Vector Selection and Action Time Calculation

The conventional vector synthesis method uses two nonzero voltage vectors adjacent to the reference voltage vector and the zero vector to synthesize the u_s^{ref} , with adjustable amplitude and direction. In order to solve the problem of large CMV caused by zero vector, a novel steady-state multivector modulated method is proposed. Because of its unique pulse modulation technique, it is called the back-and-forth synthesis method. The optimized steady-state method consists of the following steps.

1) Nonzero Voltage Vector Selection: In the three-vector synthesis method adopted in [91], two adjacent active vectors of the predicted reference voltage vector and one zero vector are selected. But as analyzed in Chapter 2, making full use of the six nonzero voltage vectors can restrict the CMV within $\pm U_{dc}/6$. Therefore, two nonzero voltage vectors in opposite directions adjacent to the sector where the reference voltage vector is located are selected to be equivalent to the zero vector. Thus, four nonzero voltage vectors are selected to synthesize the reference voltage vector. When the reference voltage vector is located in different sectors, the relationship during the sector position, the adjacent active vectors, and the candidate vectors for the equivalent zero vector are listed in Table 3.2.

TABLE 3.2

SECTORS WITH CORRESPONDING CANDIDATE VECTORS

Sector number	Position	Adjacent active vectors	Equivalent zero vectors
I	[0, π/3]	V_1,V_2	V_6,V_3
II	[π/3, 2π/3]	V_2,V_3	V_1,V_4
III	[2π/3, π]	V_3,V_4	V_2,V_5
IV	[π, 4π/3]	V_4,V_5	V_3,V_6
V	[4π/3, 5π/3]	V_5,V_6	V_4,V_1
VI	[5π/3, 2π]	V_6,V_1	V_5,V_2

2) Vectors Action Time Calculation: As shown in Fig. 3. 7, taking sector I as an example, the expression of each vector action time is introduced. The action time of vector V_1 is defined as t_1, the action time of vector V_2 is t_2, vectors V_6 and V_3 are used as equivalent zero vectors, and the action time t_3 and t_4 of the two are equal, which is half of the action time t_0 of the zero vector. It can be obtained from the geometric relationship.

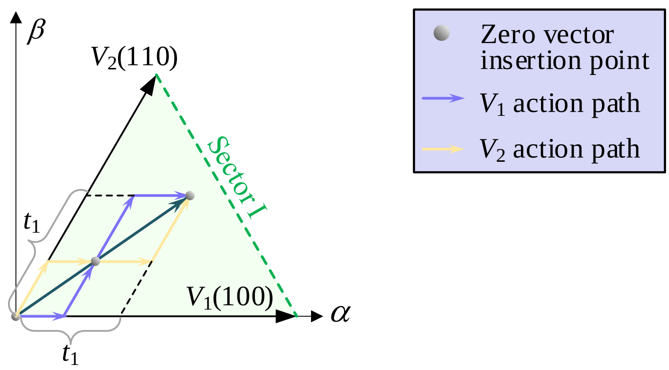

Fig. 3. 7. Schematic of multivector synthesis.

$$\begin{cases} t_1 |U_1| \sin\theta_{ref} = t_2 |U_2| \sin\left(\dfrac{\pi}{3} - \theta_{ref}\right) \\ t_2 |U_2| \sin\left(\dfrac{\pi}{3}\right) = |u_s^{ref}| \sin\theta_{ref}. \end{cases} \tag{3.10}$$

$|U_1| = |U_2| = 2U_{dc}/3$, substituting into (3.10), we can deduce that

$$\begin{cases} t_1 = \dfrac{\sqrt{3}|u_{ref}|}{U_{dc}} \sin\left(\dfrac{\pi}{3} - \theta_{ref}\right) \\ t_2 = \dfrac{\sqrt{3}|u_{ref}|}{U_{dc}} \sin\theta_{ref} \\ t_3 = t_4 = t_0/2 \\ t_0 = T_s - t_1 - t_2 \end{cases} \tag{3.11}$$

3.4.2. Vectors Action Sequence Assignment

In the proposed steady-state strategy, four nonzero voltage vectors are selected in one control cycle. In order to reduce the switching frequency of the inverter during the control cycle and to reduce the switching losses, the vector action sequence needs to be arranged in a reasonable way. The principle to be followed is that only one phase state is changed for each action. Take sector I as an example, the distribution of two opposite voltage vectors and two adjacent voltage vectors are shown in Fig. 3. 8 and Fig. 3. 9.

Despite abandoning the use of zero vectors, V_3 and V_6 can still ensure that only one phase switch needs to be activated at both sides of each control cycle. As explained in Chapter 3.2, sectors always change in a fixed pattern, and only two situations may occur. Fig. 3. 8 shows the switching sequences when the sector of the previous control cycle is consistent with the sector of the current control cycle. Different from the symmetrical three vector method in [97], it can be seen that a control period is divided into 4 segments, clockwise and counterclockwise vector sequences are alternating. In the immediately following control cycle, the four voltage vectors are arranged in reverse order. Due to the characteristic cyclic sequence form, it is named back-and-forth strategy in this thesis. This kind of design can ensure the minimum switching action between different segments. In case 1, there is also no need to switch between different control cycles. Smooth control performance is guaranteed at a lower switching frequency.

If in the next control cycle, the sector where the reference voltage is located changes and goes to the next sector, the selection of two active vectors will change. As shown in Fig. 3. 9, the distribution within a single control cycle is still four segments. The difference with Case 1 is that the switch state needs to be changed once between different control cycles. For example, if V_3 is the last equivalent zero vector of the present control period, then V_4 is distributed at the beginning of the next period. On the other hand, if the vector at the end of the previous control cycle is V_6, the action order of four voltage vectors at the next control period is V_1, V_2, V_3, and V_4. Whatever the case may be, the number of switching actions can be determined, with 3 in Case 1 and 4 in Case 2. The switch sequences for Case 2 in all sectors are shown in Table 3.3.

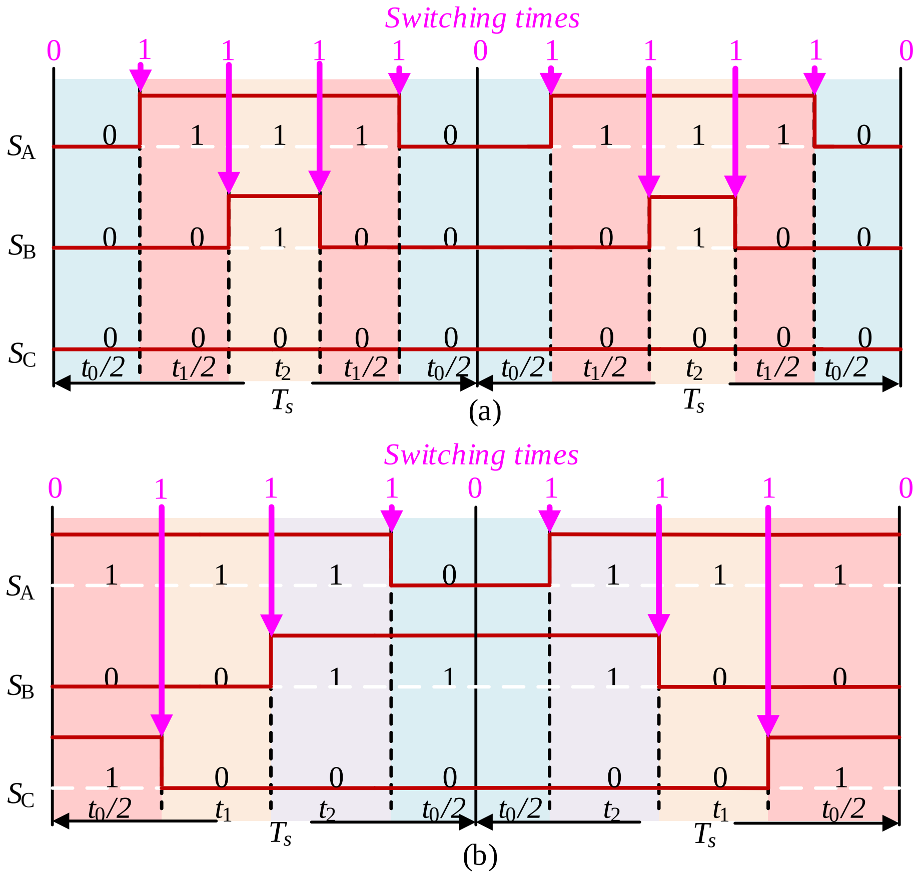

Fig. 3. 8. Case 1, three-phase switching sequences in Sector I. (a) Symmetrical three vectors. (b) Proposed method.

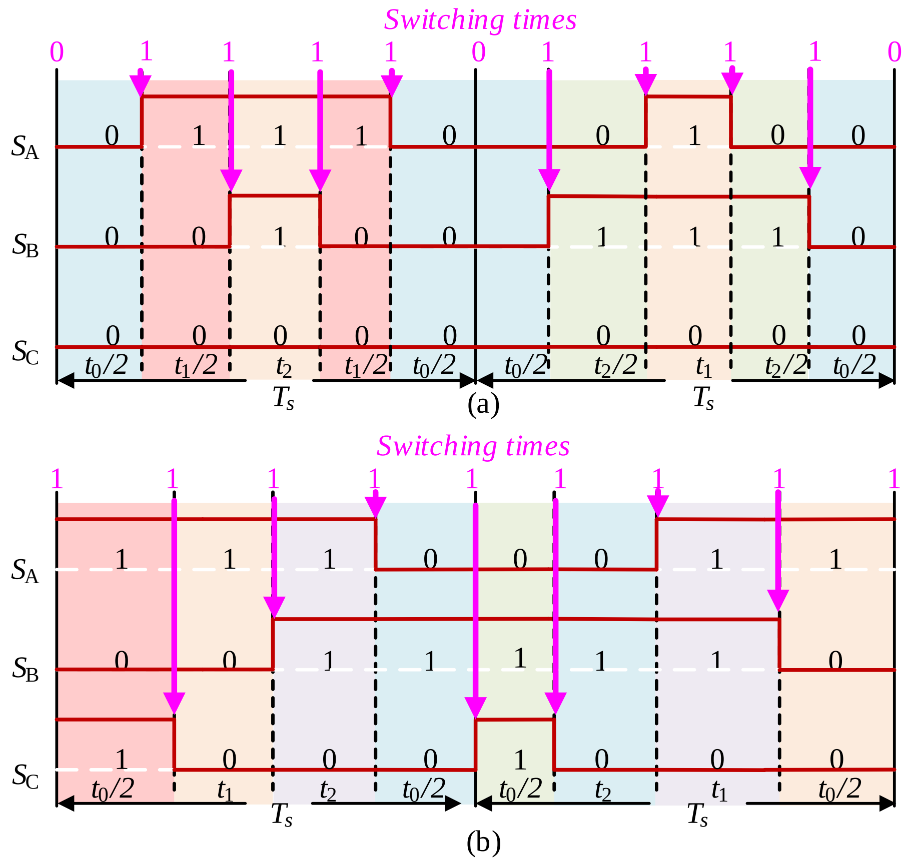

Fig. 3. 9. Case 2, three-phase switching sequences in Sector I. (a) Symmetrical three vectors. (b) Proposed method.

TABLE 3.3

CURRENT AND NEXT PERIOD VECTORS SEQUENCE FOR CASE 2

Sector switching	Current period vectors sequence	Next period vectors sequence
I→II	$V_6 \to V_1 \to V_2 \to V_3$	$V_4 \to V_3 \to V_2 \to V_1$
	$V_3 \to V_2 \to V_1 \to V_6$	$V_1 \to V_2 \to V_3 \to V_4$
II→III	$V_4 \to V_3 \to V_2 \to V_1$	$V_2 \to V_3 \to V_4 \to V_5$
	$V_1 \to V_2 \to V_3 \to V_4$	$V_5 \to V_4 \to V_3 \to V_2$
III→IV	$V_2 \to V_3 \to V_4 \to V_5$	$V_6 \to V_5 \to V_4 \to V_3$

	$V_5 \rightarrow V_4 \rightarrow V_3 \rightarrow V_2$	$V_3 \rightarrow V_4 \rightarrow V_5 \rightarrow V_6$
IV→V	$V_6 \rightarrow V_5 \rightarrow V_4 \rightarrow V_3$	$V_4 \rightarrow V_5 \rightarrow V_6 \rightarrow V_1$
	$V_3 \rightarrow V_4 \rightarrow V_5 \rightarrow V_6$	$V_1 \rightarrow V_6 \rightarrow V_5 \rightarrow V_4$
V→VI	$V_4 \rightarrow V_5 \rightarrow V_6 \rightarrow V_1$	$V_2 \rightarrow V_1 \rightarrow V_6 \rightarrow V_5$
	$V_1 \rightarrow V_6 \rightarrow V_5 \rightarrow V_4$	$V_5 \rightarrow V_6 \rightarrow V_1 \rightarrow V_2$
VI→I	$V_2 \rightarrow V_1 \rightarrow V_6 \rightarrow V_5$	$V_6 \rightarrow V_1 \rightarrow V_2 \rightarrow V_3$
	$V_5 \rightarrow V_6 \rightarrow V_1 \rightarrow V_2$	$V_3 \rightarrow V_2 \rightarrow V_1 \rightarrow V_6$

3.5. Execution Processes of the Developed Scheme

Based on the concepts and methods proposed in the previous section, the whole flow diagram of the developed scheme is given in Fig. 3. 10. The corresponding execution steps are as follows.

Step 1: Calculate the amplitude and angle of the reference voltage. Choose an appropriate threshold between 0 and $U_{dc}/\sqrt{3}$ to determine if the reference voltage amplitude exceeds.

Step 2: If the amplitude of the reference voltage vector u_s^{ref} > the switching threshold U_{sh}, the system is in dynamic operation and the single-vector method is adopted. Obtain output by selecting one of the six nonzero fundamental vectors as the optimal one. Otherwise, the proposed steady-state strategy with CMV suppression is employed.

Step 3: Judge whether the sector where the reference voltage is located has changed. If not, follow the treatment of Case 1, the selected voltage vectors are unchanged and the sequence order is reversed from the previous control cycle. If it switches to the adjacent sector, update the voltage vector selection according to the principle of Case 2. Clockwise and counterclockwise also alternate according to the previous control cycle.

Step 4: Calculate the duration of different voltage vectors by (3.11), output pulse sequence under the condition of Case 1 or Case 2.

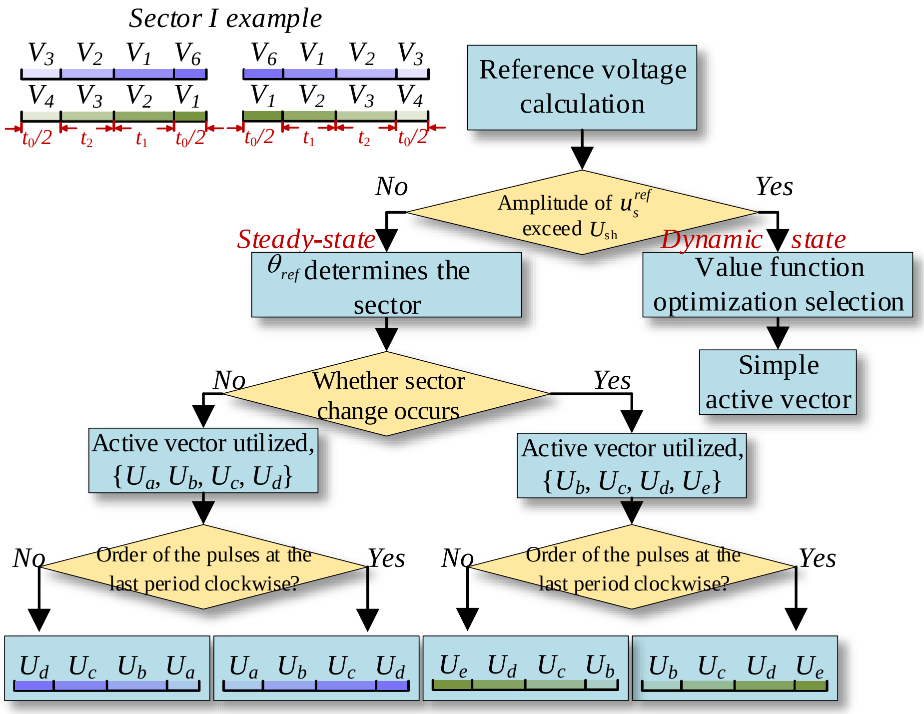

Fig. 3. 10. Flow diagram of the proposed Mode Switching MPC method.

3.6. Experimental Results

In this part, the proposed highly efficient MPC method with CMV suppression proposed in this chapter is verified. The comparison results are given based on an experimental platform, which is shown in Fig. 3. 11. dSpace 1202 is employed as the main controller for implementing the modified control algorithm. The sampling period of the control system is defined as 50 μs considering operational conditions. Tektronix

MDO 3024 mixed domain oscilloscope is used to record the experimental waveforms. The load motor is a three-phase SPMSM in which relevant parameters are listed in Table 3.4. Besides, the setup also includes a magnetic powder brake and a 5-kW dc power source.

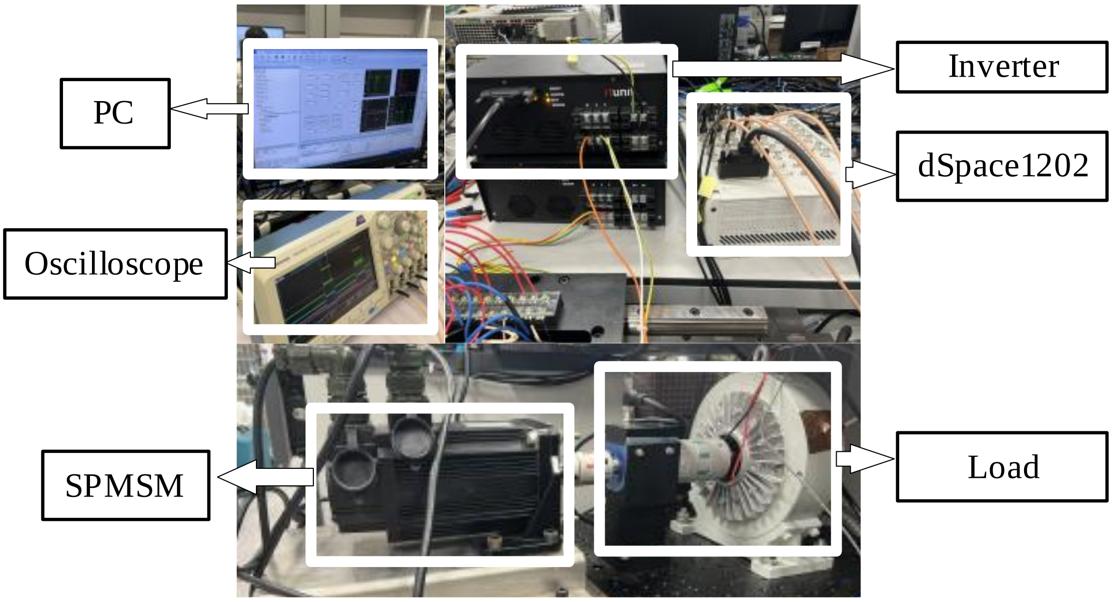

Fig. 3. 11. Experimental setup of SPMSM.

TABLE 3.4

PARAMETERS OF PMSM

Parameter	Value
Stator resistance R_s	0.65 Ω
Stator inductance L_s	1.55 mH
Rated speed n_N	1000 rpm
Rated torque T_e	6 Nm
Rated power P_N	600 W
Number of pole pairs p	4
Rotor flux linkage ψ_f	0.225 Wb

Rotational inertia J	$0.00086\ kg \cdot m^2$
Encoder resolution G_n	5000 PPR

3.6.1. Steady-State Performance Evaluation

To verify the correctness of the theoretical analysis, conduct experimental research when the motor is operating at 1000 r/min. The angle and sector distribution of the reference voltage vector and the waveform of the phase current are shown in Fig. 3. 12. It illustrates that the sector number periodically increases from 1 to 6 according to the angle of reference vector as the motor operating in the positive direction. This represents that the principle of the novel multivector modulated method is correct and works well.

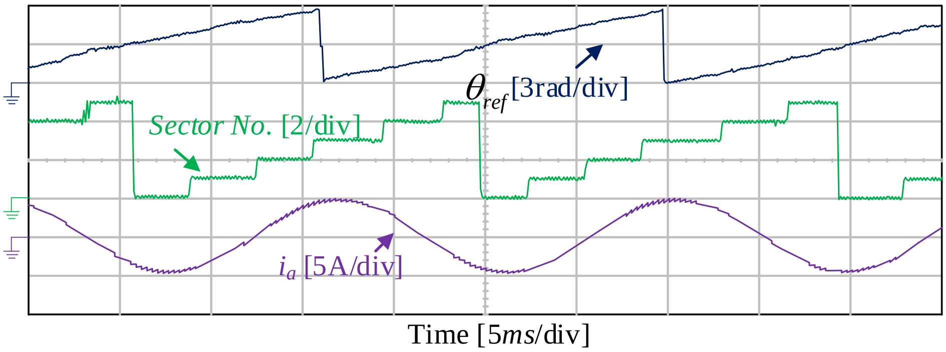

Fig. 3. 12. Vector reference angle and sector number at 1000 r/min for the proposed method.

In addition, in order to evaluate the effectiveness of the proposed method, comparative experiments are carried out. The improved three-vector (ITV-MPC) approach in [91], the single-vector MPC considering zero vector (CZV-MPC) in [118], and the proposed control strategy are applied under the same control frequency. The steady-state waveforms of the three methods are shown in Fig. 3. 13 under the conditions of both speeds of 1000 r/min and the same load. It can be seen from the steady-state results that the current quality of the proposed method is relatively good and the THD of ITV-MPC is the lowest. Although the experiments were conducted at the same control frequency, the actual switching frequencies of the three methods are not the same. After calculation, using the proposed method, the motor efficiency is 95.71% and the power factor is 0.937.

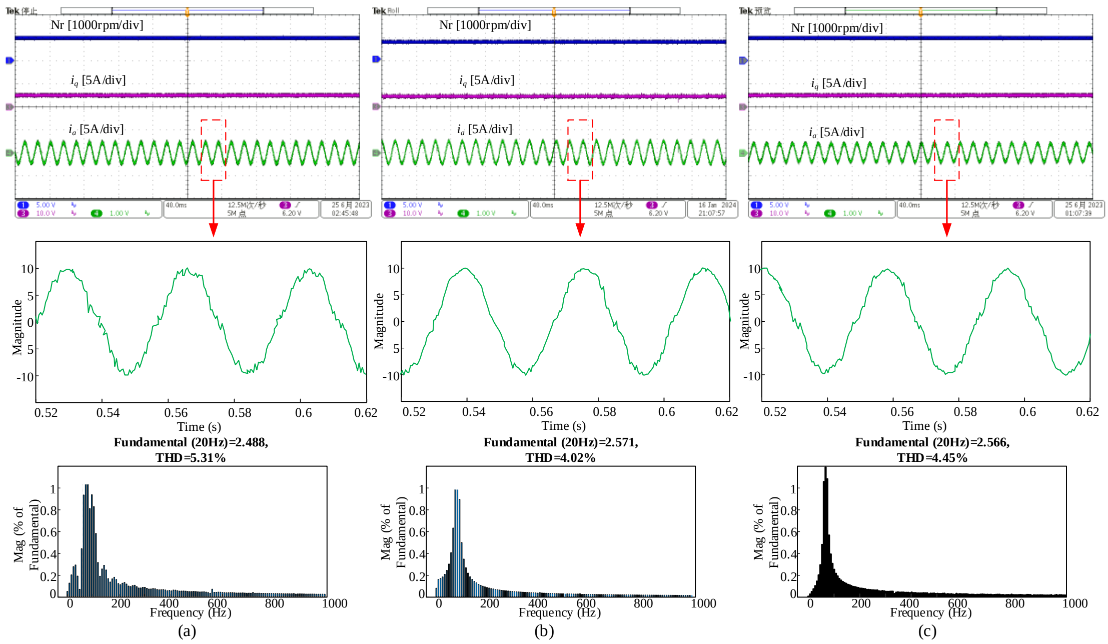

Fig. 3. 13. Experimental results of three methods at steady speed of 1000 r/min with the rated load. (a) CZV-MPC. (b) ITV-MPC. (c) Proposed method.

It can be seen from Fig. 3. 13 that in terms of motor speed, the fluctuations of all schemes are relatively small. In terms of electromagnetic torque, the ITV-MPC strategy has fewer ripples and better smoothness. In terms of current quality, the performances of ITV-MPC and the proposed method are almost identical. Under the above switching frequency conditions, the current THD results are obtained. Tektronix oscilloscope saved 10 000 sets of phase A current data (in.csv format) and imported them into MATLAB for Fast Fourier transform (FFT) analysis. The harmonic spectrum of the stator currents is also shown in Fig. 3. 13. The THD of the ITV-MPC strategy is the lowest, only 4.02%. As a comparison, the THD of the proposed strategy is 4.45%. Although the switching frequency of the proposed method is lower, the harmonic components of ITV-MPC and the proposed method are similar. As a single-vector MPC strategy, CZV-MPC has the highest THD of 5.31%. Fig. 3. 14 shows that the three control strategies calculate the switching frequency of all upper bridge arm switches every 0.05 s, and the control frequency of both strategies is 20 kHz. Obviously, the actual switching frequencies of the ITV-MPC and CZV-MPC strategies are not fixed, as there is no constraint on the set of switching states, resulting in a randomness in the selection of switching states corresponding to the voltage vector. The proposed strategy limits the sequence of switch states, allowing only one phase of the switch state to jump. Within a single control cycle, the switching frequency of all IGBTs in the upper bridge arm is fixed three times under Case 1, so it can be calculated that the switching frequency is always 1500 within 0.05 s. Therefore, the average switching frequency of the proposed strategy is 10 kHz. The average switching frequencies of the ITV-MPC and CZV-MPC are 13.98 and 5.65 kHz, respectively.

Furthermore, adjust the control frequency of ITV-MPC so that its switching frequency is at the same level as the proposed method. It is fair to compare the power quality of the two methods under this condition. For example, reduce the control frequency of ITV-MPC to 14.36 kHz at a speed of 1000 r/min so that its switching frequency is consistent with the proposed method, both are 10 kHz. Fig. 3. 15 demonstrates that under the same switching frequency, the proposed scheme has better steady-state performance. As the speed increases, the THD of the proposed method remains within 7%.

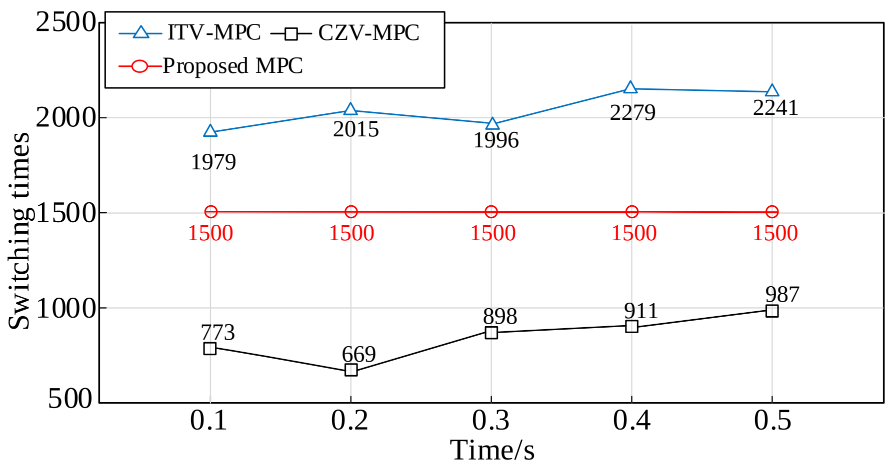

Fig. 3. 14. Switching times of the three methods within 0.05 s.

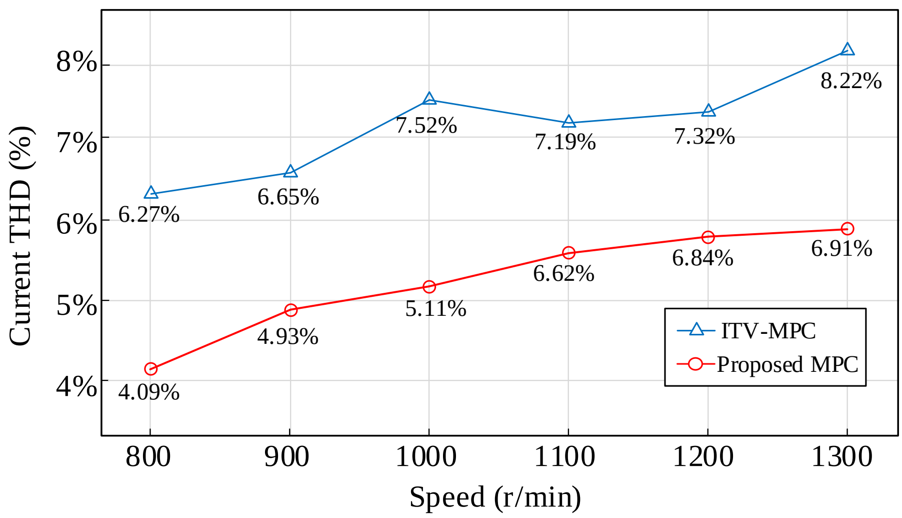

Fig. 3. 15. Comparison of current quality at different speeds for the same switching frequency.

In order to validate the output smoothness of the proposed method, comparative experiments were conducted at various motor speeds. The load is set to 0 Nm and the results are shown in Table 3.5. The dq-axis current ripples d_{rip} and q_{rip} are calculated by

$$d_{\mathrm{rip}}=\sqrt{\frac{1}{N}\sum_{k=1}^{N}\left(i_d(k)-\frac{1}{N}\sum_{k=1}^{N}i_d(k)\right)^2} \tag{3.12}$$

$$q_{\mathrm{rip}}=\sqrt{\frac{1}{N}\sum_{k=1}^{N}\left(i_q(k)-\frac{1}{N}\sum_{k=1}^{N}i_q(k)\right)^2} \tag{3.13}$$

where N is the sampling number of current in a period of 0.1 s under steady-state condition. And the root mean square (rms) error of torque ripple T_{rip} is

$$T_{\mathrm{rip}}=\sqrt{\frac{1}{N}\sum_{k=1}^{N}\left(T(k)-\frac{1}{N}\sum_{k=1}^{N}T(k)\right)^2}. \tag{3.14}$$

TABLE 3.5

OUTPUT RIPPLES EXPERIMENTAL RESULTS OF DIFFERENT METHODS

Out indicators	Control strategy	500r/min	1000r/min	1500r/min
T_{rip}/Nm	ITV-MPC	0.588	0.621	0.702
	Proposed method	0.579	0.635	0.714
d_{rip}/A	ITV-MPC	0.209	0.262	0.316
	Proposed method	0.217	0.249	0.331
q_{rip}/A	ITV-MPC	0.203	0.258	0.311
	Proposed method	0.214	0.252	0.319

Based on Table 3.5, there is a slight rise in the q_{rip} when the speed is 500 and 1500 r/min in the steady state. The proposed method reduces the ripple of the d-axis current by 4.9% at 1000 r/min speed. The torque ripple values for the proposed method are similar to ITV-MPC in all speed ranges. The above experimental results indicate that the strategy proposed in this thesis maintains good steady-state performance while suppressing CMV and reducing switching frequency.

3.6.2. Dynamic Response Performance Evaluation

Motor start experiments and speed mutation experiments were conducted under the same speed loop of the control system to verify the dynamic performance. To better demonstrate the highly efficient properties of the method proposed in this chapter, the switching threshold U_{sh} needs to choose an appropriate value. Fig. 3. 16 shows the change rules of torque ripples and switching frequency when U_{sh} is taken different values. According to Chapter 2, the value range is (0, $U_{dc} / \sqrt{3}$). Therefore, 8 points are selected to obtain the response results. The load torque is maintained at 1 Nm, and the reference speed increases evenly to the rated value. The experimental results show that the larger the U_{sh} selected for the proposed method, the lower the torque ripple and the higher the switching frequency, i.e., the novel multivector method is more often employed. On balance, U_{sh} is set to $U_{dc}/3$ based on the amplitude of the basic voltage vector of 2 U_{dc} /3. Fig. 3. 17 (a) shows three strategies' speed and current waveforms when the motor is started from a stationary state with a 0.8 Nm load. To highlight the dynamic performance of the proposed method in more depth, the speed transient test is carried out, and the experiment results are shown in Fig. 3. 17(b). The speed reference suddenly changes from 500 to 1000 r/min. The experimental results show that all three strategies can achieve a fast response, among which CZV-MPC follows the fastest, but has a large overshoot.

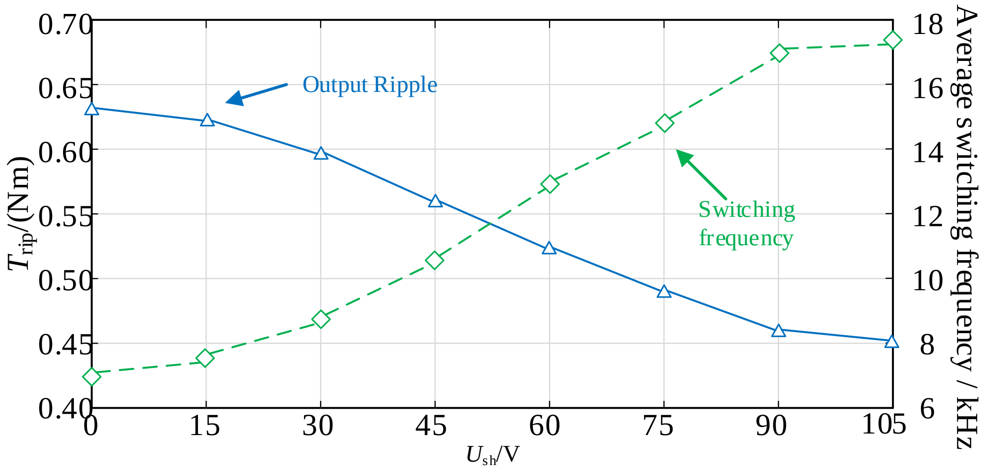

Fig. 3. 16. Variation rule of the switching threshold selection.

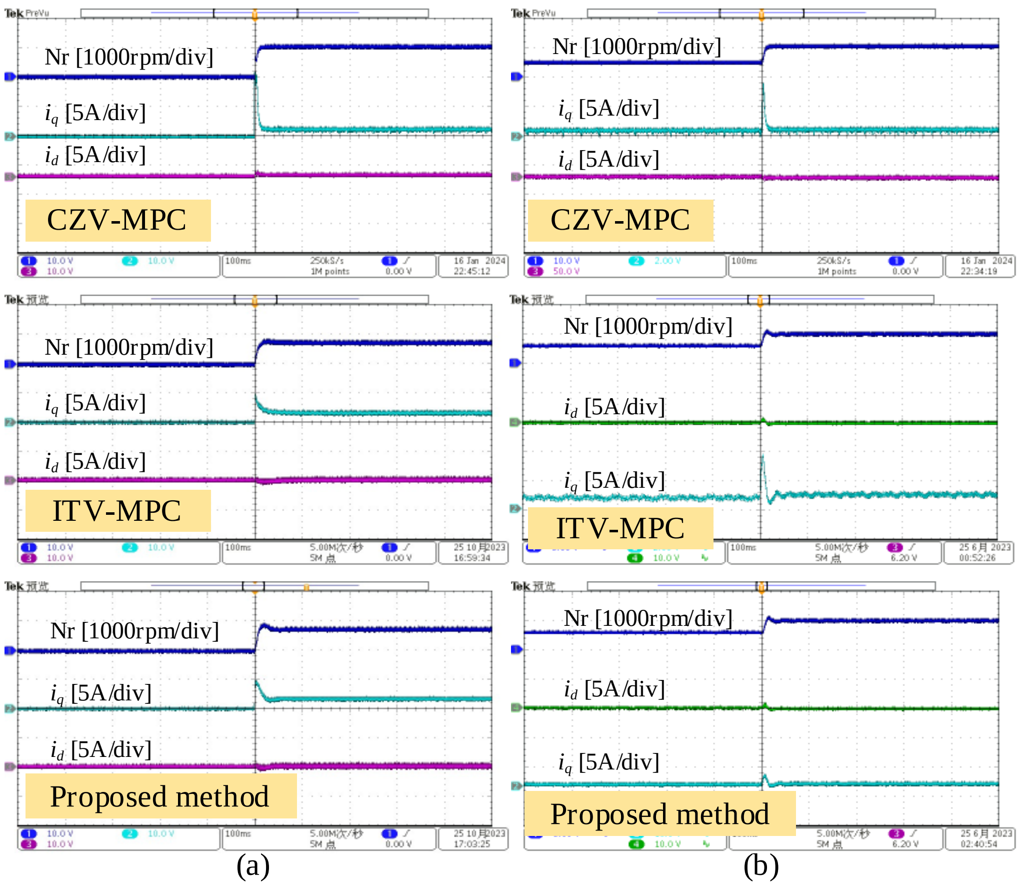

Fig. 3. 17. Experimental results under the transient conditions. (a) Starting with load.

(b) Reference speed suddenly changes under no load.

Fig. 3. 18 zooms in the transient states of the three methods. The transient speed oscillation in the initial stage is caused by the flexible coupling between the load machine and the PMSM. It can be observed that the rising times of the startup process are 29, 47, and 78 ms for CZV-MPC, the proposed method, and ITV-MPC, respectively. Considering the stable condition of q-axis current, the proposed method shows better results than ITV-MPC due to fewer basis vectors that need to be calculated. As shown in Fig. 3. 18(b), the time durations required are almost equal for CZV-MPC and the proposed method during the commanded change in speed. Hence, the method proposed in this thesis is superior in high-efficient output while inheriting a high dynamic response from single-vector MPC. The torque and speed tracking performance has certain advantages.

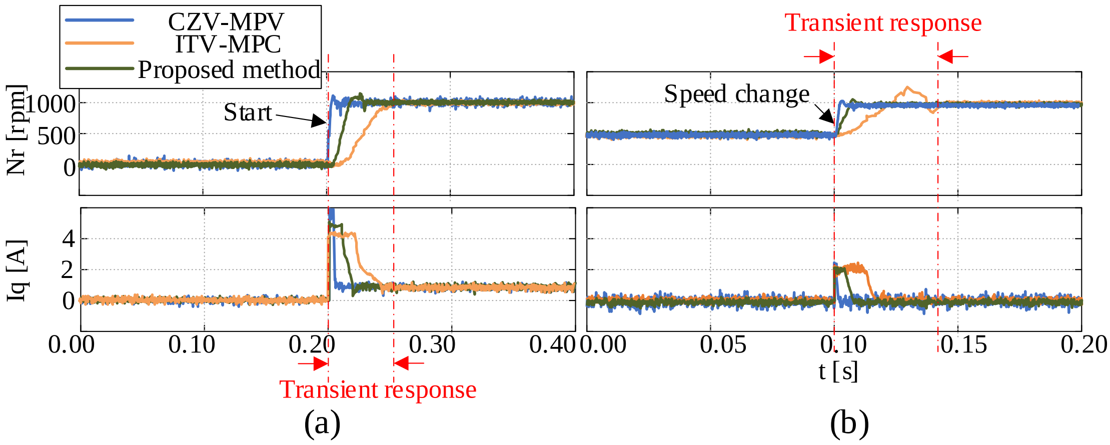

Fig. 3. 18. Comparison on dynamic response by using the three control methods. (a) Motor starting. (b) Speed change.

3.6.3. CMV Suppression Effect Evaluation

To verify the CMV suppression ability of the proposed high-efficient MPC method, a comparative experiment was conducted between the proposed method and ITV-MPC.

As the waveforms of CMV shown in Fig. 3. 19(a), due to the use of zero voltage vectors in ITV-MPC methods, there existed CMV with an amplitude of $\pm U_{dc}/2$. After the proposed method was put into use, CMV was effectively suppressed, with a maximum of only $\pm U_{dc}/6$. Fig. 3. 19 (b) shows that on the premise of suppression effect of CMV, this method maintains low output ripples during motor operation. Fig. 3. 20 illustrates the peak-to-peak value of the CMV. The original CMV is within the range of $\pm U_{dc}/2$ and has been reduced to 50 V with the proposed method.

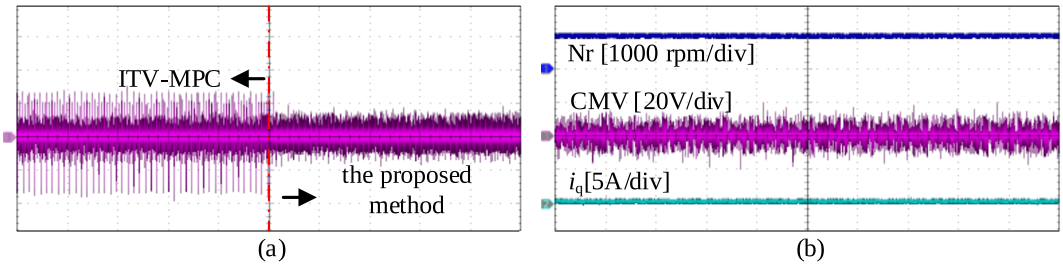

Fig. 3. 19. Waveforms of CMV. (a) Comparison of CMV under different methods. (b) Steady state performance.

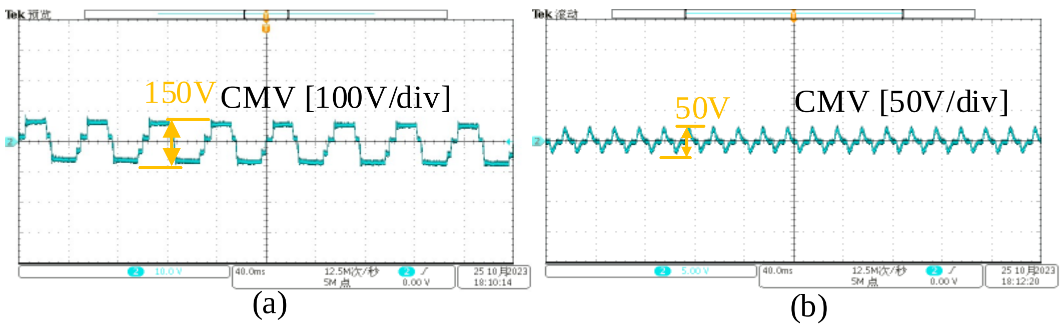

Fig. 3. 20. CMV amplitude before and after suppression. (a) Before suppression. (b) After suppression.

3.6.4. Robustness Performance Evaluation

As an MPC control strategy, the normal operation of the proposed high-efficient method relies on the accurate model and parameters of the controlled object. The motor parameter mismatch experiments are conducted in this section to verify the robustness of the proposed method. Fig. 3. 21 illustrates the steady-state control performance for a 10% error in the stator resistance, stator inductance, and permanent magnet chain, and the working conditions are the same as Fig. 3. 13. Comparing the waveforms without parameter error, the average torque ripple is 0.677 Nm, while in the presence of parameter mismatch, the average torque ripple increases to 0.802 Nm. Despite the performance degradation, the system is still able to operate normally, and parameter robustness is verified.

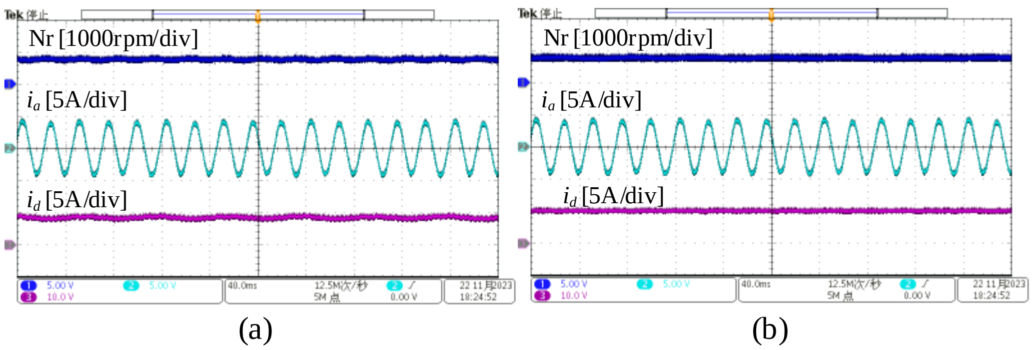

Fig. 3. 21. Experimental comparison of steady-state operation of motors with or without parameter errors. (a) Proposed method has parameter error of 10%. (b) When parameters are accurate.

3.7. Conclusion

In this chapter, a highly efficient multivector strategy with CMV suppression is proposed for motor drive. Two voltage vector generation methods for reference voltages with different amplitudes when operating state changes are alternately used. A novel voltage vector synthesis method applied in the steady state is presented, which minimizes switching times. Zero vectors are not used directly but are synthesized by two adjacent active vectors and placed at the beginning and end of each control period. Accurate dynamic adjustment can be achieved through simple conditional judgment. The proposed highly efficient MPC scheme has been carried out and compared with existing improved MPC algorithms.

The experimental results verify that the proposed method can restrict the CMV within $\pm U_{dc}/6$. While retaining the dynamic performance advantages of typical single-state operation MPC, the proposed method also ensures lower switching frequency and output ripples. The overall performance of the proposed MPC scheme makes it suitable for transportation motor drive systems and other highly efficient industrial applications. Future work will focus on how to reduce system parameter dependence or perform parameter identification.

CHAPTER 4. PROPOSED THREE-LEVEL FS-MPC METHOD OF MAPPING TO SUB-HEXAGONS

4.1. Introduction

Three-level NPC inverters have the advantages of high number of levels, low harmonics, low switching frequency and low switching loss, which are suitable for high voltage and high-power scenarios. However, compared with the traditional two-level inverter, the three-level inverter has a more complex structure and can issue more number of vectors. In order to reduce the burden of FS-MPC computation and maintain the reliable operation of the PMSM drive system, a revised strategy is proposed. In revised FS-MPC (RFS-MPC), a deadbeat MPC strategy is applied to convert the cost function for minimizing the stator current tracking error to the cost function for minimizing the stator voltage tracking error. An efficient location determination method is introduced to map the reference voltage vector onto the subhexagon. As a result, the candidate region becomes narrower, and the number of computations is significantly reduced.

4.2. Topology and Switching States of 3L-NPC Inverter

Fig. 4. 1 shows the topology of the 3L-NPC inverter, V_{dc} is constant DC bus voltage, U_{C_1} and U_{C_2} are DC-link bus top and bottom capacitor voltages respectively. The two

capacitors (C_1 and C_2) are charged to half of the DC bus voltage. Variables U_a, U_b and U_c respectively express the outputs of ABC three-phase arms.

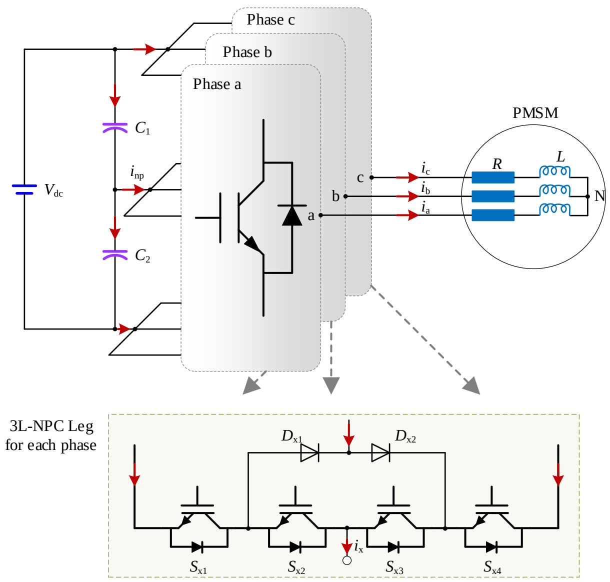

Fig. 4. 1. Topology of three-level NPC inverter.

Taking Phase A as an example, the four IGBTs, (S_{a1},S_{a3}) and (S_{a2},S_{a4}), are complementary switching pairs, with only half the voltage stress on each IGBT compared to the two-level inverter. Each phase arm, therefore, has three switching states, the corresponding output value of U_a (U_b or U_c) maybe $-V_{dc}/2$, 0 or $V_{dc}/2$. For convenience, $-V_{dc}/2$, 0 and $V_{dc}/2$ are labeled as N, O and P. It can be calculated that there are a total of $3^3=27$ switching states for the three-phase outputs, and their directions and amplitudes in the $\alpha\beta$ stationary coordinate system are shown in Fig. 4. 2.

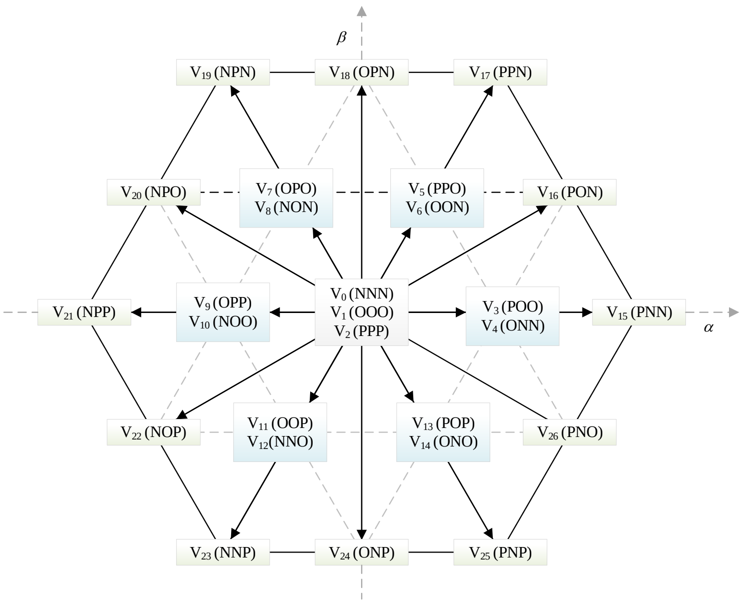

Fig. 4. 2. Three-level vector plot.

4.3. Predictive Model Based on Deadbeat Principle

In terms of the principle of deadbeat control, the predictions of *dq*-axis stator currents in (*k*)-th instant can be assumed to reach their reference values. As a result, current prediction equations can be modified as

$$\begin{cases} i_d^* = i_d^k + \left(u_d^k - R_s i_d^k + pL\omega_r^k i_q^k\right)T_s / L \\ i_q^* = i_q^k + \left(u_q^k - R_s i_q^k - p\omega_r^k\left(Li_d^k + \psi\right)\right)T_s / L \end{cases} \tag{4.1}$$

According to the principle of maximum torque per ampere, i_d^* is set to zero. The *dq*-axis stator voltages u_d^k and u_q^k in (4.1) can be regarded as the desired references u_d^* and u_q^*, which can be deduced as

$$\begin{cases} u_d^* = R_s i_d^k - L\dfrac{i_d^k}{T_s} - L\omega_e^k i_q^k \\ u_q^* = R_s i_q^k + L\dfrac{i_q^* - i_q^k}{T_s} + L\omega_e^k i_d^k + \psi\omega_e^k \end{cases} \tag{4.2}$$

where u_d^* and u_q^* are assumed to keep constant within every control cycle. Accordingly, the cost function can be defined as

$$g_2 = \left|u_d^* - u_d^i\right| + \left|u_q^* - u_q^i\right|, i = 0,1,2,\ldots,26. \tag{4.3}$$

From the above analysis, it can be seen that instead of multiple predictions in FS-MPC, the reference voltage is calculated only once during every control cycle. The execution time is reduced than that of the FS-MPC. Even so, a total of 27 elementary voltage vectors (including 8 redundant voltage vectors) needs to be evaluated by (4.3), which is still causing a heavy calculation time. To further relieve the computational burden, it is effective to reduce the number of candidate elementary vectors, provided that the performance of the control system is not degraded. Through inverse Park transformation, the reference voltage vector is converted to the $\alpha\beta$ plane for sector judgment.

$$\begin{gathered}\begin{bmatrix} V_{\mathrm{ref}}^{\alpha} \\ V_{\mathrm{ref}}^{\beta} \end{bmatrix} = \begin{bmatrix} \cos\theta_{\mathrm{e}} & -\sin\theta_{\mathrm{e}} \\ \sin\theta_{\mathrm{e}} & \cos\theta_{\mathrm{e}} \end{bmatrix} \begin{bmatrix} u_d^* \\ u_q^* \end{bmatrix} \\ V_{\mathrm{ref}} = V_{\mathrm{ref}}^{\alpha} + jV_{\mathrm{ref}}^{\beta}. \end{gathered} \tag{4.4}$$

4.4. Sub-hexagon Mapping Rules in Three-Level Vector Space

To further simplify the localization and narrow the scope of the optimization search, the rule of mapping the three-level vectors into sub-hexagons is adopted. Unlike the traditional triangular subsector dividing approach [119], the one taken in this thesis is the only one applicable to the subsequent scheme. As shown in Fig. 4. 3, the original reference voltage vector V_{ref} in the stationary $\alpha\beta$-axis is mapped as $V_{\mathrm{sub-ref}}$ in sub-hexagon I, which can be expressed as the difference between V_{ref} and the corresponding sub-hexagon center vector:

$$V_{\text{sub-ref}} = V_{\text{ref}} - u_{cv} \tag{4.5}$$

where u_{cv} (cv = 1, 2, 3, 4, 5, 6) is the center vector according to the sector where the reference voltage vector lies.

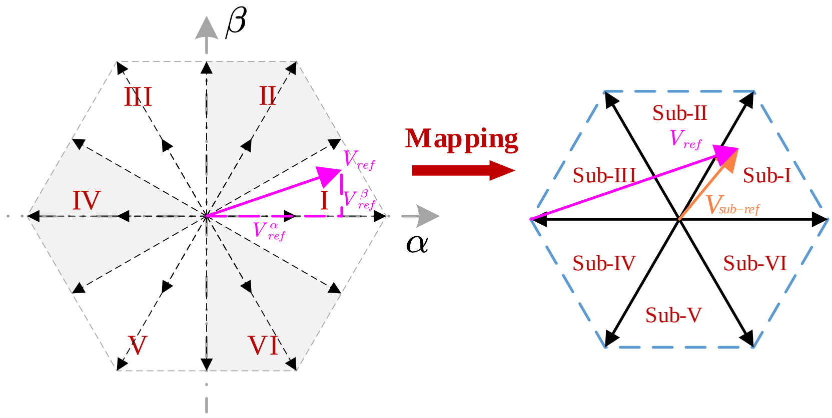

Fig. 4. 3. Diagram of the original voltage vector and the mapping process.

Based on the length and angle of V_{ref}, it is possible to determine adjacent vectors directly. In order to facilitate the digital implementation of the algorithm, the following specific indicators are designed to determine geometric relationships based on a certain number of conditions. Here, the intermediate voltage variables V_X, V_Y, and V_Z are introduced, and their definitions are shown in (4.6). Define the intermediate indicator variables X, Y, Z and N according to the positive and negative values of the intermediate voltage variables, as shown in (4.7).

$$\begin{cases} V_{\mathrm{X}} = V_{\mathrm{ref}}^{\alpha} \\ V_{\mathrm{Y}} = 3V_{\mathrm{ref}}^{\beta} - \sqrt{3}V_{\mathrm{ref}}^{\alpha} \\ V_{\mathrm{Z}} = -3V_{\mathrm{ref}}^{\beta} - \sqrt{3}V_{\mathrm{ref}}^{\alpha} \end{cases} \tag{4.6}$$

$$\begin{aligned} X &= \begin{cases} 1, & \text{if } V_{\mathrm{X}} \geq 0 \\ 0, & \text{if } V_{\mathrm{X}} < 0 \end{cases} \\ Y &= \begin{cases} 1, & \text{if } V_{\mathrm{Y}} \geq 0 \\ 0, & \text{if } V_{\mathrm{Y}} < 0 \end{cases} \\ Z &= \begin{cases} 1, & \text{if } V_{\mathrm{Z}} \geq 0 \\ 0, & \text{if } V_{\mathrm{Z}} < 0 \end{cases} \\ N &= 4Z + 2Y + X. \end{aligned} \tag{4.7}$$

Calculating the value of N uniquely determines the sector where V_{ref} is located. Taking sub-hexagon I as an example, $V_{\mathrm{X}} \geq 0$, $V_{\mathrm{Y}} < 0$, $V_{\mathrm{Z}} < 0$, and thus $X = 1$, $Y = 0$, $Z = 0$, $N = 1$. The corresponding relationship between the subhexagon number and the values of the intermediate indicator variables X, Y, Z, and N is shown in Table 4.1.

TABLE 4.1

CORRESPONDING RELATIONS BETWEEN SUB-HEXAGON AND INTERMEDIATE INDEXES

Sub-hexagon	I	II	III	IV	V	VI
X	1	1	0	0	0	1
Y	0	1	1	1	0	0
Z	0	0	0	1	1	1
N	1	3	2	6	4	5

To further pinpoint the positioning, continue sectoring in the sub-hexagons. The small sector number where $V_{\mathrm{sub-ref}}$ is located can be determined as follows:

$$
\begin{cases}
V_{\text{X-sub}} = V_{\text{sub-ref}}^{\beta} \\
V_{\text{Y-sub}} = 3V_{\text{sub-ref}}^{\alpha} - \sqrt{3}V_{\text{sub-ref}}^{\beta} \\
V_{\text{Z-sub}} = -3V_{\text{sub-ref}}^{\alpha} - \sqrt{3}V_{\text{sub-ref}}^{\beta}
\end{cases}
\tag{4.8}
$$

$$
\begin{gathered}
X_{sub} = \begin{cases} 1, \text{if } V_{\text{X-sub}} > 0 \\ 0, \text{if } V_{\text{X-sub}} \le 0 \end{cases} \\
Y_{sub} = \begin{cases} 1, \text{if } V_{\text{X-sub}} > 0 \\ 0, \text{if } V_{\text{X-sub}} \le 0 \end{cases} \\
Z_{sub} = \begin{cases} 1, \text{if } V_{\text{Z-sub}} > 0 \\ 0, \text{if } V_{\text{Z-sub}} \le 0 \end{cases} \\
M = 4Z_{\text{sub}} + 2Y_{\text{sub}} + X_{\text{sub}}.
\end{gathered}
\tag{4.9}
$$

Similarly, the correspondence of M is shown in Table 4.2. After the above series of processes, the reference voltage vector is accurately positioned in a small sector of the sub-hexagon. At this time, the number of predictions has been greatly reduced, and only three adjacent vectors in the small sector need to be evaluated, and the optimal candidate vector among them is determined based on the nearest distance principle. This approach redefines the cost function and avoids the tedious process of repeated predictions.

TABLE 4.2

CORRESPONDING RELATIONS BETWEEN SMALL SECTORS AND INTERMEDIATE INDEXES

Small sector	I	II	III	IV	V	VI
X_{sub}	1	1	1	0	0	0
Y_{sub}	1	0	0	0	1	1
Z_{sub}	0	0	1	1	1	0
M	3	1	5	4	6	2

4.5. Simulation Results

The driving system of NPC-type three-level inverter is built in Matlab/Simulink, and the simulation models of conventional single-vector current predictive control and the RFS-MPC proposed in this chapter are realized respectively to compare the two methods. The simulation is done with Fixed-step, Solver using ode3 (Bogacki-Shampine), and the simulation time is 2s.

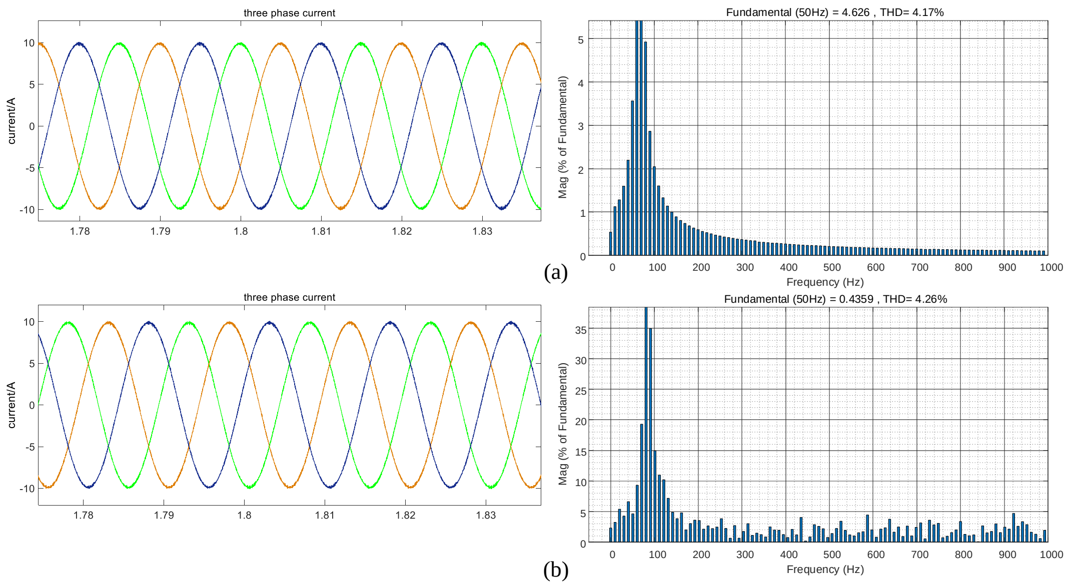

Fig. 4. 4. Stator current waveforms and FFT analysis of 2 control strategies. (a) Conventional single-vector method. (b) RFS-MPC.

First let the motor work at a steady state of 1000r/min. Fig. 4. 4 illustrates the stator current waveforms and their corresponding Fourier analysis results under two control strategies. It can be observed from the figure that the Total Harmonic Distortion (THD) content for the single vector model predictive control strategy is 4.17%, which is only

0.07% lower than the 4.26% THD achieved by the proposed RFS-MPC. This demonstrates that, despite employing a more simplified vector selection strategy, the RFS-MPC can achieve steady-state performance comparable to that of the conventional single vector strategy.

Fig. 4. 5 shows the *q*-axis current waveforms for both control strategies at the same load. When the conventional single vector model predictive control strategy is used, the peak-peak value of q-axis current is about 0.35 A. The peak-peak value of RFS-MPC is also about 0.35A, which has the same excellent steady state performance, and the variation frequency is lower, and the random pulsation is less.

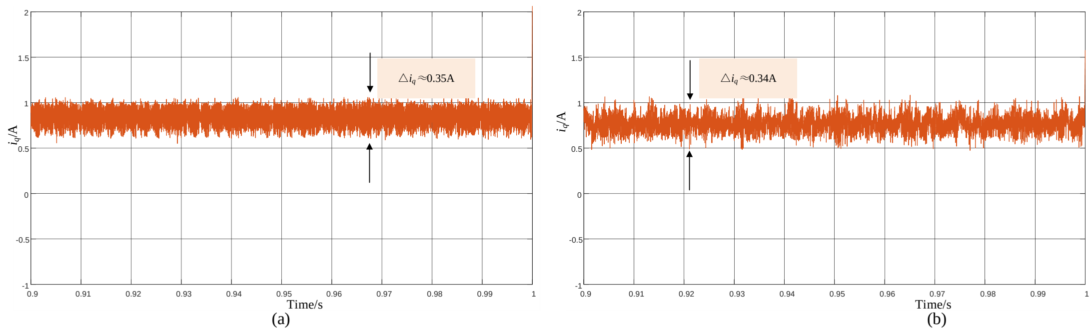

Fig. 4. 5. *q*-axis current waveforms of 2 control strategies. (a) Conventional single-vector method. (b) RFS-MPC.

Furthermore, to evaluate the dynamic performance of the control strategy, a no-load start-up simulation experiment of the motor was conducted. The speed reference was set to 1000 r/min, and the simulation waveforms using the traditional single-vector model predictive control are illustrated in Fig. 4. 6. As evident from the figure, the system exhibits a smooth start-up; the motor speed and three-phase current both show no overshoot. The speed swiftly follows the reference, while the current waveforms remain stable. Once stable, the average electromagnetic torque output is measured to be 0 N·m.

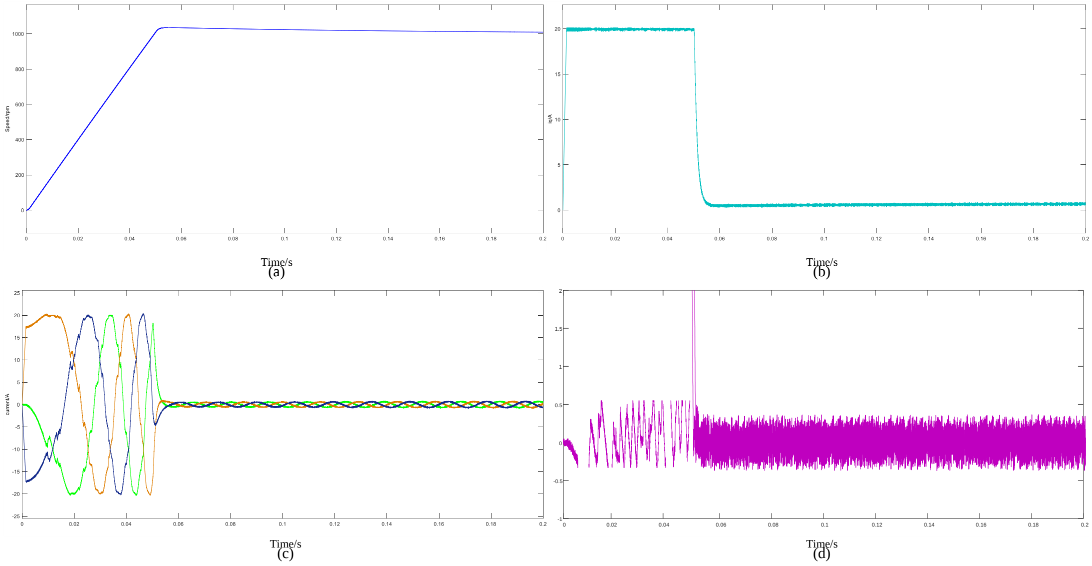

Fig. 4. 6. Dynamic response waveforms of conventional single-vector FC-MPC.

(a) Speed. (b) i_q. (c) three phase current. (d) i_d.

Fig. 4. 7 illustrates the waveforms of the motor during no-load start-up using the proposed RFS-MPC control strategy. As observed from the figure, the step response time is approximately 0.0035 s, indicating a significant improvement in dynamic response capability. In comparison to traditional approaches, RFS-MPC eliminates a considerable amount of predictive calculations for basic voltage vectors, making the optimization process for the optimal voltage vector more efficient.

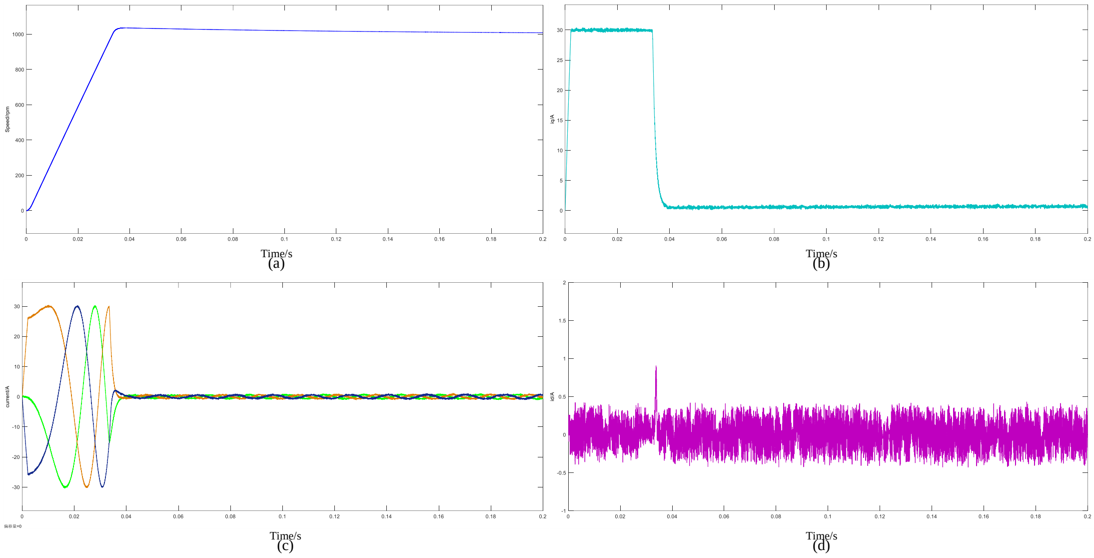

Fig. 4. 7. Dynamic response waveforms of proposed RFS-MPC. (a) Speed. (b) i_q. (c) three phase current. (d) i_d.

4.6. Conclusion

This chapter begins by introducing the basic topology of the NPC-type three-level inverter. It utilizes indicative parameters to map the reference voltage vector into a more precise range. Based on the control characteristics of PMSMs and system constraints, a cost function is designed, effectively enabling the rapid iteration of the FS-MPC algorithm within the three-level space vector framework. Validation shows that this control algorithm does not require complex parameter design, while also reducing computational complexity and significantly improving current tracking speed.

CHAPTER 5. PROPOSED MODEL PREDICTIVE CONTROL OF THREE-LEVEL NPC INVERTER-FED PMSM DRIVES BASED ON A NOVEL VECTOR-SELECTIOB SCHEME

5.1. Introduction

Existing model predictive control (MPC) methods mostly adopt multi-vector mode to achieve better steady-state control performance. But this increases system complexity, especially for three-level inverters. In addition, various vector combinations need to be evaluated in the cost function, and cumbersome tuning of weighting factors is also involved when the common-mode voltage (CMV) and neutral point potential (NPP) imbalance issues are considered. This chapter proposes a novel multi-vector-based MPC scheme to deal with these challenges. The key is to map the reference voltage vector to sub-hexagons, and the candidate region is narrowed down. Then, the dwell time of the determined voltage vectors is obtained from the cost function, which minimizes the error between the predicted reference voltage vector and the synthesis vector. In addition, the basic vectors with higher CMV amplitudes are reconstructed, and the NPP imbalance is addressed due to the employment of a hysteresis controller.

5.2. Analysis of NPP Imbalance and CMV Generation

5.2.1. Neutral Point Potential Imbalance

Based on the topology of the NPC three-level inverter, the causes of neutral point potential (NPP) imbalance can be derived. The system controls the NPC three-level inverter to output different voltage vectors based on the required demand. During this process, the DC source repeatedly charges or discharges the two capacitors, resulting in varying charging and discharging currents at the neutral point. As a consequence, the voltages across the two capacitors cannot remain balanced, leading to neutral point potential imbalance.

As illustrated in Fig. 5. 1, we can observe that for a 3L-NPC inverter, a total number of 27 switching states are available. Out of which, 6 are large voltage vectors (LVV) of the amplitude. When these vectors are applied, the three phases are either connected to the positive or negative rail and the loads are not connected to the neutral point. Therefore, LVVs do not cause a change in the neutral point voltage. For the 3 zero voltage vectors (ZVV), all three phase loads are short circuited to the same rail and thus do not affect the NPP either. For the 6 medium (MVV) and 12 small vectors (SVV), at least one of the three phases is connected to the neutral point of the capacitor and forms a current with the positive and negative rail of the DC supply.

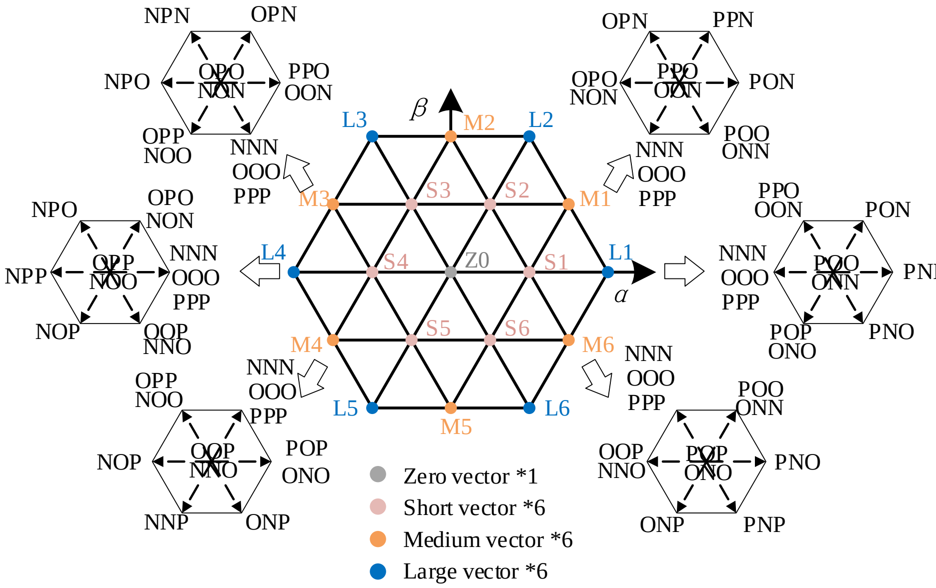

Fig. 5. 1. Space voltage vectors diagram and 27 output states for the three-level inverter.

When the MVV or the SVV are applied, the upper capacitor C_1 and the lower capacitor C_2 are charged and discharged by the current I_{np}, thus causing the NPP drift. Each pair of redundant SVVs has the opposite polarity of the I_{np} although the output voltage state is the same, so they can be used to mitigate the NPP drift caused by the MVVs. All the 27 switching states and different types of voltage vectors can be found in Table 5.1. Fig. 5. 2 takes the switching states of V_3 and V_4 as an example to explain the relationship between the neutral point current and the phase currents.

Fig. 5. 1 shows that the positions of V_3 and V_4 are the same, but the effect on NPP is just opposite. Define SVV connected to the positive end of the DC bus like V_4 as a positive small voltage vector (SVV(+)), and SVV connected to the negative end of the DC bus like V_3 as a negative small voltage vector (SVV (-)).

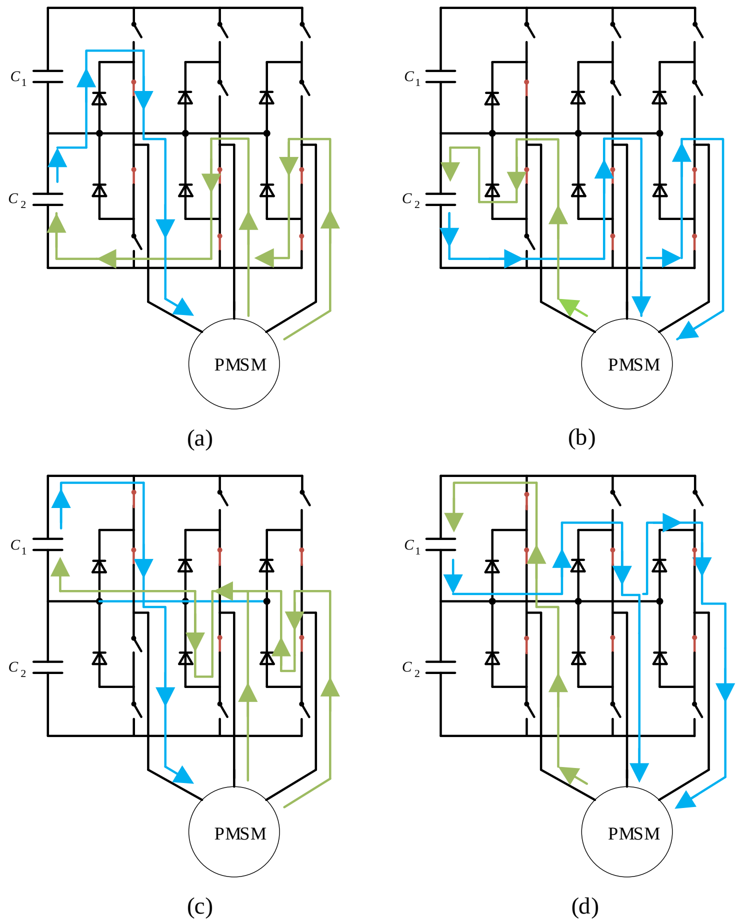

Fig. 5. 2. SVVs operating states and their corresponding neutral point currents.

(a)V_4(ONN),$I_a > 0$ (b) V_4 (ONN), $I_a < 0$ (c) V_3 (POO), $I_a > 0$

(d) V_3 (POO), $I_a < 0$.

TABLE 5.1

SWITCHING STATES AND ITS CORRESPONDING NEUTRAL CURRENT

Vector categories	Voltage level	Switching state and neutral current		
ZVV	0 (Null)	V_0(NNN) 0	V_1(OOO) 0	V_2(PPP) 0
SVV	$V_{dc}/3$	V_3(POO) $-I_a$	V_7(OPO) $-I_b$	V_6(OON) $-I_c$
		V_4(ONN) I_a	V_8(NON) I_b	V_5(PPO) I_c

		V_{10}(NOO)	V_{14}(ONO)	V_{11}(OOP)
		$-I_a$	$-I_b$	$-I_c$
		V_9(OPP)	V_{13}(POP)	V_{12}(NNO)
		I_a	I_b	I_c
MVV	$V_{dc}/\sqrt{3}$	V_{18}(OPN)	V_{16}(PON)	V_{20}(NPO)
		I_a	I_b	I_c
		V_{24}(ONP)	V_{22}(NOP)	V_{26}(PNO)
		I_a	I_b	I_c
LVV	$2V_{dc}/3$	V_{15}(PNN)	V_{17}(PPN)	V_{19}(NPN)
		0	0	0
		V_{21}(NPP)	V_{23}(NNP)	V_{25}(PNP)
		0	0	0

5.2.2. Common Mode Voltage Problem

The CMV is essentially the zero-sequence component widely present in inverters and is defined as the potential difference between the load neutral and the reference ground.

$$\begin{aligned} V_{AO} &= V_{AN} + V_{NO} \\ V_{BO} &= V_{BN} + V_{NO} \\ V_{CO} &= V_{CN} + V_{NO} \end{aligned} \tag{5.1}$$

where, V_{AN}, V_{BN} and V_{CN} are the three phases voltages, and V_{AO}, V_{BO} and V_{CO} are the pole voltages. V_{NO} is the voltage difference between the neutral point of the PMSM and the neutral point of the capacitors. As for a balanced three-phase system, the sum of the three-phase voltages is zero. Thus, the definition of V_{CMV} is

$$V_{CMV} = \frac{V_{AO} + V_{BO} + V_{CO}}{3} \tag{5.2}$$

According to (5.2), the CMVs for the 27 voltage vectors are listed in Table 5.2. It is shown that MVVs and V_1(OOO) produce zero CMV, and if space vectors with larger CMVs are aborted, CMV can be controlled within $\pm V_{dc}/3$.

TABLE 5.2

SPACE VECTORS AND CORRESPONDING CMV

LVV	V_{CMV}	MVV	V_{CMV}	SVV(+)	V_{CMV}	SVV(-)	V_{CMV}	ZVV	V_{CMV}
V_{15}	$-V_{dc}/6$	V_{16}	0	V_4	$-V_{dc}/3$	V_3	$V_{dc}/6$	V_0	$-V_{dc}/2$
V_{17}	$V_{dc}/6$	V_{18}	0	V_5	$V_{dc}/3$	V_6	$-V_{dc}/6$	V_1	0
V_{19}	$-V_{dc}/6$	V_{20}	0	V_8	$-V_{dc}/3$	V_7	$V_{dc}/6$	V_2	$V_{dc}/2$
V_{21}	$V_{dc}/6$	V_{22}	0	V_9	$V_{dc}/3$	V_{10}	$-V_{dc}/6$		
V_{23}	$-V_{dc}/6$	V_{24}	0	V_{12}	$-V_{dc}/3$	V_{11}	$V_{dc}/6$		
V_{25}	$V_{dc}/6$	V_{26}	0	V_{15}	$V_{dc}/3$	V_{14}	$-V_{dc}/6$		

5.3. Multi-Vector Strategy and Dwell Time

In the previous subsection, the synthesis of SVV was accomplished using ZVV and LVVs. In contrast to the use of SVV(-) in place of SVV(+), the proposed scheme does not produce a neutral point current in the synthesized SVVs because the ZVV and LVVs do not produce a current at the neutral point. However, in order to achieve a purposeful regulation of the NPP, it is necessary to recombine a set of fundamental vectors that act opposite the NPP and to design a controller that does not need to take into account the system parameters. The whole control diagram is illustrated in Fig. 5. 3.

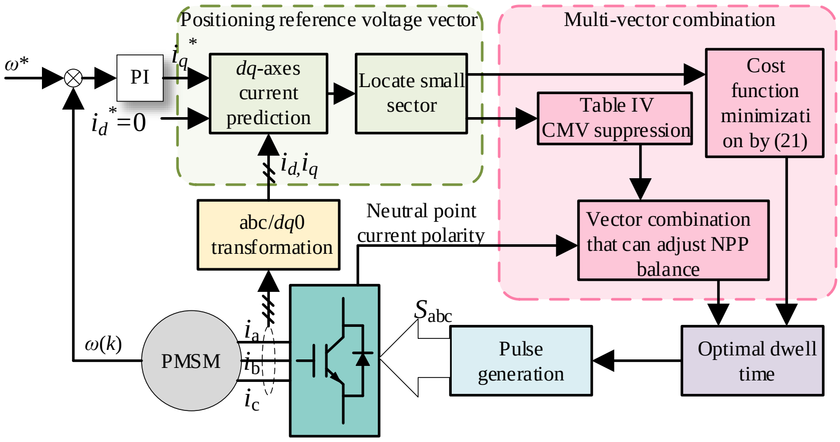

Fig. 5. 3. Control diagram of the proposed method.

5.3.1. Principle of the Proposed Multi-Vector Strategy

When the 3L-NPC inverter drives the PMSM, the three-phase bridge arm output voltage is related to the direction of the load current. Fig. 5. 4 shows the position of the voltage space vector and the direction of the three-phase current at this time. Taking the angle of V_{ref} as 15°, mapped to the sub-hexagon I. The directions of the ABC three-phase currents are + − −.

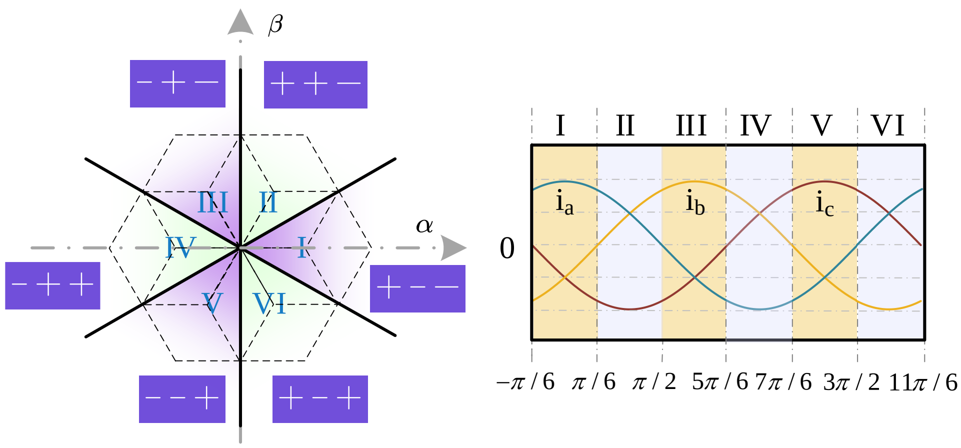

Fig. 5. 4. Direction of Three-phase Current in the Voltage Vector Figure.

In the previous subsection, we analyzed the effects of various voltage vectors on the NPP balance. Taking the MVV V_{16}(PON) as an example, during its dwell time T_m, the charge q_{T_m} flowing out of the neutral point O of the voltage dividing capacitors due to the three-phase load current is:

$$q_{T_{\mathrm{m}}} = \int_0^{T_{\mathrm{m}}} I_{\mathrm{a}} \mathrm{d}t + \int_0^{T_{\mathrm{m}}} I_{\mathrm{b}} \mathrm{d}t + \int_0^{T_{\mathrm{m}}} I_{\mathrm{c}} \mathrm{d}t \tag{5.3}$$

If $I_{\mathrm{b}} < 0$ and the charge flowing out of neutral point O $q_{T_m} < 0$, then U_{C_1} becomes smaller and U_{C_2} becomes larger; if $I_{\mathrm{b}} > 0$ and the charge flowing out of neutral point O $q_{T_m} > 0$, then U_{C_1} becomes larger and U_{C_2} becomes smaller. And since, as mentioned earlier, the current I_{b} is always negative throughout the sub-hexagon I, the influence exerted by the original MVV on the NPP balance is also in a fixed direction.

5.3.2. Multi-Vector Dwell Time Calculation

In the conventional multi-vector MPC method, dwell times for two adjacent voltage vectors and the zero vector are calculated from a geometric relationship. In this thesis, we refer to the method in [42], optimizing the switching time by the cost function. Assuming that the mapping reference voltage vector falls in the first small sector of sub-hexagon I, analyze the vector selection case and the dwell times. At this time, the original vectors closest to the reference voltage are V_3/V_4, V_{15} and V_{16}. First, based on the amplitude-second balance principle of the space vector, the following equation can be obtained:

$$\begin{cases} V_{\mathrm{e0}} T_0 + V_{\mathrm{e1}} T_1 + V_{\mathrm{e2}} T_2 = V_{ref} T_{\mathrm{s}} \\ T_0 + T_1 + T_2 = T_{\mathrm{s}} \end{cases} \tag{5.3}$$

where V_{e0} is the equivalent vector of the MVV V_{16} and T_1 is its dwell time. V_{e1} is the equivalent vector of the LVV V_{15} and T_2 is its dwell time. V_{e2} is the equivalent vector of the SVV V_3/V_4 and T_0 is its dwell time.

The reference voltage vector can be regarded as constant over a cycle. Therefore, transform (5.3) into the $\alpha\beta$ coordinate system:

$$\begin{cases} T_s V_\alpha = V_{\alpha 1} T_1 + V_{\alpha 2} T_2 + V_{\alpha 0} T_0 \\ T_s V_\beta = V_{\beta 1} T_1 + V_{\beta 2} T_2 + V_{\beta 0} T_0 \\ T_0 + T_1 + T_2 = T_s \end{cases} \tag{5.4}$$

where $V_{\alpha1}$, $V_{\alpha2}$ and $V_{\alpha0}$ are the α-axis component of the three selected voltage vectors. $V_{\beta1}$, $V_{\beta2}$ and $V_{\beta0}$ are the β-axis component. The duration ratio of the symmetrical vectors d_1, d_2 and d_0 can be obtained by normalizing dwell times T_1, T_2 and T_0, respectively.

$$\begin{cases} V_\alpha = V_{\alpha 1} d_1 + V_{\alpha 2} d_2 + V_{\alpha 0} d_0 \\ V_\beta = V_{\beta 1} d_1 + V_{\beta 2} d_2 + V_{\beta 0} d_0 \\ d_0 = T_0 / T_s \\ d_1 = T_1 / T_s \\ d_2 = T_2 / T_s . \end{cases} \tag{5.5}$$

In the previous chapter, the predictive voltage is adopted as the desired value u_d^* in the next sampling time. The cost function can be defined as follows to obtain the optimal solution of d_1, d_2 and d_0.

$$g = \left(u_\alpha^* - V_\alpha\right)^2 + \left(u_\beta^* - V_\beta\right)^2 . \tag{5.6}$$

where u_α^* and u_β^* are the predictive voltages. Taking partial derivatives of (5.6) yields

$$\begin{cases} \dfrac{\partial g}{\partial d_1} = \dfrac{\partial\left(\left(u_\alpha^* - V_\alpha\right)^2 + \left(u_\beta^* - V_\beta\right)^2\right)}{\partial d_1} = 0 \\ \dfrac{\partial g}{\partial d_2} = \dfrac{\partial\left(\left(u_\alpha^* - V_\alpha\right)^2 + \left(u_\beta^* - V_\beta\right)^2\right)}{\partial d_2} = 0. \end{cases} \tag{5.7}$$

Calculating (5.5) and (5.7) gives d_1 and d_2 as

$$\begin{cases} d_1 = (AC - BD)/\left(B^2 - A^2\right) \\ d_2 = (AD - BC)/\left(B^2 - A^2\right) \end{cases} \tag{5.8}$$

where

$$\begin{cases} A = V_{\alpha 1}^2 + V_{\beta 1}^2 \\ B = V_{\alpha 1} V_{\alpha 2} + V_{\beta 1} V_{\beta 2} \\ C = -u_\alpha^* V_{\alpha 1} - u_\beta^* V_{\beta 1} \\ D = -u_\alpha^* V_{\alpha 2} - u_\beta^* V_{\beta 2}. \end{cases} \tag{5.9}$$

The novel method is called optimal dwell time MPC. Its computational complexity is greatly reduced. On the basis of one-time prediction deadbeat control, the output error is further reduced, and the control accuracy is improved. After the center vector of the corresponding sub-hexagon is found out, the three resultant voltage vectors in the mapping sector are applied and switched in the optimal moments.

5.4. NPP Hysteresis Balance Based on Multipolarity of Space Vectors

5.4.1. NPP Hysteresis Balance Controller Design

Based on the previous analysis in Chapter 5.3, the NPP polarity of the final output voltage is dependent on the NPP polarities of the SVV and MVV selected in this control cycle. Therefore, the neutral point current can be effectively controlled by adjusting the combination of voltage vectors. According to this sampling period′s detected neutral point current polarity, the SVV and MVV opposite to the current polarity is output. The principle of hysteresis control is shown in Fig. 5. 5. However, the MVVs have no redundancy and can only balance the NPP from a fixed polarity, whereas the SVVs, despite being paired, where SVV(+) need to be avoided due to higher CMV.

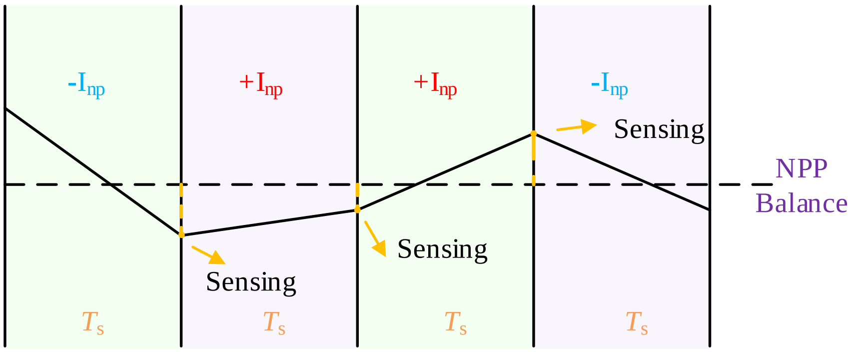

Fig. 5. 5. Scheme of NPP Balance hysteresis control.

In each sampling period, one equivalent short voltage vector and two voltage vectors on the boundary of small sectors are employed. This part will use this switch states recombination feature to achieve NPP hysteresis control. Defining the voltage vectors at the six sub-hexagons centers as $V_{si}^{'}$. According to the multi-vector MPC method proposed in this thesis, the output synthesized vector can only appear in the following three cases. Taking the sub-hexagon centered at V_3/V_4 as an example (as shown in Fig. 5. 2), the switch states selection principle is explained as follows.

5.4.2. Case Classification and Corresponding Selection

Case 1: the candidate voltage vectors are two SVVs and one ZVV in terms of magnitude. Because the SVV(+) is replaced by a combined vector of LVV and ZVV, given its larger CMV, NPP hysteresis control can be achieved just by selecting one proper SVV(-) and one $V_{si}^{'}$. If $U_{C_1} > U_{C_2}$, the SVV(-) with negative q_{T_m} are selected as the output. In sub-hexagon I, $I_a > 0$, $I_b < 0$, $I_c < 0$, thus V_3(POO) is the proper switch state. If $U_{C_1} < U_{C_2}$, the SVV(-) with positive q_{T_m} are selected as the output. Thus V_6(OON)/V_{14}(ONO) is the proper switch state. For the other two vectors, ZVV V_1(OOO) and the corresponding position of $V_{si}^{'}$ are chosen. None of them will cause NPP fluctuations, and the CMV is also very small.

Case 2: the candidate voltage vectors are two SVVs and one MVV in terms of magnitude. In sub-hexagon I, the two MVVs V_{16}(PON)/V_{26}(PNO) produce neutral currents I_b and I_c, which are all negative polarity. If $U_{C_1} > U_{C_2}$, the SVV(-) with negative q_{T_m} are selected as the output. Thus V_{16}(PON)/V_{26}(PNO) is the proper switch state. If $U_{C_1} < U_{C_2}$, the overall output need to be of positive q_{T_m} . This can be achieved by rationally utilizing the MVVs and SVVs. According to Fig. 5. 4, within the second small sector of the sub-hexagon I, the absolute value of I_c is always less than I_b. Therefore, the total polarity of V_6 and V_{16} is positive and still applies to the case where $U_{C_1} < U_{C_2}$. By the above method, although the neutral point current of MVV is not adjustable, reliable suppression of the NPP unbalance can still be ensured.

Case 3: the candidate voltage vectors are one SVV, one MVV and one LVV in terms of magnitude. In this case, the candidate space vectors have the same negative polarity neutral point current. When $U_{C_1} > U_{C_2}$, hysteresis control can be achieved by outputting them. But when $U_{C_1} < U_{C_2}$, even if the equivalent combinations of the SVV is $V_{si}^{'}$ with no neutral point current, the NPP polarity of the output vector is still negative and the hysteresis control fails. To cope with this situation, take the center vector replacement method. When $U_{C_1} < U_{C_2}$, replacing the center vector with a positive polarity neutral point current corrects the NPP of the resultant voltage vector to zero. Although the CMV amplitude of SVV(+) is larger, it is temporarily used to achieve NPP balance. When the reference voltage vector is located in other sub-hexagons, the switching state of the center vector that needs to be replaced also changes, but in principle, such measures can always have a negative feedback effect.

5.4.3. Vector Combinations in Different Cases

All voltage vectors and neutral current polarities in subhexagon I are labeled as shown in Fig. 5. 6, with black indicating 0, green indicating positive, and red indicating negative. The mechanisms of the above three cases are summarized in Table 5.3. $U_{C_1} < U_{C_2}$ in Case 3 needs to replace center vector, which has a certain impact on the current control performance. Apart from this, in other cases, it only changes the switch state and does not affect the position of the output voltage vector. This hysteresis control method provides a more robust suppression of NPP imbalance without the need to model the neutral point current. In addition, the regulation process is simple without the need to fine-tune the weighting factors or recalculate the action time of the active vector. By simulating the execution time of each process in the algorithm, it can be found that the computation time of the proposed strategy is only 19.6 μs, of which CMV suppression and NPP balancing account for only 24.4% of the computation amount.

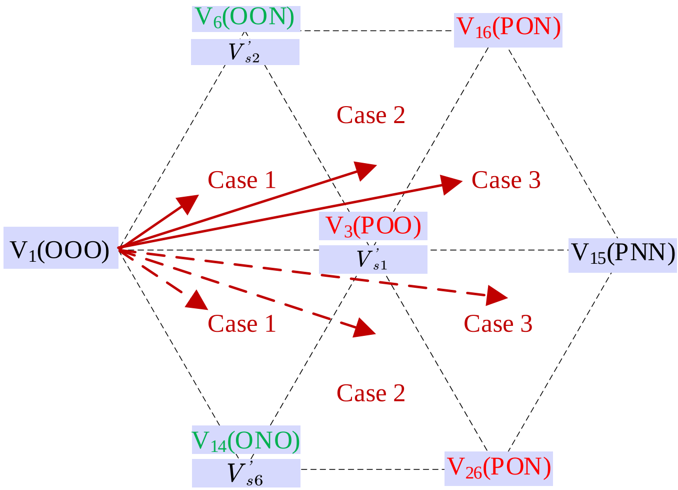

Fig. 5. 6. Scheme of vectors combination selection.

TABLE 5.3

SUMMARY OF NPP HYSTERESIS CONTROL

Nearest three-vector combination type	NPP polarity	Small sector number	Selected voltage vectors	Centre vector replace
Case 1	$U_{C_1} > U_{C_2}$	3	V_3, V_1, V'_{s2}	No need
		4	V_3, V_1, V'_{s6}	No need
	$U_{C_1} < U_{C_2}$	3	V'_{s1}, V_1, V_6	No need
		4	V'_{s1}, V_1, V_{14}	No need
Case 2	$U_{C_1} > U_{C_2}$	2	V_3, V'_{s2}, V_{16}	No need
		5	V_3, V'_{s6}, V_{26}	No need
	$U_{C_1} < U_{C_2}$	2	V_3, V'_{s2}, V_{16}	No need
		5	V_3, V'_{s6}, V_{26}	No need
Case 3	$U_{C_1} > U_{C_2}$	1	V_3, V_{15}, V_{16}	No need
		6	V_3, V_{15}, V_{26}	No need
	$U_{C_1} < U_{C_2}$	1	V_4, V_{15}, V_{16}	Need
		6	V_4, V_{15}, V_{26}	Need

5.5. Overall Control Scheme

Fig. 5. 7 illustrates the flowchart for the proposed method, which begins with the calculation of *dq*-axis predictive voltages of PMSM. Then they are transformed to αβ-axis, and the sub-hexagon can be located. The mapping αβ-axis predictive voltages are used to obtain two adjacent voltage vectors and center voltage vectors. The optimal dwell times of multi-vector are calculated using the cost function. The computational burden is greatly reduced, and the reference voltage is generated more accurately.

In order to achieve CMV suppression and NPP balance, a hysteresis controller is designed. After the selection of the candidate voltage vectors is completed and the dwell time is determined, according to the detected polarity of the neutral point current in this sampling cycle, the vectors combination is adjusted. Finally, the 3L-NPC inverter outputs NPP opposite to the polarity of the neutral point current. Compared to the existing strategies, the proposed strategy is easily implemented and gets rid of the dependence on the motor model.

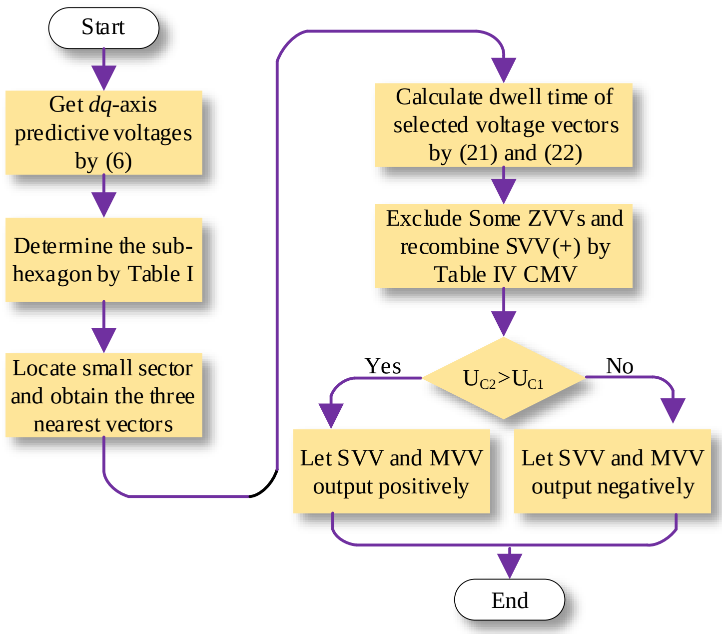

Fig. 5. 7. Flowchart of the proposed scheme.

5.6. Experimental Results

5.6.1. PMSM Test Rig Setup Based on Three-level Inverter

To validate the feasibility of the proposed low computational burden MPC with NPP balance and CMV suppression, the hardware experimental results are obtained on a PMSM platform. The photograph of the experimental test rig is shown in Fig. 5. 8. The oscilloscope is the high performance Tektronix MDO4024HD. Under different working conditions of the experiment, the switching frequency is in the range of 4-8khz, which is suitable for practical application scenarios of high voltage and high power. A high-power DC supply powers the three-level NPC inverter, and an independent small power supply powers the encoder of the PMSM. The loading is provided with the help of a magnetic powder brake and an external tension controller. The MicroLabBox dSPACE 1202 is chosen as the main controller. The parameters are the same as the PMSM taken for the experiments in Chapter 3.

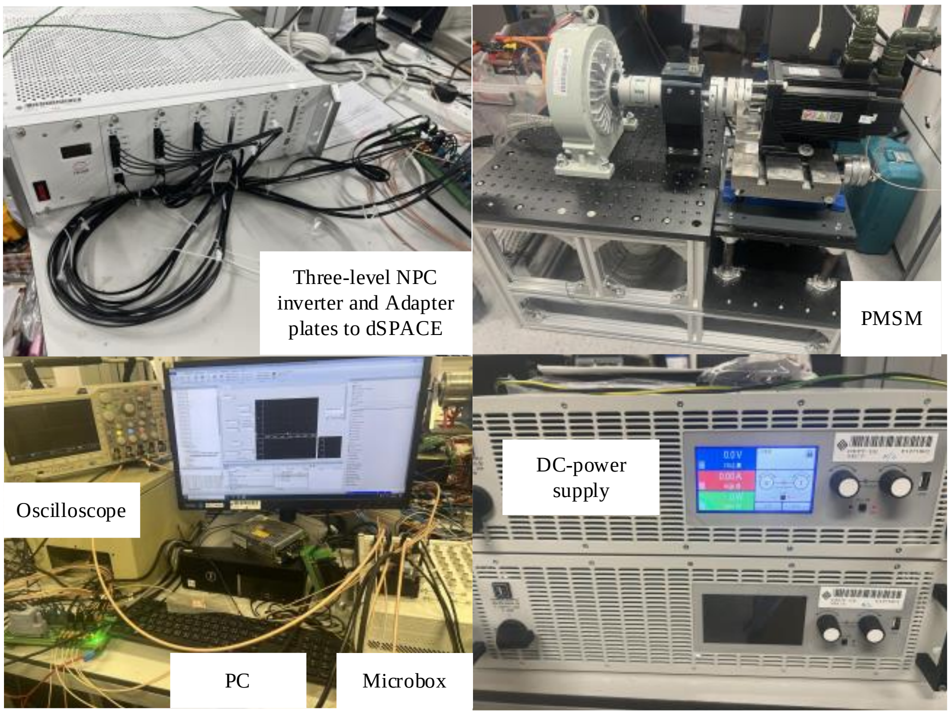

Fig. 5. 8. PMSM test rig setup.

5.6.2. Steady-State Performance and Dynamic Response Comparison

The performance of the proposed schemes is evaluated by conducting comprehensive comparisons with RFS-MPC and conventional multi-vector MPC (CMV-MPC) proposed in [102]. First, the steady-state performance of the three approaches is tested under 500 r/min (50% rated speed) with a load of 3 N·m. The line-line voltage and the phase currents corresponding to different methods are shown in Fig. 5. 9, respectively. The comparative experiment was also carried out under the operation mode of rated speed and load, and the results are shown in Fig. 5. 10. From the current spectrum, it can be observed that the proposed method has the lowest current distortion among the three approaches under different operating modes as it further optimizes the dwell times.

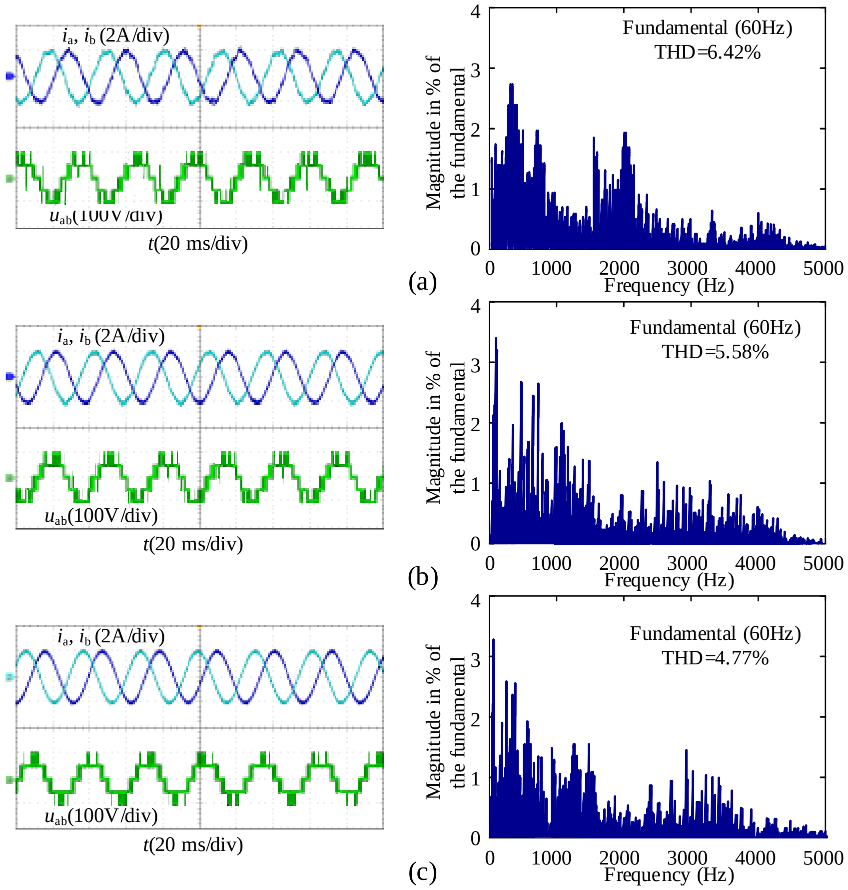

Fig. 5. 9. Steady-state performance comparison at 500 r/min and 3Nm load. (a) RFS-MPC. (b) CMV-MPC. (c) Proposed method.

The THD of RFS-MPC is significantly greater than that of CMV-MPC and the proposed method. This is because RFSMPC selects the output voltage vector according to the region where the calculated reference voltage is located and maintains a single output throughout the control cycle. As shown in Fig. 5. 11, the average switching frequency of RFS-MPC will always be lower than that of the other two methods if operated at the same sampling frequency. This is true over the entire speed range, especially when the motor is running at low speeds, where zero vector is selected most of the time.

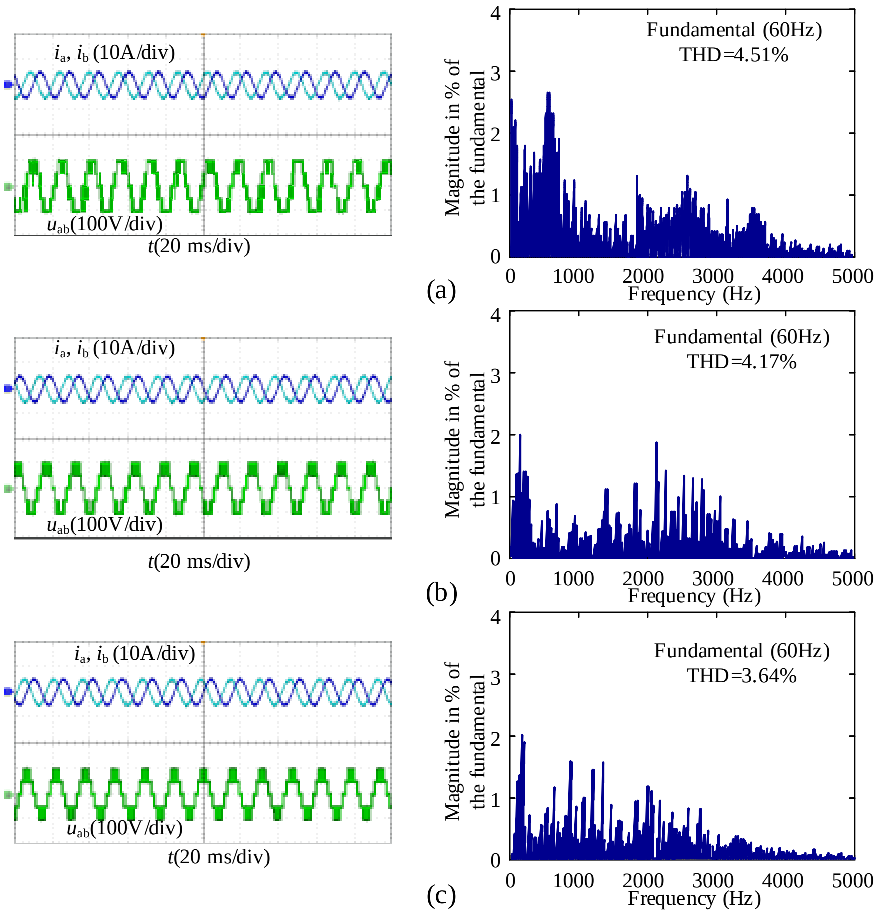

Fig. 5. 10. Steady-state performance comparison at rated speed and load. (a) RFS-MPC. (b) CMV-MPC. (c) Proposed method.

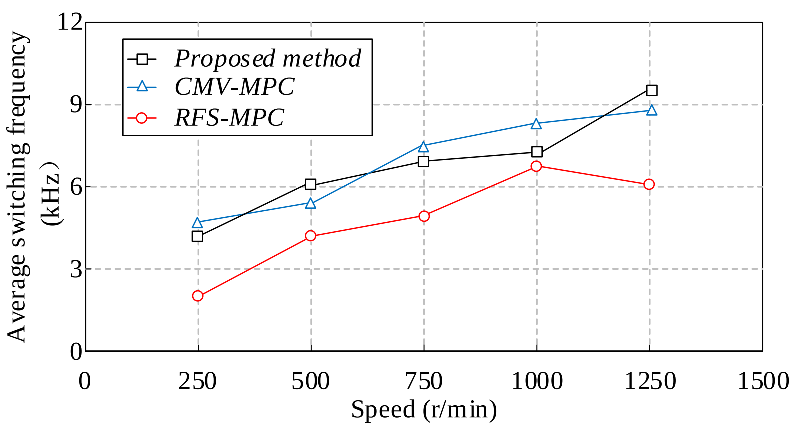

Fig. 5. 11. Average switching frequencies comparison under different speeds.

The power test verifies that the inverter loss of the proposed scheme is lower than that of CMV-MPC under different operating conditions. Despite the NPP balance, CMV suppression, and excellent control effect, it does not actuate the switching device more frequently. The switching devices of the 3L-NPC inverter system are 1.5 times that of the two-level system. Thus, the switching loss is more significant. It makes excellent sense to reduce the switching frequency as much as possible, like the proposed method.

It is also essential to analyze the transient behavior of the PMSM drive and ascertain the dynamic response capability of the proposed approach with the rated load. Fig. 5. 12(a) shows the q-axis current and speed response to a sudden change in reference speed from 400 r/min to 750 r/min. It can be seen that the proposed strategy can make a quick response to complete the acceleration process. Moreover, Fig. 5. 12(b) shows the drive response when the motor starts to rate speed. Fig. 5. 13 shows the transient performance comparison of different methods when the q-axis reference current is set to 4A. The settling time of CMV-MPC is the longest, while the proposed method took 1.14 ms to track the reference current, slightly slower than RFS-MPC. These results demonstrate that the proposed method has satisfactory dynamic performance. During the full speed range, the major contribution of the proposed method is to relieve the computational burden at a similar switching frequency range, besides certain improvements in motor performance.

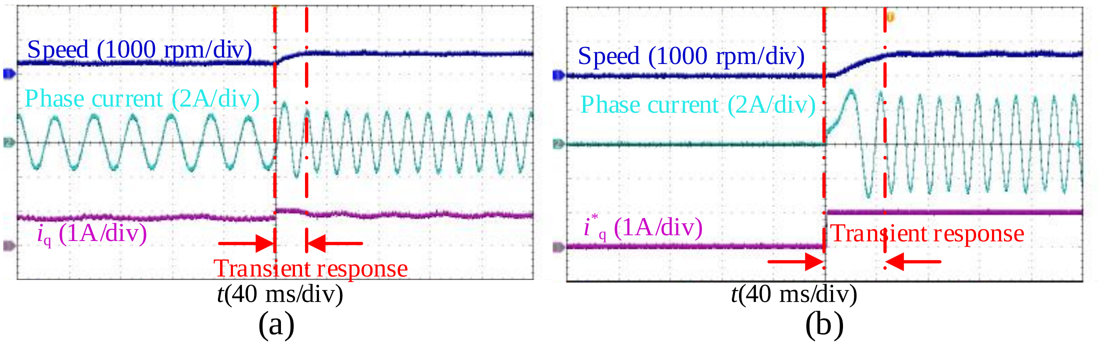

Fig. 5. 12. Dynamic response of the proposed method. (a) Speed change from 400 r/min to 750 r/min. (b) Motor starts to rated speed.

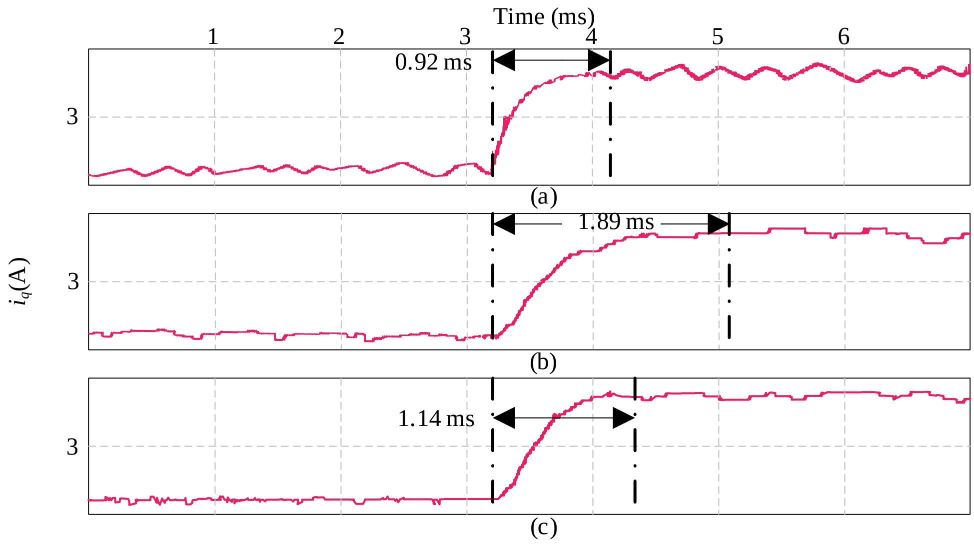

Fig. 5. 13. Comparison of transient performance when the speed loop is removed, and the q-axis reference current is given as 4A. (a) RFS-MPC. (b) CMV-MPC. (c) Proposed method.

5.6.3. NPP Balance and CMV Suppression Test

Two tests were conducted to verify the NPP balancing effect of the proposed method. First, the capacitors voltages before and after the proposed scheme is put into use are compared, and the experimental results are shown in Fig. 5. 14(a). It can be observed that the imbalance is serious at the beginning, and the voltage difference between the upper capacitor and the lower capacitor $U_{C_1} - U_{C_2}$ on the DC side is about 15V. After the proposed method is put into use, two capacitor voltages tend to be same and their fluctuations are restricted within the range of [-5, 5] most of the time. The proposed method achieves significant results for the control of NPP. The dynamic response of the NPP balance effect is shown in Fig. 5. 14(b) when the motor speed is changed from 500 r/min to 1000 r/min, and the capacitors voltage difference remains stable. The comparison experiment with CMV-MPC is presented in Fig. 5. 15, which indicates that the proposed method has a better NPP balancing capability in the full speed range.

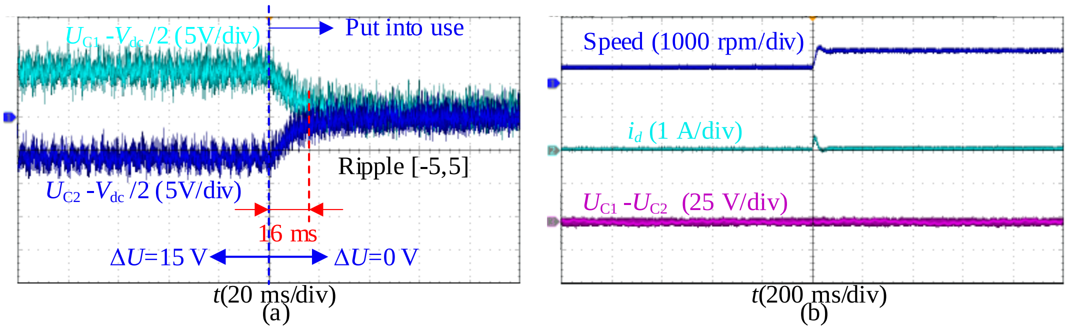

Fig. 5. 14. Two tests of NPP balance. (a) Comparison before and after application of the proposed method. (b) NPP suppression effect dynamic response.

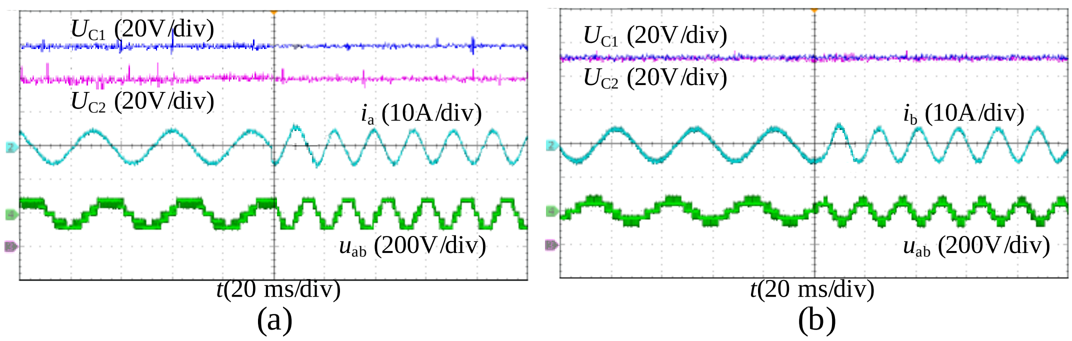

Fig. 5. 15. Response of speed change from 500 to 1000 r/min with rated load for (a) CMV-MPC. and (b) proposed method.

On the other hand, the CMV suppression effect of the proposed method is shown in Fig. 5. 16. Due to the application of V_0(NNN), V_2(PPP), and SVVs(+), the amplitude of CMV is up to $\pm U_{dc}/2$ before the proposed algorithm is put into use. It should be noted that the magnitude of CMV is reduced to less than 50 V immediately when the proposed strategy is applied. The dynamic effectiveness of CMV suppression is proved while, at the same time, the capacitors voltages can be properly balanced to $U_{dc}/2$. Fig. 5. 17 shows the experimental waveforms at high modulation indices. The THD of CMVMPC is 5.39%, while the proposed scheme has higher current quality, but its CMV suppression effect is somewhat reduced, because Case 3 requires the use of SVV(+).

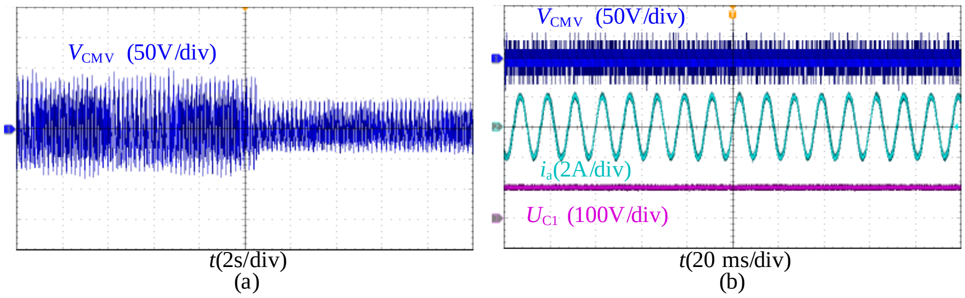

Fig. 5. 16. CMV suppression effect. (a) Dynamic waveforms of CMV. (b) Integrated situation under stable operation.

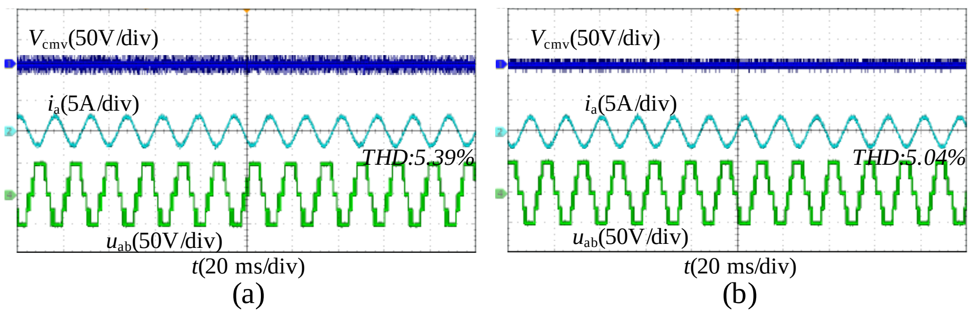

Fig. 5. 17. Experimental waveforms of the different methods at a modulation index of 1. (a) CMV-MPC. (b) the proposed method.

5.6.4. Robustness Against Parameters Mismatch Test

The hysteresis control adopted by the proposed method is independent of the capacitor model parameters. A comparative experimental study is carried out to verify the effectiveness of the proposed method in balancing NPP when the capacitor parameters are inaccurate. Fig. 5. 18 illustrates that the effect of balancing U_{C_1} and U_{C_2} of the proposed method is not influenced by the capacitor parameter mismatch. In terms of motor parameters, it mainly involves resistance, inductance and flux linkage, and their maximum range of variation is also determined experimentally. Fig. 5. 19 shows the comparative results of RFS-MPC, CMV-MPC, and the proposed method for stator resistance mismatch.

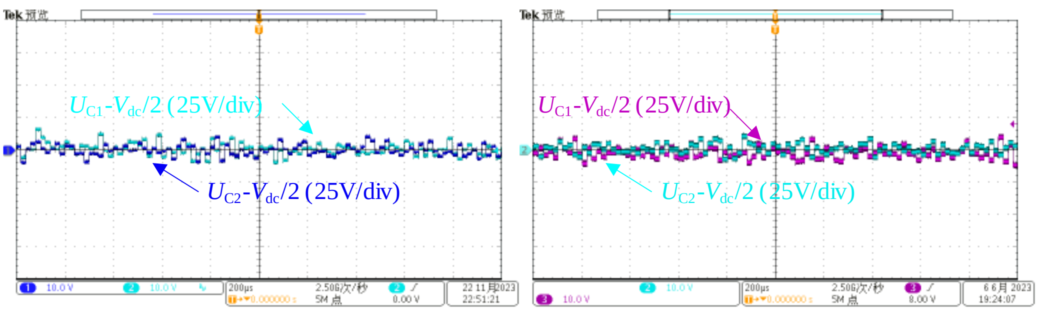

Fig. 5. 18. NPP unbalance suppression effect of the proposed algorithm. (a) Accurate capacitance parameters. (b) Capacitor increased to 150% of actual value.

The motor operates at 800 rpm with rated load, and at 0.10 s, the model resistance suddenly changes to 150% of the actual value. The phase current fluctuation and the q-axis ripple based on the proposed method are the lowest. The steady state current performance with mismatched inductance and flux parameters is shown in Fig. 5. 20. Despite the slight increase in THD, the waveforms are stable and sinusoidal. The proposed method has some sensitivity to the motor parameters, especially the inductance, but still operates stably at 0.5 times mismatch.

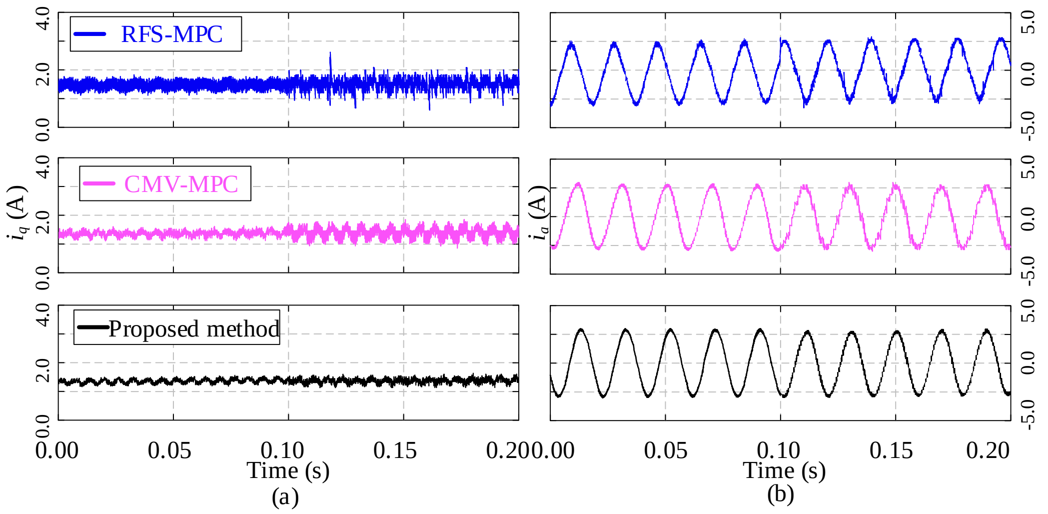

Fig. 5. 19. Robustness against resistance parameter mismatch comparison of three methods. (a) q-axis currents. (b) A-phase stator current.

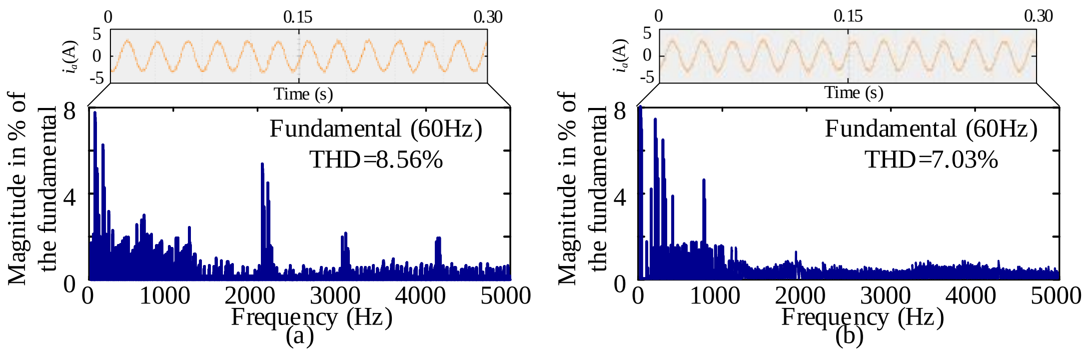

Fig. 5. 20. Steady-state stator current curves and their FFT spectra with parameter mismatch. (a) Proposed method when inductance decreases by 50%. (b) Proposed method when flux-linkage increases by 50%.

5.6.5. Algorithm Execution Time Test

To verify the computational efficiency of the proposed methods, the turnaround time was read directly in the dSPACE1202 control system. Fig. 5. 21 shows the algorithm execution time for different scenarios under the same control period of 50μs. For a fair comparison, Scenario 1 employs the optimized dwell time proposed in this chapter, but the nearest three-vector solution is used as the benchmark, and Scenario 2 uses the proposed scheme. It can be observed that the computation time for Scenario 1 is longer at 35.6μs. This is due to the fact that the unsimplified multi-vector algorithm needs to compute the predicted currents for the 27 switching states of the three-level inverter and traverse to find the optimal output combination. Scenario 2 is 55% faster than Scenario 1. In addition, the complete operation of the proposed scheme is tested, and 9.3μs of code execution time is required to detect the neutral current polarity and the data retention time for the hysteresis control process. The proposed method is better in terms of overall performance and is more computationally efficient. Relieving the computational burden is meaningful for practical applications, incorporate protection functions and communication. The proposed method can leave more time margin for other steps required for code implementation.

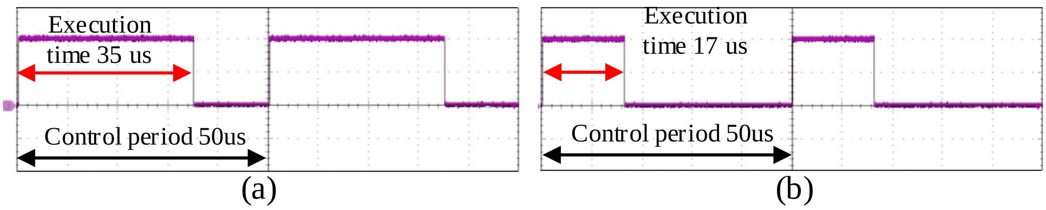

Fig. 5. 21. Algorithm execution time comparison. (a) Scenario 1. (b) Scenario 2.

5.7. Conclusion

In this chapter, a novel multi-vector MPC method for 3L-NPC inverter-powered PMSM is proposed, aiming to improve computational efficiency and synergistically suppress CMV and balance NPP. In the proposed method, the optimal dwell time of each adjacent vector is calculated by the cost function without weight factors. To realize the independence of capacitor parameters and NPP balance, a hysteresis controller is introduced. The positive and negative NPP polarities of various vectors in different sub-hexagons are fully utilized to decouple vector selection from CMV suppression/NPP balance. Comparative experiments are conducted with other three-level MPC algorithms, which reveal that the proposed method has not only satisfactory steady-state output performance but also fast transient response. The effectiveness and robustness of the proposed method is also verified. The CMV is restricted within $\pm U_{dc}/6$ most of the time, and the NPP imbalance situation has also been greatly improved. Future work will focus on the multiple sampling mechanism of the three-level MPC, MPC optimization considering three-level inverter nonlinearity, and enhanced robust MPC under parameter mismatch.

CHAPTER 6. COHERENT VECTOR BASED MODEL PREDICTIVE CONTROL WITH ZERO-SEQUENCE COMPONENT INJECTION FOR THREE-LEVEL NPC INVERTER FED PMSM DRIVES

6.1. Introduction

Conventional MPC selects one basic voltage vector through the enumeration process, exhibiting relatively high output ripples. To enhance the control performance, a three-level neutral-point-clamped (NPC) inverter is applied, although this increases the complexity of the control algorithm for PMSM. In the proposed MPC scheme, a set of coherent voltage vectors (CVVs) with movable starting points is introduced to replace the basic candidates. The pulse train of the optimal CVV is generated by single-carrier modulation, and capacitor charge balancing in different sectors can be included in the zero-sequence component injection. The proposed CVV-MPC is characterized by simple implementation and satisfactory performance under low switching frequency. Comparative experiments are conducted to verify the effectiveness and superiority of the proposed method.

6.2. Voltage Vector Coherence

In the FS-MPC presented in the previous chapter, the best voltage vector is selected among the 27 available vectors and applied during the entire control period. This will cause the output voltage to change abruptly and is also computationally inefficient. To address these issues, we introduce the concept of coherent voltage vector, which relates the voltage vectors of the current time step to the previous step. The candidate set is modified as follows:

$$u_{dqn}^{c}(k) = \varepsilon_{\alpha} u_{dq}^{c}(k-1) + (1-\varepsilon_{\alpha}) u_{dqn} \tag{6.1}$$

where $u_{dqn}^{c}(k)$ denotes the candidate vector after coherent, u_{dqn} denote the different original voltage vectors, ε_{α} denotes the degree of coherence and takes values in the interval [0, 1), the larger ε_{α} is, the more pronounced the coherence of the voltage is.

In order to avoid repeated calculation of redundant vectors and reduce the number of calls to the formula, the original voltage vector shown in Fig. 4. 2 is simplified. Such u_{dqn} intervals of 60◦ also make full use of the rich vector resources of the three-level inverter. Fig. 6. 1 shows the candidate vector selection for several control cycles, which have been coherentized. Therefore, the cost function considering the delay compensation is constructed as:

$$J(k) = \left| i_{ds}^{*} - i_{ds}(k+2) \right| + \left| i_{qs}^{*} - i_{qs}(k+2) \right| \tag{6.2}$$

From analysis (6.1), we can know that if ε_{α} is too large, it will reduce the output capability and affect the tracking of the reference value. When ε_{α} is zero, it is exactly the same as before the coherentization process. Therefore, it is necessary to set an upper limit for ε_{α} to ensure that the dynamic response can be at the same level as conventional control methods. Fig. 6. 1 illustrates the scenario when ε_{α}=0.5, a value chosen to ensure that the cut-off frequency is approximately equal to the bandwidth of the conventional MPC, while also maintaining the coherence of the CVVs.

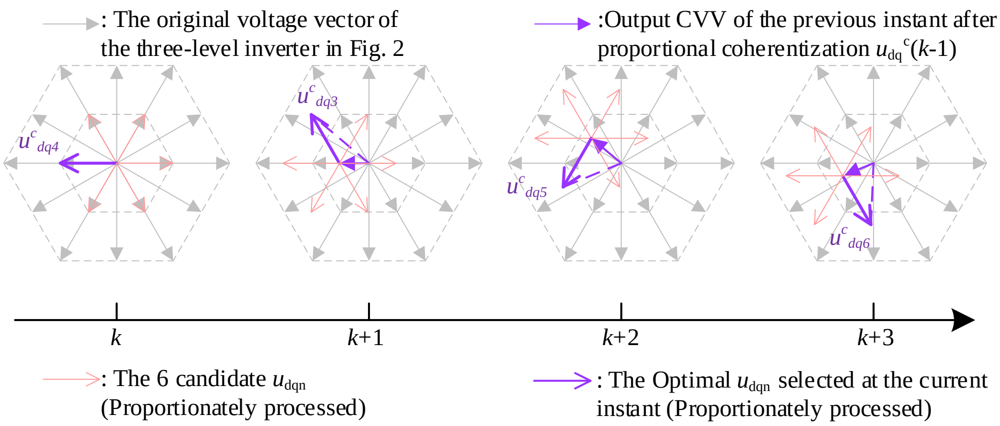

Fig. 6. 1. Optimal CVV selection process in several control cycles.

6.3. Optimal CVV Synthesis with Neutral-Point Capacitor Voltage Balance

Among the u_{dqn}^{c} pointing in different directions, the one with the smallest cost function is selected as the optimal CVV. After that, its corresponding active vectors group and duration time need to be determined in the conventional methods.

In this chapter, a novel vector space decomposition adapted to the concept of vector coherence is employed to reduce computational complexity without the need for multiple optimizations. Therefore, we must first know the precise sector of u_{dq}^{c} according to the geometric relationship. The desired CVV in the stationary $\alpha-\beta$ reference frame is obtained through inverse Park transformation:

$$\begin{bmatrix} u_{\alpha}^{c} \\ u_{\beta}^{c} \end{bmatrix} = \begin{bmatrix} \cos\theta & -\sin\theta \\ \sin\theta & \cos\theta \end{bmatrix} \begin{bmatrix} u_{d}^{c} \\ u_{q}^{c} \end{bmatrix}. \tag{6.3}$$

Transform it to the per unit format, taking V_{dc} as benchmark and represent it as the three-phase symmetric form:

$$\begin{cases} u_a^* = m \cdot \sin\theta \\ u_b^* = m \cdot \sin\left(\theta - \dfrac{2\pi}{3}\right) \\ u_c^* = m \cdot \sin\left(\theta + \dfrac{2\pi}{3}\right) \end{cases} \tag{6.4}$$

where m = $\sqrt{3} \cdot V^c / V_{dc}$, $\theta = \omega t$ (ω is the angular frequency).

In existing studies, the three-level vector space is often divided into six sub-hexagons [120], [121], which are simplified to two-level algorithms to narrow the range of optimization search and reduce switching losses. However, adjacent subhexagons have overlapping areas. As shown in Fig. 6. 2(a), this chapter designs a more reasonable sector division method by combining the properties of the sub-hexagon rule. The sector position can be determined directly based on the number of candidate vectors that minimizes the cost function. As shown in Fig. 6. 2(b), each u_n^c can also be regarded as synthesized from the center vector of each quadrilateral sector as the starting point. This eliminates the need to call the inverse trigonometric function and the cumbersome sector judgment and sub-sector judgment processes. The relationship between u_n^c and sector number *N* is shown in Table 6.1.

TABLE 6.1

CVV SECTOR JUDGMENT

Sector number (N)	Corresponding CVV	S_a	S_b	S_c
I	u_1^c	≥ 0	≤ 0	≤ 0
II	u_2^c	≥ 0	≥ 0	≤ 0

III	u_3^c	≤ 0	≥ 0	≤ 0
IV	u_4^c	≤ 0	≥ 0	≥ 0
V	u_5^c	≤ 0	≤ 0	≥ 0
VI	u_6^c	≥ 0	≤ 0	≥ 0

In this chapter, an efficient zero-sequence component injection scheme is implemented, which makes full use of the sign law of S_x in Table 6.1. Unlike the traditional method, the scheme eliminates the need to iteratively determine the positive and negative phase voltages after superimposing the zero-sequence components (u_{zs}), thereby facilitating the conservation of computational resources. The corrected modulation wave h_x^* of each phase is:

$$h_x^* = \frac{2}{\sqrt{3}} u_x^* + u_{zs} \tag{6.5}$$

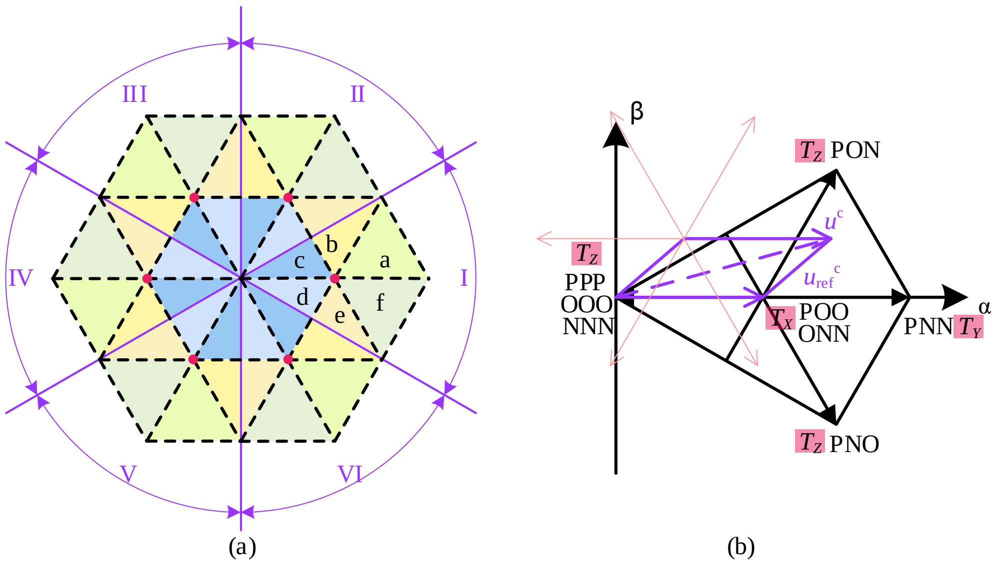

Fig. 6. 2. Quadrilateral sectors and CVV synthesis. (a) Division of I-VI sectors. (b) CVV synthesis path in sector I and corresponding vectors.

Since each sector corresponds to a specific combination of switching function signs, the required CVV can be achieved only by changing the duty cycle of single carrier. Fig. 6. 3 shows the adopted single carrier modulation mode, which greatly reduces the amount of computation and simplifies the modulation process while providing strong neutral-point voltage balancing. By comparing the green modulated wave with the purple carrier wave, switching signals that contains two states $S_x \in \{1, 0\}$ or $S_x \in \{0, -1\}$ are produced.

According to chapter 4, only when the output state of a phase is O, the load current of that phase flows through the neutral point and has an effect on the neutral-point potential. The relationship between the average neutral-point current and the load current as well as the three-phase switching state in one control cycle is as follows:

$$\bar{i}_{\mathrm{NP}} = d_{\mathrm{Oa}} i_{\mathrm{a}} + d_{\mathrm{Ob}} i_{\mathrm{b}} + d_{\mathrm{Oc}} i_{\mathrm{c}} \tag{6.6}$$

where d_{Ox} denotes the O-state duty cycle of phase x, which is calculated with respect to the positive or negative of S_x:

$$d_{\mathrm{Ox}} = 1 - \left| d_{\mathrm{NPx}} \right| = \begin{cases} \left(1 - h_{\mathrm{x}}^{*}\right)/2, & S_{\mathrm{x}} > 0 \\ \left(1 + h_{\mathrm{x}}^{*}\right)/2, & S_{\mathrm{x}} \le 0 \end{cases} \tag{6.7}$$

Taking CVV located in sector I as an example, substituting (6.5) and (6.7) into (6.6):

$$
\begin{aligned}
\bar{i}_{\mathrm{NP}} &= \frac{1-h_{\mathrm{a}}^*}{2} i_{\mathrm{a}} + \frac{1+h_{\mathrm{b}}^*}{2} i_{\mathrm{b}} + \frac{1+h_{\mathrm{c}}^*}{2} i_{\mathrm{c}} \\
&= \frac{1}{2}\left[h_{\mathrm{a}}^* \left(i_{\mathrm{b}} + i_{\mathrm{c}} \right) + h_{\mathrm{b}}^* i_{\mathrm{b}} + h_{\mathrm{c}}^* i_{\mathrm{c}} \right] = \frac{1}{2}\left[\left(h_{\mathrm{a}}^* + h_{\mathrm{b}}^* \right) i_{\mathrm{b}} + \left(h_{\mathrm{a}}^* + h_{\mathrm{c}}^* \right) i_{\mathrm{c}} \right] \\
&= \frac{1}{2}\left[\left(\frac{2u_{\mathrm{a}}^*}{\sqrt{3}} + \frac{2u_{\mathrm{b}}^*}{\sqrt{3}} + 2u_{\mathrm{zs}} \right) i_{\mathrm{b}} + \left(\frac{2u_{\mathrm{a}}^*}{\sqrt{3}} + \frac{2u_{\mathrm{c}}^*}{\sqrt{3}} + 2u_{\mathrm{zs}} \right) i_{\mathrm{c}} \right] \\
&= \frac{1}{2}\left[\left(-\frac{2u_{\mathrm{c}}^*}{\sqrt{3}} + 2u_{\mathrm{zs}} \right) i_{\mathrm{b}} + \left(-\frac{2u_{\mathrm{b}}^*}{\sqrt{3}} + 2u_{\mathrm{zs}} \right) i_{\mathrm{c}} \right] \\
&= -\left[u_{\mathrm{zs}} i_{\mathrm{a}} + \frac{1}{\sqrt{3}} \left(u_{\mathrm{b}}^* i_{\mathrm{c}} + u_{\mathrm{c}}^* i_{\mathrm{b}} \right) \right]
\end{aligned} \tag{6.8}
$$

To achieve active control of the neutral-point potential balance, the DC bus capacitor voltage variation is detected, and feedback correction is formed. The relationship between the voltage deviation U_{npv} and the neutral-point current within a control cycle is:

$$U_{\mathrm{npv}} = U_{\mathrm{C_1}} - U_{\mathrm{C_2}} = \bar{i}_{\mathrm{NP}}' T_{\mathrm{s}} / C \tag{6.9}$$

where $\bar{i}_{\mathrm{NP}}'$ is the average increment of the neutral-point current caused by the charging and discharging of the capacitors, which requires adjusting the zero-sequence voltage injection amount.

$$\bar{i}_{\mathrm{NP}} + \bar{i}_{\mathrm{NP}}' = 0 \tag{6.10}$$

$$u_{\mathrm{zs}} = \frac{1}{i_{\mathrm{a}}} \left[\frac{CU_{\mathrm{npv}}}{T_{\mathrm{s}}} - \frac{1}{\sqrt{3}} \left(u_{\mathrm{b}}^* i_{\mathrm{c}} + u_{\mathrm{c}}^* i_{\mathrm{b}} \right) \right] \tag{6.11}$$

In the same way, the expressions of the zero-sequence components in the six sectors can be found in Table 6.2.

An exact mathematical relationship between the neutral point average current and the zero-sequence component is established in each small quadrilateral sector of the simplified three-level vector space. It can be seen that only the original CVV, the output current, and the upper and lower capacitor voltages are needed to generate the zero-sequence components required to balance the neutral-point potential, and the expression is simple and does not contain complex trigonometric calculations. Its computational complexity is significantly reduced as well. After simulation verification, the computation time for its prediction optimization is only about 15% of that required by the strategy in [103].

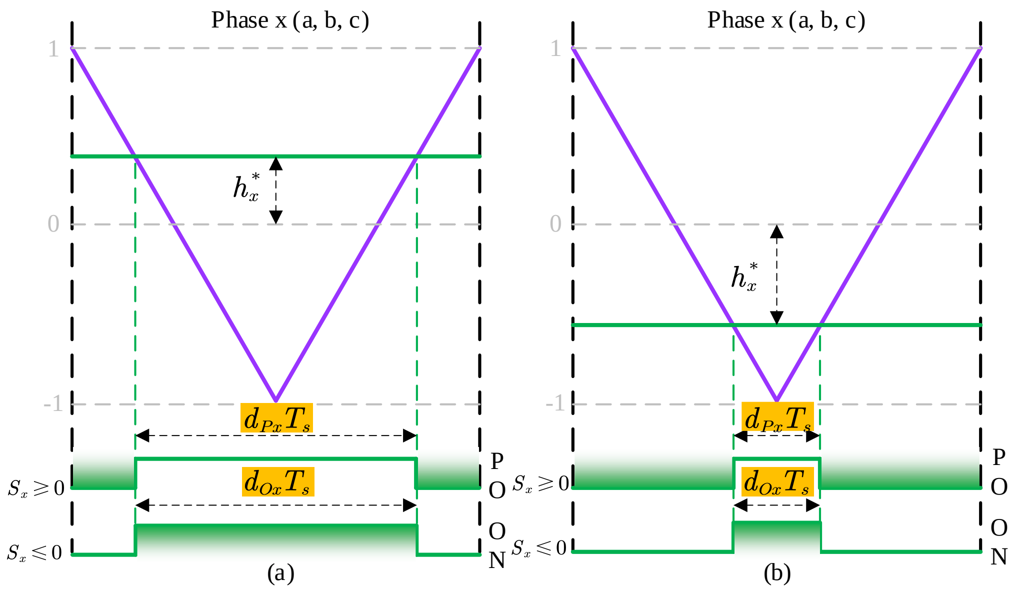

Fig. 6. 3. Single carrier modulation mode. (a) Generation of duty cycle when h_x^* is positive. (b) Generation of duty cycle when h_x^* is negative.

TABLE 6.2

NEUTRAL-POINT CURRENTS AND ZERO SEQUENCE VOLTAGES IN SIX SECTORS

Sector	$\bar{i}_{np}$	u_{zs}
I	$-\left[u_{zs}i_a+\frac{1}{\sqrt{3}}(u_b^*i_c+u_c^*i_b)\right]$	$\frac{1}{i_a}\left[\frac{CU_{npv}}{T_s}-\frac{1}{\sqrt{3}}(u_b^*i_c+u_c^*i_b)\right]$
II	$u_{zs}i_c+\frac{1}{\sqrt{3}}(u_a^*i_b+u_b^*i_a)$	$\frac{1}{i_a}\left[\frac{CU_{npv}}{T_s}-\frac{1}{\sqrt{3}}(u_b^*i_c+u_c^*i_b)\right]$
III	$-\left[u_{zs}i_b+\frac{1}{\sqrt{3}}(u_a^*i_c+u_c^*i_a)\right]$	$\frac{1}{i_a}\left[\frac{CU_{npv}}{T_s}-\frac{1}{\sqrt{3}}(u_b^*i_c+u_c^*i_b)\right]$
IV	$u_{zs}i_a+\frac{1}{\sqrt{3}}(u_b^*i_c+u_c^*i_b)$	$\frac{1}{i_a}\left[\frac{CU_{npv}}{T_s}-\frac{1}{\sqrt{3}}(u_b^*i_c+u_c^*i_b)\right]$
V	$-\left[u_{zs}i_c+\frac{1}{\sqrt{3}}(u_a^*i_b+u_b^*i_a)\right]$	$\frac{1}{i_a}\left[\frac{CU_{npv}}{T_s}-\frac{1}{\sqrt{3}}(u_b^*i_c+u_c^*i_b)\right]$
VI	$u_{zs}i_b+\frac{1}{\sqrt{3}}(u_a^*i_c+u_c^*i_a)$	$\frac{1}{i_a}\left[\frac{CU_{npv}}{T_s}-\frac{1}{\sqrt{3}}(u_b^*i_c+u_c^*i_b)\right]$

6.4. Pulse Train Generation

Once we have found the optimal CVV through the cost function and synthesize it with single carrier zero-sequence injection method, we next need to generate switching signals based on it [122]. To prevent duty cycle saturation, resulting in output voltage distortion, the zero-sequence component must be reasonably limited.

$$\begin{cases} u_{\text{zsmax}}=1-\dfrac{2}{\sqrt{3}}\max\left(u_a^*,u_b^*,u_c^*\right) \\ u_{\text{zsmin}}=-1-\dfrac{2}{\sqrt{3}}\min\left(u_a^*,u_b^*,u_c^*\right) \end{cases} \tag{6.12}$$

When the injected zero-sequence component goes up to $u_{zs\max}$ or down to $u_{zs\min}$, the duty cycle of one phase will becomes 1, and the switch does not operate during this cycle. Under these conditions, in order to maintain the regulating capability of the neutral-point balance, a dual-carrier modulation is taken to generate the desired switching signals. As shown in Fig. 6. 4, the charge is balanced in one control cycle under the effect of the compensation amount, and it can be derived as:

$$u_{\text{off}}^{*}=\frac{C\left(U_{C_1}-U_{C_2}\right)+\sum\limits_{\text{x=a,b,c}} d_{\text{Ox}} i_{\text{x}}}{\sum\limits_{\text{x=a,b,c}} \operatorname{sign}\left(h_{\text{x}}^{*}\right) i_{\text{x}}} \tag{6.13}$$

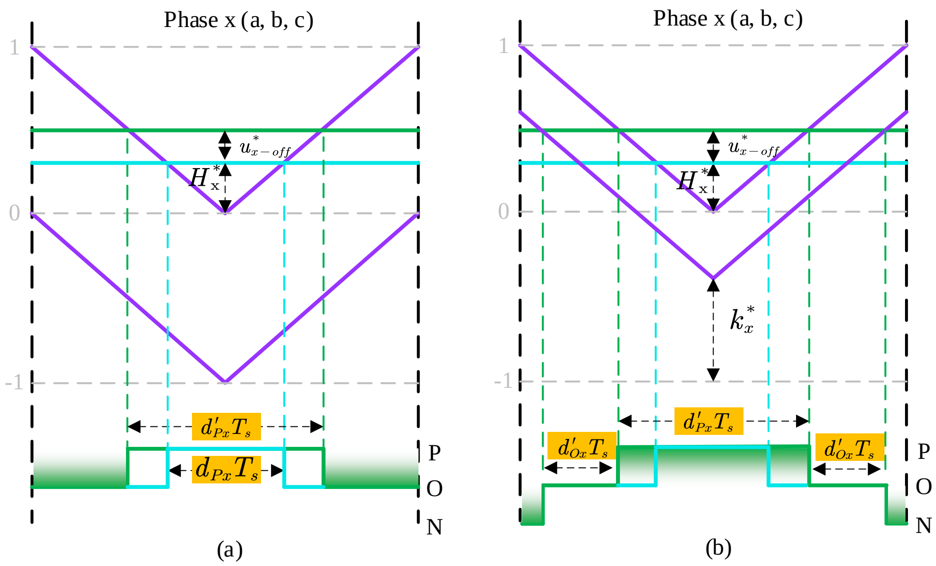

Fig. 6. 4. Dual-carrier modulation mode under initial and improved modulated waves.

(a) Two carriers are fixed. (b) Lower carrier is adjustable.

6.5. Control Block Diagram and Implementation Steps

Based on the above analysis, the proposed control strategy is implemented in three progressive stages shown in Fig. 6. 5. In summary, the proposed strategy can be implemented in the following steps:

Step 1 Measurement: Sample the motor speed and rotor position, as well as the stator currents $\boldsymbol{i}_s$. Record the voltage vector applied at the current moment.

Step 2 Desired value calculation: Develope the discrete mathematical model of PMSM. Like the conventional FS-MPC method, use the external speed loop to obtain the current reference i^*_q and set i^*_d to 0.

Step 3 CVV selection: The original voltage is coherently transformed into u^c_{dqn} using (6.1) along with the output state from the previous moment. The current states of all candidate CVVs at the ($k+2$)th instant are predicted using the discrete models in (2.25) and (2.26). The cost function in (6.2) is then evaluated, and the u^c_{dqn} corresponding to the minimum current error is selected.

Step 4 Zero-sequence component injection: Calculate the average neutral-point current $\bar{i}_{np}$ using the voltage deviation U_{npv} on the DC bus. Based on the quadrilateral sector number of the optimal CVV, determine the corresponding zero sequence component u_{zs} from Table 6.2 to balance the neutral point potential. The modified modulated wave amplitude h^*_x is then obtained from (6.5).

Step 5 Switching pulses generation: Before the final reference voltage h^*_x is output, it is judged according to (6.12). Based on the switching function signs in Table 6.2, h^*_x is converted to a two-channel signals, which is then simply compared with the triangular carrier to produce four drive signals.

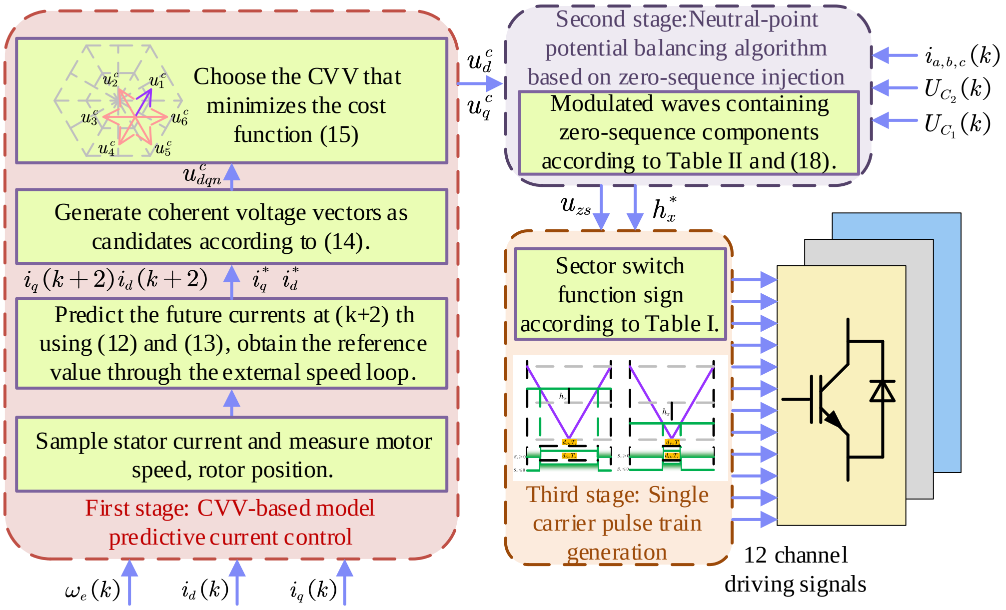

Fig. 6. 5. Block diagram of proposed MPC algorithm.

6.6. Experimental Results

6.6.1. Steady-State Performance Comparison

First, the steady-state performance tests were carried out under the command of 500 r/min with the rated load. To verify the superiority of the proposed method, the experimental results of the conventional multi-virtual-vector MPC (M2V-MPC) [106] with the same sampling and switching frequency were also presented. The waveforms of speed, three-phase currents for the two methods are shown in Fig. 6. 6, as well as the phase a current harmonic spectrum and the scaled-up d-axis current.

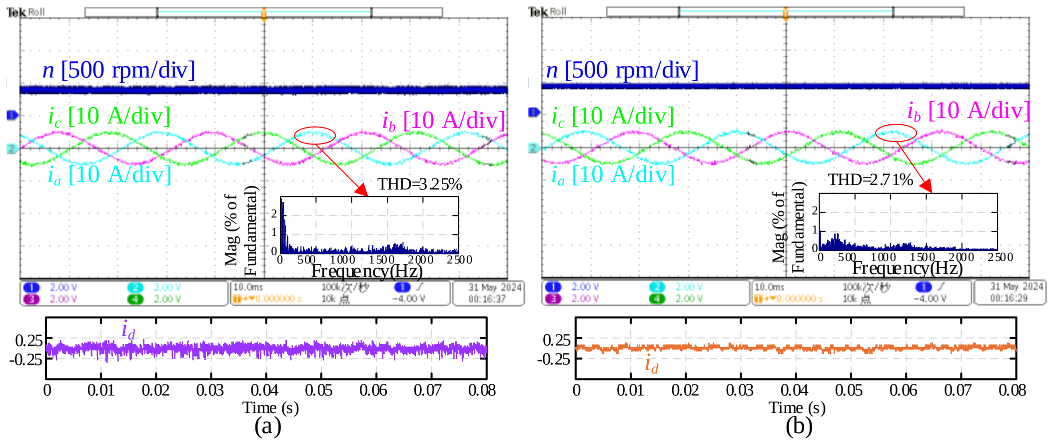

Fig. 6. 6. Comparison of steady-state performance at rated load, 500 r/min. From above to below: speed, three-phase currents, harmonics spectrum, *d*-axis current. (a) M2V-MPC. (b) the proposed method.

It can be seen that both methods track the speed reference well at constant torque, and the proposed method is more stable in comparison. The results of Fast Fourier Analytical Transform (FFT) show that the Total Harmonic Distortion (THD) of phase current is 3.25% for the conventional method and 2.71% for the proposed method, which is the effect of using coherent voltage vector and zero-sequence component injection. The proposed method is able to track the *d*-axis current target stably with a maximum tracking error of about 0.15A, which is much lower than that of M2V-MPC. The proposed method is better than MV2-MPC in terms of current quality and *d*-axis current ripple.

Steady-state behavior of the PMSM for the two methods is also tested at 1.25 times the rated speed (1250 r/min), and the waveforms are illustrated in Fig. 6. 7. Although the output currents of both FS-MPC algorithms are sinusoidal, the proposed method has a lower current distortion of 2.55%. The employment of CVVs with adjustable amplitude and moveable start point can still improve the current quality significantly during high-speed operation. It can also be seen from Fig. 6. 7 that the neutral point voltage deviation ($U_{C_1} - U_{C_2}$) in the proposed method is limited to 1.18 V (peak-to-peak), while more spikes are present in M2V-MPC.

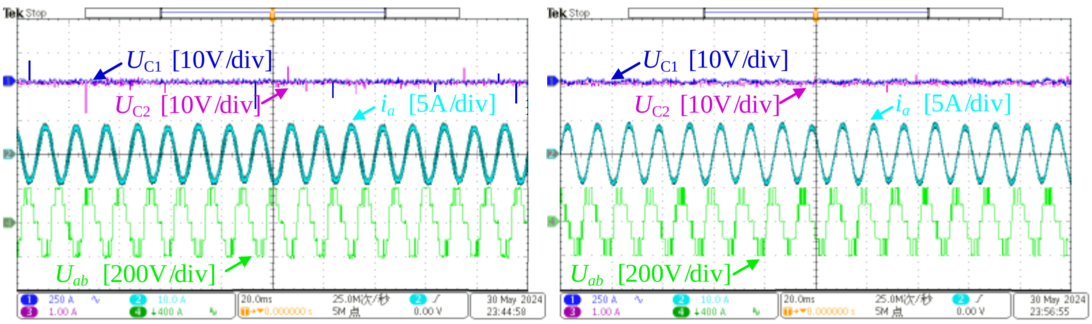

Fig. 6. 7. Comparison of steady-state performance at rated load, 1250 r/min. From above to below: dc-link capacitor voltages, phase-a output currents, lineline voltage. (a) M2V-MPC. (b) the proposed method.

In order to quantitatively compare the steady-state performance of the motors using the two methods, the torque ripple is evaluated using the standard deviation equation.

$$\sigma_{\varepsilon} = \sqrt{\frac{1}{N}\sum_{n=1}^{N}\left(\varepsilon(n) - \varepsilon^{\text{ave}}\right)}, \quad \varepsilon^{\text{ave}} = \frac{1}{N}\sum_{n=1}^{N}\varepsilon(n) \tag{6.14}$$

where N is the number of sampled data; σ_e represents the torque standard deviation; and ε^{ave} is the corresponding mean value.

The steady-state performances across the full motor speed range were experimentally investigated for both methods under rated load, with results presented in Fig. 6. 8. The proposed method demonstrates superior performance throughout the entire speed range.

Numerical comparisons indicate that the average torque ripple of the proposed method is 39.65% lower, and the average current THD is 66.21% lower than that of the M2V-MPC. To evaluate the actual computational efficiency of the proposed methods, the turnaround time was directly measured using the dSPACE1202 control system. Fig. 6. 9 illustrates the algorithm execution times for different methods, all under the same control period of 50 μs. It can be seen that the execution time of the duty cycle optimization MPC (DCOMPC) approach in [107] is 29 μs, while the proposed scheme is 41% faster.

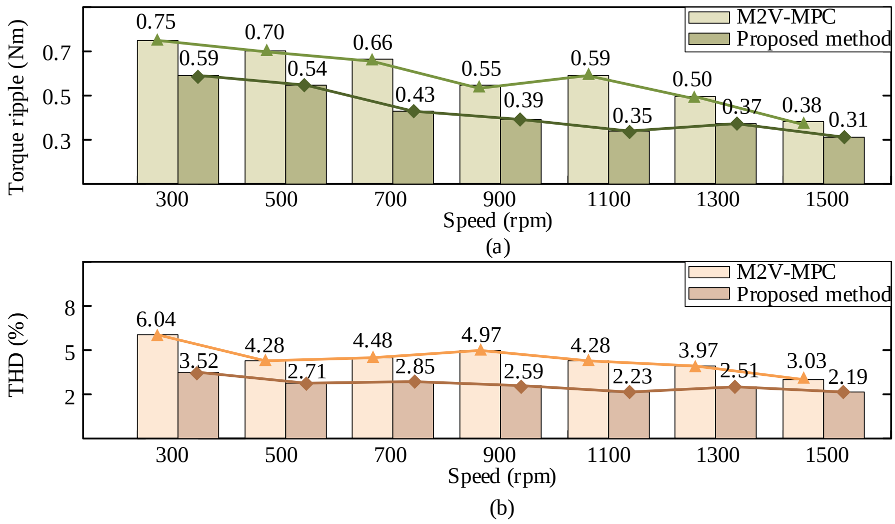

Fig. 6. 8. Quantitative comparison of the control performance of the two methods. (a) Torque ripple. (b) current THD.

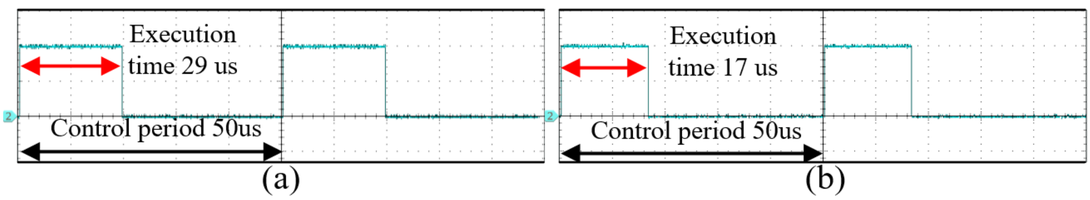

Fig. 6. 9. Algorithm execution time comparison. (a) DCO-MPC. (b) Proposed method.

6.6.2. Performance Evaluation of Transient Response

Apart from the steady-state performance comparison, the dynamic performance of the proposed method is also investigated. Fig. 6. 10 shows the experimental results for the speed and *dq*-axis currents transient response. It can be observed that when the motor starts from standstill to 800 r/min with rated load, the proposed method is able to realize the response within 62 ms. Moreover, Fig. 6. 10(b) shows the ability of the drive to respond to a sudden change in reference speed from 500 r/min to 800 r/min at the rated load. The rotor speed quickly reaches the rated speed in just 20ms and i_q tracks its reference well.

To highlight the tracking performance of the proposed methods during transients, Fig. 6. 11 shows the zoomed *d*-axis and *q*-axis current transient waveforms for the two methods during the speed reversal (from forward to reverse). It can be observed that the settling time of the proposed method is only 1.08 *ms*, which is 1.7 times shorter than that of M2V-MPC, and the overshoot is significantly lower. Due to the candidate vector coherent processing, the output voltage does not change abruptly, which results in a small *dq*-axis current ripple, but the fast response is still maintained.

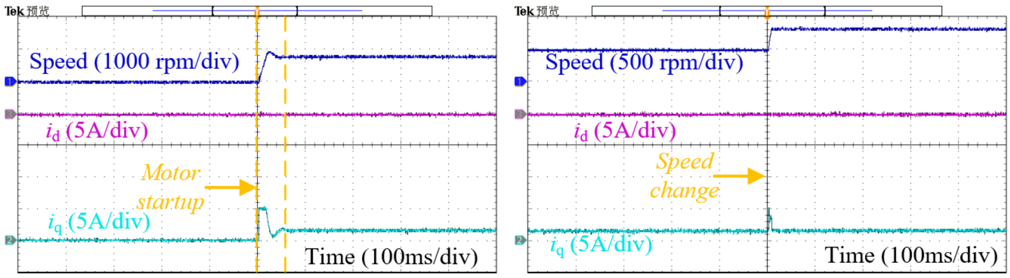

(a) (b)

Fig. 6. 10. Dynamic response of motor speed and *dq*-axis current. (a) Start from standstill to 800r/min with rated load. (b) Speed changes from 500 to 800 r/min with the rated load.

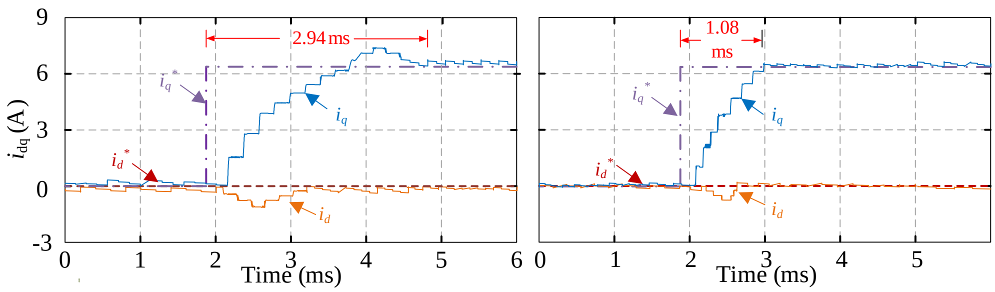

(a) (b)

Fig. 6. 11. *dq*-axis currents transient-state response during speed reversal. (a) M2V-MPC. (b) the proposed method.

Fig. 6. 12 presents experimental results when ε_α is set to 0.3 and 0.5, respectively. The current tracking speed of ε_α = 0.5 is similar to that of ε_α = 0.3 when the *q*-axis reference current is increased abruptly from 1A to 3A, but the current ripples are much smaller than that of ε_α = 0.3. It is evident that the current ripples reduce significantly with increasing ε_α, but a value of 0.5 also ensures the same level of dynamic performance.

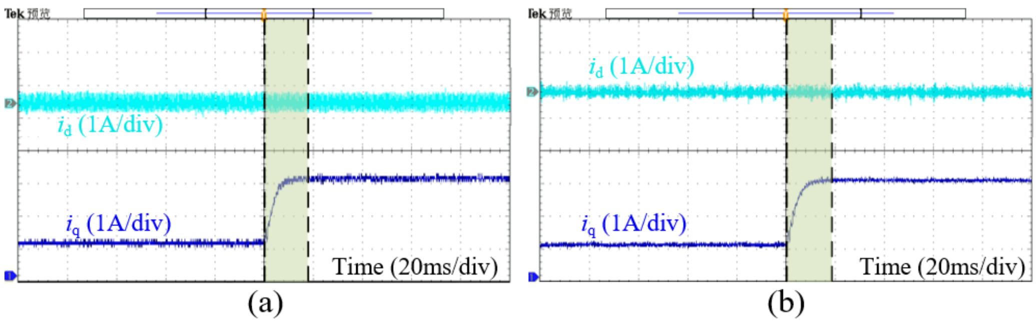

Fig. 6. 12. Comparison of current transient response performance with different values of ε_α. (a) ε_α = 0.3. (b) ε_α = 0.5.

6.6.3. Investigation of Average Switching Frequency

The single carrier modulation mode and pulse train generation adopted in the proposed scheme can avoid two-level jumps and the switching loss is reduced. To highlight this advantage, the average switching frequency of the six IGBTs at the top of the 3L-NPC inverter is defined as follows

$$f_{sw} = \frac{1}{6T}\sum_{k=1}^{6} N_{c_k} \tag{1.1}$$

where N_{c_k} is the number of states switching of the kth IGBT during the stator period T.

For a fair comparison in the previous steady-state experiments, the average switching frequencies of the two methods were kept at approximately the same level. When the sampling frequency is controlled to be fixed, the average switching frequencies of the two control schemes at different speeds are tested, and the results are shown in Fig. 6. 13(a). It is obvious that the proposed strategy exhibits lower f_{sw} over the entire speed range, which verifies the benefit of limiting state switching to the two types of (0↔1) and (-1↔0). At the rated speed, f_{sw} of M2V-MPC is 4.514 kHz and f_{sw} of the proposed method is 3.536 kHz. Therefore, the latter reduces the average switching frequency by 21.67% relative to M2V-MPC, although the switching frequency is not included in the cost function, and there is no need to tune the weighting factor.

Fig. 6. 13 (b) shows the switching status of the proposed method during the transient process of the previous reversal test, with f_{sw} updated every 10 ms. It can be seen that during the dynamic process, the average switching frequency temporarily fluctuates. After the transient process ends, f_{sw} can be restored to the level before the speed reversal. The tests show that the specially designed coherent voltage vector changes rapidly in response to transient changes and remain relatively stable after tracking the given value.

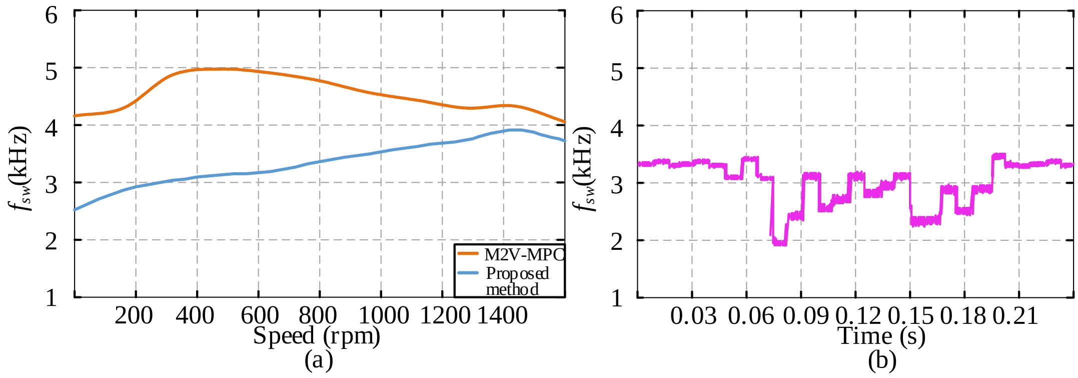

Fig. 6. 13. Average switching frequency of the experiment at the fixed sampling frequency. (a) Comparison of f_{sw} at various speeds. (b) Responses of f_{sw} during speed reversal.

6.7. Conclusion

In this chapter, a novel coherent voltage vector-based MPC method is proposed and has been experimentally applied to a PMSM system. Candidate vectors are coherently processed, and the starting point can be movable according to the optimal vector of the previous instant, thus avoiding sudden changes in the output voltage. Zero-sequence component injection is introduced to balance the neutral point potential, the amplitude of which is judged according to the sector in which the CVV with the minimum tracking error is located. Another innovative point of the proposed method is in the generation of the pulse sequence, which is not only easy to implement, but also does not involve two-step jumps. The experimental results confirmed that the proposed MPC method could achieve better output current quality in the steady-state and faster transient response in comparison with the conventional multi-vector MPC. Under the full speed range conditions, the proposed method features lower switching frequency, and the average torque ripple is reduced by 39.65%.

CHAPTER 7. SUMMARY AND FUTURE WORK

7.1. Summary

FS-MPC, as a high-performance motor control strategy, is characterized by its simple principles, ease of implementation, and capability to handle system nonlinearities and multi-constraint problems. As a result, it has become a research hotspot in the field of motor control. This thesis focuses on the study of Surface Permanent Magnet Synchronous Motors (SPMSM) driven by conventional two-level and three-level NPC-type inverters, employing FS-MPC to enhance the control performance of the entire motor speed regulation system. The following is a brief summary of the work conducted in this thesis:

1. The research background is briefly outlined based on a survey of relevant literature, highlighting both domestic and international research achievements. A concise overview of several commonly used control strategies in current motor control systems is presented. Subsequently, a detailed review of the theoretical development and state-of-the-art research on MPC is conducted, accompanied by an analysis of the main issues associated with traditional FS-MPC and FS-MPC-based common mode voltage (CMV) suppression methods.

2. Various common types of Permanent Magnet Synchronous Motors (PMSM) are introduced from the perspective of motor structure, along with their respective advantages and disadvantages. For the SPMSM, its mathematical model is derived in

different coordinate systems. The basic principles of MPC are succinctly outlined, with a particular focus on the PMSM current control strategy based on FS-MPC. Simulation results using Simulink validate the constructed PMSM drive system, indicating that the system exhibits excellent speed regulation performance and stability, capable of meeting the requirements under sudden load changes.

3. The fundamental principles of deadbeat calculation for reference voltage vectors are introduced, alongside an analysis of the causes of CMV and the provision of relevant calculation formulas. A novel modulation method is proposed based on the sector switching law during motor operation, with a detailed discussion of the design process and applicable rules. An experimental platform for the SPMSM driven by a traditional two-level inverter is established, and comparative experiments demonstrate that the proposed method achieves high control performance under varying operating conditions while effectively suppressing CMV.

4. The topological structure of the three-level inverter is introduced, describing the operating states of the NPC-type three-level inverter. A permanent magnet synchronous motor drive system based on the NPC three-level inverter is constructed, encompassing aspects such as circuit topology, control strategy, and parameter design. A three-level FS-MPC method mapped to sub-hexagons is proposed. Finally, Simulink simulations verify that the simplified algorithm not only achieves good control performance but also significantly reduces computational load.

5. A multi-vector FC-MPC method with hysteresis control is proposed, accompanied by an optimization design for dwell time. This method no longer relies on

inductance parameters but incorporates NPP balancing and CMV suppression into the candidate set updating and output vector reconfiguration process. An experimental platform for servo control of a permanent magnet motor driven by a three-level NPC inverter is built, and experimental results demonstrate that the proposed method effectively eliminates NPP imbalance and suppresses CMV while improving parameter adaptability.

6. Coherent voltage vector-based model predictive control (CVV-MPC) for 3L-NPC inverters is proposed. The 27 basic voltage vectors of the three-level inverter are coherentized before being applied to predict the operating state at the next instant. Only the finite set of coherent voltage vectors adjacent to the previous output voltage is computed, which is computationally efficient. The sudden change in output voltage is simply and effectively avoided, which in turn achieves a smooth and accurate control effect. The neutral voltage balance is explicitly considered in the prediction process, so as to synthesize the optimal coherent voltage vector. A single carrier mode applicable to the above algorithm is realized.

7.2. Future Work

This thesis addresses some research work on the MPC control strategy for PMSM. However, due to limitations in time, resources, and capability, certain aspects remain under-investigated, and some issues need to be resolved. The summary is as follows:

1) Through experimental analysis, the impact of parameter mismatches on motor control has been identified. The proposed modified model predictive current control

effectively corrects various parameter mismatch scenarios. The next step is to conduct both online and offline parameter identification, including inductance, resistance, and flux linkage, followed by experimental validation.

2) The speed outer loop utilizes a PI controller, resulting in a simple control method. The next step will involve exploring other control schemes, such as robust control, adaptive control, active disturbance rejection control, and backstepping control, with the aim of achieving better control performance.

3) The PMSM used in the experiments is equipped with a 5000-line encoder. In the future, we hope to achieve control that does not rely on optical encoders or other speed and position sensors.

REFERENCES

[1] Y. Luo and C. Liu, "Elimination of Harmonic Currents Using a Reference Voltage Vector Based-Model Predictive Control for a Six-Phase PMSM Motor," *IEEE Transactions on Power Electronics*, vol. 34, no. 7, pp. 6960-6972, 2019.

[2] I. M. Alsofyani and K. -B. Lee, "A Unidirectional Voltage Vector Preselection Strategy for Optimizing Model Predictive Torque Control With Discrete Space Vector Modulation of IPMSM," *IEEE Transactions on Industrial Electronics*, vol. 69, no. 12, pp. 12305-12315, 2022.

[3] M. H. Vafaie, B. M. Dehkordi, P. Moallem and A. Kiyoumarsi, "Improving the Steady-State and Transient-State Performances of PMSM Through an Advanced Deadbeat Direct Torque and Flux Control System," *IEEE Transactions on Power Electronics*, vol. 32, no. 4, pp. 2964-2975, 2017.

[4] V. Madonna, P. Giangrande, and M. Galea, "Electrical power generation in aircraft: Review, challenges, and opportunities," *IEEE Transactions on Transportation Electrification*, vol. 4, no. 3, pp. 646-659, 2018.

[5] A. Griffo, R. Wrobel, P. H. Mellor, and J. M. Yon, "Design and characterization of a three-phase brushless exciter for aircraft starter/generator," *IEEE Transactions on Industry Applications*, vol. 49, no. 5, pp. 2106-2115, 2013.

[6] Z. Xue, S. Niu and X. Li, "A Simplified Multivector-Based Model Predictive Current Control for PMSM With Enhanced Performance," *IEEE Transactions on Transportation Electrification*, vol. 9, no. 3, pp. 4032-4044,. 2023.

[7] L. Jin, Y. Mao, X. Wang, L. Lu and Z. Wang, "Online Data-Driven Fault Diagnosis of Dual Three-Phase PMSM Drives Considering Limited Labeled Samples," *IEEE Transactions on Industrial Electronics*, vol. 71, no. 7, pp. 6797-6808, 2024.

[8] R. Bojoi, A. Cavagnino, A. Tenconi, and S. Vaschetto, "Control of shaft-line-embedded multiphase starter/generator for aero-engine," *IEEE Transactions on Industrial Electronics*, vol. 63, no. 1, pp. 641-652, 2015.

[9] Z. Dong, Z. Song, W. Wang and C. Liu, "Improved Zero-Sequence Current Hysteresis Control-Based Space Vector Modulation for Open-End Winding PMSM Drives With Common DC Bus," *IEEE Transactions on Industrial Electronics*, vol. 70, no. 10, pp. 10755-10760, 2023.

[10] X. Zhang, L. Sun, K. Zhao, and L. Sun, "Nonlinear speed control for PMSM system using sliding-mode control and disturbance compensation techniques," *IEEE Transactions on Power Electronics,* vol. 28, no. 3, pp. 1358-1365, 2012.

[11] W. Wang, S. Niu and X. Zhao, "A Novel Field and Armature Synchronous Pulse Injection Method for Sensorless Drive Control of 12/10 DC Vernier Reluctance Machine," *IEEE Transactions on Energy Conversion*, vol. 38, no. 3, pp. 2126-2135, 2023.

[12] Y. Bi, W. Fu, S. Niu, X. Zhao, J. Huang and Z. Qiao, "Torque Enhancement of a Dual-PM Flux-Switching Machine With Improved Multiple High-Order Working Harmonics," *IEEE Transactions on Transportation Electrification*, vol. 10, no. 2, pp. 2830-2843, 2024.

[13] P. B. Reddy, A. M. El-Refaie, K.-K. Huh, J. K. Tangudu, and T. M. Jahns, "Comparison of interior and surface PM machines equipped with fractional-slot concentrated windings for hybrid traction applications," *IEEE Transactions on Energy Conversion,* vol. 27, no. 3, pp. 593-602, 2012.

[14] I. Boldea, L. N. Tutelea, L. Parsa, and D. Dorrell, "Automotive electric propulsion systems with reduced or no permanent magnets: An overview," *IEEE Transactions on Industrial Electronics,* vol. 61, no. 10, pp. 5696-5711, 2014.

[15] X. Zhao, S. Niu, X. Zhang, and W. Fu, "Design of a new relieving-DC-saturation hybrid reluctance machine for fault-tolerant in-wheel direct drive,"

IEEE Transactions on Industrial Electronics, vol. 67, no. 11, pp. 9571-9581, 2019.

[16] Z. Wang, J. Chen, M. Cheng, and K. Chau, "Field-oriented control and direct torque control for paralleled VSIs fed PMSM drives with variable switching frequencies," *IEEE Transactions on Power Electronics*, vol. 31, no. 3, pp. 2417-2428, 2015.

[17] A. H. Abosh, Z. Q. Zhu and Y. Ren, "Reduction of Torque and Flux Ripples in Space Vector Modulation-Based Direct Torque Control of Asymmetric Permanent Magnet Synchronous Machine," *IEEE Transactions on Power Electronics*, vol. 32, no. 4, pp. 2976-2986, 2017.

[18] Y. Inoue, S. Morimoto and M. Sanada, "Examination and Linearization of Torque Control System for Direct Torque Controlled IPMSM," *IEEE Transactions on Industry Applications*, vol. 46, no. 1, pp. 159-166, 2010.

[19] M. H. Vafaie, B. Mirzaeian Dehkordi, P. Moallem and A. Kiyoumarsi, "A New Predictive Direct Torque Control Method for Improving Both Steady-State and Transient-State Operations of the PMSM," *IEEE Transactions on Power Electronics*, vol. 31, no. 5, pp. 3738-3753, 2016.

[20] X. Yuan and C. H. T. Lee, "A Simple Three-Degree-of-Freedom Digital Current Controller With Dead Beat Response for AC Machines," *IEEE Transactions on Industrial Electronics*, vol. 69, no. 8, pp. 7848-7858, 2022.

[21] W. Song, J. Li, C. Ma, Y. Xia and B. Yu, "A Simple Tuning Method of PI Regulators in FOC for PMSM Drives Based on Deadbeat Predictive Conception," *IEEE Transactions on Transportation Electrification*, vol. 10, no. 4, pp. 9852-9863, 2024.

[22] J. Lara, J. Xu and A. Chandra, "Effects of Rotor Position Error in the Performance of Field-Oriented-Controlled PMSM Drives for Electric Vehicle Traction Applications," *IEEE Transactions on Industrial Electronics*, vol. 63, no. 8, pp. 4738-4751, 2016.

[23] Z. Wang, J. Chen, M. Cheng and K. T. Chau, "Field-Oriented Control and Direct Torque Control for Paralleled VSIs Fed PMSM Drives With Variable Switching Frequencies," *IEEE Transactions on Power Electronics*, vol. 31, no. 3, pp. 2417-2428, 2016.

[24] Y. Ren, Z. Q. Zhu, and J. Liu, "Direct torque control of permanentmagnet synchronous machine drives with a simple duty ratio regulator," *IEEE Transactions on Industrial Electronics*, vol. 61, no. 10, pp. 5249–5258, 2014.

[25] M. R. Nikzad, B. Asaei and S. O. Ahmadi, "Discrete Duty-Cycle-Control Method for Direct Torque Control of Induction Motor Drives With Model Predictive Solution," *IEEE Transactions on Power Electronics*, vol. 33, no. 3, pp. 2317-2329, 2018.

[26] X. Lin, W. Huang, W. Jiang, Y. Zhao and S. Zhu, "Deadbeat Direct Torque and Flux Control for Permanent Magnet Synchronous Motor Based on Stator Flux Oriented," *IEEE Transactions on Power Electronics*, vol. 35, no. 5, pp. 5078-5092, 2020.

[27] S. G. Petkar and V. K. Thippiripati, "A Novel Duty-Controlled DTC of a Surface PMSM Drive With Reduced Torque and Flux Ripples," I*EEE Transactions on Industrial Electronics*, vol. 70, no. 4, pp. 3373-3383, 2023.

[28] V. s. r. Chagam redd and S. Devabhaktuni, "Reduction of Stator Flux Ripple and Current Harmonic Distortion using Constant Switching Flux Controller-based DTC of Five-Phase Induction Motor," *IEEE Latin America Transactions*, vol. 21, no. 8, pp. 915-924, 2023.

[29] I. M. Alsofyani, K. Y. Kim, S. S. Lee and K. -B. Lee, "A Modified Flux Regulation Method to Minimize Switching Frequency and Improve DTC-Hysteresis-Based Induction Machines in Low-Speed Regions," *IEEE Journal of Emerging and Selected Topics in Power Electronics*, vol. 7, no. 4, pp. 2346-2355, 2019.

[30] E. Daryabeigi and S. Vaez-Zadeh, "A Combined Control for Fast and Smooth Performance of IPM Motor Drives Over Wide Operating Conditions," *IEEE Transactions on Energy Conversion*, vol. 33, no. 3, pp. 1384-1391, 2018.

[31] M. J. Navardi, J. Milimonfared and H. A. Talebi, "Torque and Flux Ripples Minimization of Permanent Magnet Synchronous Motor by a Predictive-Based Hybrid Direct Torque Control," *IEEE Journal of Emerging and Selected Topics in Power Electronics*, vol. 6, no. 4, pp. 1662-1670, 2018.

[32] B. Sarsembayev, K. Suleimenov and T. D. Do, "High Order Disturbance Observer Based PI-PI Control System With Tracking Anti-Windup Technique for Improvement of Transient Performance of PMSM," *IEEE Access*, vol. 9, pp. 66323-66334, 2021.

[33] C. Lian *et al.*, "Current Harmonic Minimum Pulse Width Modulation for Dual Three-Phase PMSM System With 3L-NPC Inverter and Output Filter," *IEEE Transactions on Power Electronics*, vol. 40, no. 2, pp. 2847-2859, 2025.

[34] K. Lv, D. Wang, W. Huang and J. Hu, "Research on Fault Indicator for Integrated Fault Diagnosis System of PMSM Based on Stator Tooth Flux," *IEEE Journal of Emerging and Selected Topics in Power Electronics*, vol. 12, no. 1, pp. 985-996, 2024.

[35] W. Huang, J. Du, W. Hua, K. Bi and Q. Fan, "A Hybrid Model-Based Diagnosis Approach for Open-Switch Faults in PMSM Drives," *IEEE Transactions on Power Electronics*, vol. 37, no. 4, pp. 3728-3732, 2022.

[36] X. Song, B. Han, S. Zheng and S. Chen, "A Novel Sensorless Rotor Position Detection Method for High-Speed Surface PM Motors in a Wide Speed Range," *IEEE Transactions on Power Electronics*, vol. 33, no. 8, pp. 7083-7093, 2018.

[37] R. M. Pindoriya, B. S. Rajpurohit and R. Kumar, "A Novel Application of Harmonics Spread Spectrum Technique for Acoustic Noise and Vibration Reduction of PMSM Drive," *IEEE Access*, vol. 8, pp. 103273-103284, 2020.

[38] R. Yan, D. Wang, C. Wang, W. Miao and X. Wang, "Analytical Approach and Experimental Validation of Sideband Electromagnetic Vibration and Noise in

PMSM Drive With Voltage-Source Inverter by SVPWM Technique," *IEEE Transactions on Magnetics*, vol. 61, no. 1, pp. 1-6, 2025.

[39] L. Dai, J. Gao, S. Niu, K. Liu, S. Huang and W. L. Chan, "Cogging Torque Suppression for IPMSM Based on Flux Harmonic Configuration," *IEEE Transactions on Industrial Electronics*, vol. 72, no. 3, pp. 2903-2913, 2025.

[40] K. Wang, B. Zhou, X. Zhou, S. Jiang, and J. Wei, "The output voltage control strategy for DSEG with controlled rectification based on conduction angle estimation," *IEEE Transactions on Industrial Electronics*, vol. 67, no. 5, pp. 3350-3360, 2019.

[41] S. Kwak, U. -C. Moon and J. -C. Park, "Predictive-Control-Based Direct Power Control With an Adaptive Parameter Identification Technique for Improved AFE Performance," *IEEE Transactions on Power Electronics*, vol. 29, no. 11, pp. 6178-6187, Nov. 2014.

[42] G. Feng, C. Lai and N. C. Kar, "A Closed-Loop Fuzzy-Logic-Based Current Controller for PMSM Torque Ripple Minimization Using the Magnitude of Speed Harmonic as the Feedback Control Signal," *IEEE Transactions on Industrial Electronics*, vol. 64, no. 4, pp. 2642-2653, April 2017.

[43] T. T. Nguyen, H. N. Tran, T. H. Nguyen and J. W. Jeon, "Recurrent Neural Network-Based Robust Adaptive Model Predictive Speed Control for PMSM With Parameter Mismatch," *IEEE Transactions on Industrial Electronics*, vol. 70, no. 6, pp. 6219-6228, 2023.

[44] M. Abdelrahem, C. M. Hackl, R. Kennel, and J. Rodriguez, "Computationally efficient finite-position-set-phase-locked loop for sensorless control of PMSGs in wind turbine applications," *IEEE Transactions on Power Electronics*, vol. 36, no. 3, pp. 3007-3016, 2020.

[45] R. Sreejith and B. Singh, "Sensorless predictive current control of PMSM EV drive using DSOGI-FLL based sliding mode observer," *IEEE Transactions on Industrial Electronics*, vol. 68, no. 7, pp. 5537-5547, 2020.

[46] J. Rodriguez *et al*., "Predictive Current Control of a Voltage Source Inverter," *IEEE Transactions on Industrial Electronics*, vol. 54, no. 1, pp. 495-503, 2007.

[47] X. Zhang, B. Hou and Y. Mei, "Deadbeat Predictive Current Control of Permanent-Magnet Synchronous Motors with Stator Current and Disturbance Observer," *IEEE Transactions on Power Electronics*, vol. 32, no. 5, pp. 3818-3834, 2017.

[48] P. G. Carlet, A. Favato, S. Bolognani and F. Dörfler, "Data-Driven Continuous-Set Predictive Current Control for Synchronous Motor Drives," *IEEE Transactions on Power Electronics*, vol. 37, no. 6, pp. 6637-6646, 2022.

[49] T. Li, X. Sun, M. Yao, D. Guo and Y. Sun, "Improved Finite Control Set Model Predictive Current Control for Permanent Magnet Synchronous Motor With Sliding Mode Observer," *IEEE Transactions on Transportation Electrification*, vol. 10, no. 1, pp. 699-710, 2024.

[50] L. Xu *et al*., "Multimode Ultralocal-Model-Based Predictive Current Control of a Variable Reluctance Flux Controllable Permanent Magnet Motor," *IEEE Transactions on Industrial Electronics*, vol. 72, no. 2, pp. 1391-1401, 2025.

[51] S. Lin, X. Fang, X. Wang, Z. Yang and F. Lin, "Multiobjective Model Predictive Current Control Method of Permanent Magnet Synchronous Traction Motors With Multiple Current Bounds in Railway Application," *IEEE Transactions on Industrial Electronics*, vol. 69, no. 12, pp. 12348-12357, 2022.

[52] Y. Wei, Y. Wei, Y. Sun, H. Qi and X. Guo, "Prediction Horizons Optimized Nonlinear Predictive Control for Permanent Magnet Synchronous Motor Position System," *IEEE Transactions on Industrial Electronics*, vol. 67, no. 11, pp. 9153-9163, 2020.

[53] X. Zhang, Z. Liu, P. Zhang and Y. Zhang, "Model Predictive Current Control for PMSM Drives Based on Nonparametric Prediction Model," *IEEE Transactions on Transportation Electrification*, vol. 10, no. 1, pp. 711-719, 2024.

[54] Y. Zhou, Y. Wang, H. Li and J. Mao, "Optimal Solution for Model Predictive Current Control of Surface Mounted Permanent Magnet Synchronous Motor Based on Trigonometrical Substitution," *IEEE Transactions on Energy Conversion*, vol. 37, no. 4, pp. 2338-2347, 2022.

[55] X. Liu, H. Yang, H. Lin, F. Yu and Y. Yang, "A Novel Finite-Set Sliding-Mode Model-Free Predictive Current Control for PMSM Drives Without DC-Link Voltage Sensor," *IEEE Transactions on Power Electronics*, vol. 39, no. 1, pp. 320-331, 2024.

[56] Z. Zhang, Y. Liu, X. Liang, H. Guo and X. Zhuang, "Robust Model Predictive Current Control of PMSM Based on Nonlinear Extended State Observer," *IEEE Journal of Emerging and Selected Topics in Power Electronics*, vol. 11, no. 1, pp. 862-873, 2023.

[57] X. Song, H. Wang, X. Ma, X. Yuan and X. Wu, "Robust Model Predictive Current Control for a Nine-Phase Open-End Winding PMSM With High Computational Efficiency," *IEEE Transactions on Power Electronics*, vol. 38, no. 11, pp. 13933-13943, 2023.

[58] S. Liu and C. Liu, "Virtual-Vector-Based Robust Predictive Current Control for Dual Three-Phase PMSM," *IEEE Transactions on Industrial Electronics*, vol. 68, no. 3, pp. 2048-2058, 2021.

[59] Z. Zhang, Q. Sun and Q. Zhang, "A Computationally Efficient Model Predictive Control Method for Dual Three-Phase PMSM of Electric Vehicle With Fixed Switching Frequency," *IEEE Transactions on Industry Applications*, vol. 60, no. 1, pp. 1105-1116, 2024.

[60] W. Chen, S. Zeng, G. Zhang, T. Shi and C. Xia, "A Modified Double Vectors Model Predictive Torque Control of Permanent Magnet Synchronous Motor," *IEEE Transactions on Power Electronics*, vol. 34, no. 11, pp. 11419-11428, 2019.

[61] C. A. Rojas, M. Aguirre, S. Kouro, T. Geyer and E. Gutierrez, "Leakage Current Mitigation in Photovoltaic String Inverter Using Predictive Control With Fixed

Average Switching Frequency," *IEEE Transactions on Industrial Electronics*, vol. 64, no. 12, pp. 9344-9354, 2017.

[62] S. -W. Kang, J. -H. Soh and R. -Y. Kim, "Symmetrical Three-Vector-Based Model Predictive Control With Deadbeat Solution for IPMSM in Rotating Reference Frame," *IEEE Transactions on Industrial Electronics*, vol. 67, no. 1, pp. 159-168, 2020.

[63] H. Li, M. Lin, M. Yin, J. Ai and W. Le, "Three-Vector-Based Low-Complexity Model Predictive Direct Power Control Strategy for PWM Rectifier Without Voltage Sensors," *IEEE Journal of Emerging and Selected Topics in Power Electronics*, vol. 7, no. 1, pp. 240-251, March 2019.

[64] M. Wu, X. Sun, J. Zhu, G. Lei and Y. Guo, "Improved Model Predictive Torque Control for PMSM Drives Based on Duty Cycle Optimization," *IEEE Transactions on Magnetics*, vol. 57, no. 2, pp. 1-5, 2021.

[65] L. Guo, N. Jin, C. Gan and K. Luo, "Hybrid Voltage Vector Preselection-Based Model Predictive Control for Two-Level Voltage Source Inverters to Reduce the Common-Mode Voltage," *IEEE Transactions on Industrial Electronics*, vol. 67, no. 6, pp. 4680-4691, 2020.

[66] B. Xu, Q. Jiang, W. Ji and S. Ding, "An Improved Three-Vector-Based Model Predictive Current Control Method for Surface-Mounted PMSM Drives," *IEEE Transactions on Transportation Electrification*, vol. 8, no. 4, pp. 4418-4430, 2022.

[67] S. G. Petkar and V. K. Thippiripati, "Enhanced Predictive Current Control of PMSM Drive With Virtual Voltage Space Vectors," *IEEE Journal of Emerging and Selected Topics in Industrial Electronics*, vol. 3, no. 3, pp. 834-844, 2022.

[68] Y. Han, C. Gong, L. Yan, H. Wen, Y. Wang and K. Shen, "Multiobjective Finite Control Set Model Predictive Control Using Novel Delay Compensation Technique for PMSM," *IEEE Transactions on Power Electronics*, vol. 35, no. 10, pp. 11193-11204, 2020.

[69] L. Gao, J. E. Fletcher and L. Zheng, "Low-Speed Control Improvements for a Two-Level Five-Phase Inverter-Fed Induction Machine Using Classic Direct Torque Control," *IEEE Transactions on Industrial Electronics*, vol. 58, no. 7, pp. 2744-2754, 2011.

[70] F. Wang, S. Li, X. Mei, W. Xie, J. Rodríguez and R. M. Kennel, "Model-Based Predictive Direct Control Strategies for Electrical Drives: An Experimental Evaluation of PTC and PCC Methods," *IEEE Transactions on Industrial Informatics*, vol. 11, no. 3, pp. 671-681, 2015.

[71] C. D. Townsend, T. J. Summers, J. Vodden, A. J. Watson, R. E. Betz and J. C. Clare, "Optimization of Switching Losses and Capacitor Voltage Ripple Using Model Predictive Control of a Cascaded H-Bridge Multilevel StatCom," *IEEE Transactions on Power Electronics*, vol. 28, no. 7, pp. 3077-3087, 2013.

[72] Z. Zhang, C. M. Hackl and R. Kennel, "Computationally Efficient DMPC for Three-Level NPC Back-to-Back Converters in Wind Turbine Systems With PMSG," *IEEE Transactions on Power Electronics*, vol. 32, no. 10, pp. 8018-8034, Oct. 2017.

[73] T. Liu, A. Chen and Y. Huang, "Multivector Model Predictive Current Control for Paralleled Three-Level T-Type Inverters With Circulating Current Elimination," I*EEE Transactions on Industrial Electronics*, vol. 70, no. 8, pp. 8042-8052, 2023.

[74] F. Guo *et al.*, "An Advanced Dual-Carrier-Based Multi-Optimized PWM Strategy of Three-Level Neutral-Point-Clamped Converters for More-Electric-Aircraft Applications," *IEEE Transactions on Energy Conversion*, vol. 39, no. 1, pp. 356-367, 2024.

[75] W. Ding, C. Zhang, F. Gao, B. Duan and H. Qiu, "A Zero-Sequence Component Injection Modulation Method With Compensation for Current Harmonic Mitigation of a Vienna Rectifier," *IEEE Transactions on Power Electronics*, vol. 34, no. 1, pp. 801-814, 2019.

[76] K. Antoniewicz, M. Jasinski, M. P. Kazmierkowski and M. Malinowski, "Model Predictive Control for Three-Level Four-Leg Flying Capacitor Converter Operating as Shunt Active Power Filter," *IEEE Transactions on Industrial Electronics*, vol. 63, no. 8, pp. 5255-5262, 2016.

[77] Y. Li, F. Diao, Y. Zhao and H. A. Mantooth, "A Hybrid Model Predictive Control for a Seven-Level Hybrid Multilevel Converter With Independent Low-Frequency and High-Frequency Stages," *IEEE Transactions on Power Electronics,* vol. 37, no. 5, pp. 5256-5271, 2022.

[78] H. Zhang, C. Zhang, X. Xing, C. Liu, X. Li and B. Zhang, "Three-Layer Double-Vector Model Predictive Control Strategy for Current Harmonic Reduction and Neutral-Point Voltage Balance in Vienna Rectifier," *IEEE Transactions on Transportation Electrificatio*n, vol. 8, no. 1, pp. 251-262 2022.

[79] S. Y. Kuai, S. Zhao, F. P. Heng, and X. Cui, "Position sensorless technology of switched reluctance motor drives including mutual inductance," *IET Electric Power Applications*, Article vol. 11, no. 6, pp. 1085-1094, 2017, doi: 10.1049/iet-epa.2016.0490.

[80] U. -M. Choi, F. Blaabjerg and K. -B. Lee, "Reliability Improvement of a T-Type Three-Level Inverter With Fault-Tolerant Control Strategy," *IEEE Transactions on Power Electronics,* vol. 30, no. 5, pp. 2660-2673, 2015.

[81] V. Yaramasu and B. Wu, "Predictive Control of a Three-Level Boost Converter and an NPC Inverter for High-Power PMSG-Based Medium Voltage Wind Energy Conversion Systems," *IEEE Transactions on Power Electronics*, vol. 29, no. 10, pp. 5308-5322, 2014.

[82] B. Hu, L. Kang, J. Cheng, X. Luo and Z. Zhang, "Model Predictive Power Control With Dual Vectors for Three-Level Inverter," *IEEE Journal of Emerging and Selected Topics in Power Electronics,* vol. 7, no. 4, pp. 2204-2212, 2019.

[83] M. Krishnamurthy, C. S. Edrington, and B. Fahimi, "Prediction of rotor position at standstill and rotating shaft conditions in switched reluctance machines," *IEEE Transactions on Power Electronics,* vol. 21, no. 1, pp. 225-233, 2006.

[84] M. Schweizer and J. W. Kolar, "Design and Implementation of a Highly Efficient Three-Level T-Type Converter for Low-Voltage Applications," *IEEE Transactions on Power Electronics*, vol. 28, no. 2, pp. 899-907, 2013.

[85] H. T. Nguyen and J. -W. Jung, "Finite Control Set Model Predictive Control to Guarantee Stability and Robustness for Surface-Mounted PM Synchronous Motors," *IEEE Transactions on Industrial Electronics*, vol. 65, no. 11, pp. 8510-8519, 2018.

[86] D. Zhou, L. Ding and Y. Li, "Two-Stage Optimization-Based Model Predictive Control of 5L-ANPC Converter-Fed PMSM Drives," *IEEE Transactions on Industrial Electronics*, vol. 68, no. 5, pp. 3739-3749, 2021.

[87] S. Vazquez, P. Acuna, R. P. Aguilera, J. Pou, J. I. Leon and L. G. Franquelo, "DC-Link Voltage-Balancing Strategy Based on Optimal Switching Sequence Model Predictive Control for Single-Phase H-NPC Converters," *IEEE Transactions on Industrial Electronics*, vol. 67, no. 9, pp. 7410-7420, 2020.

[88] Q. Liu and K. Hameyer, "Torque Ripple Minimization for Direct Torque Control of PMSM With Modified FCSMPC," *IEEE Transactions on Industry Applications*, vol. 52, no. 6, pp. 4855-4864, 2016.

[89] S. Suresh and R. P. P., "Virtual Space Vector-Based Direct Torque Control Schemes for Induction Motor Drives," *IEEE Transactions on Industry Applications*, vol. 56, no. 3, pp. 2719-2728, 2020.

[90] X. Zhang and K. Yan, "Four-Segment-Mode Model Predictive Control for PMSM Drives With Fixed Switching Frequency," *IEEE Transactions on Transportation Electrification*, vol. 9, no. 1, pp. 452-462, 2023.

[91] X. Zhang and B. Hou, "Double Vectors Model Predictive Torque Control Without Weighting Factor Based on Voltage Tracking Error," *IEEE Transactions on Power Electronics*, vol. 33, no. 3, pp. 2368-2380, 2018.

[92] X. Sun, T. Li, M. Yao, G. Lei, Y. Guo and J. Zhu, "Improved Finite-Control-Set Model Predictive Control With Virtual Vectors for PMSHM Drives," *IEEE Transactions on Energy Conversion*, vol. 37, no. 3, pp. 1885-1894, 2022.

[93] J. Rodriguez, S. Bernet, P. K. Steimer, and I. E. Lizama, “A survey on neutral-point-clamped inverters,” *IEEE Transactions on Industrial Electronics*, vol. 57, no. 7, pp. 2219–2230, 2010.

[94] X. Zhang, X. Wu, G. Tan, W. Zhang, and Q. Wang, “A dual-vector model predictive control method with minimum current THD,” *IEEE Transactions on Power Electronics*, vol. 36, no. 9, pp. 9758–9762, 2021.

[95] C. Xiong, H. Xu, T. Guan, and P. Zhou, “A constant switching frequency multiple-vector-based model predictive current control of five-phase PMSM with nonsinusoidal back EMF,” *IEEE Transactions on Industrial Electronics*, vol. 67, no. 3, pp. 1695–1707, 2020.

[96] W. Alhosaini, Y. Wu, and Y. Zhao, “An enhanced model predictive control using virtual space vectors for grid-connected three-level neutralpoint clamped inverters,” *IEEE Transactions on Energy Conversion*, vol. 34, no. 4, pp. 1963–1972, 2019.

[97] F. Donoso, A. Mora, R. Cárdenas, A. Angulo, D. Sáez and M. Rivera, "Finite-Set Model-Predictive Control Strategies for a 3L-NPC Inverter Operating With Fixed Switching Frequency," *IEEE Transactions on Industrial Electronics*, vol. 65, no. 5, pp. 3954-3965, 2018.

[98] Y. Yang *et al.*, "Low Complexity Finite-Control-Set MPC Based on Discrete Space Vector Modulation for T-Type Three-Phase Three-Level Converters," *IEEE Transactions on Power Electronics*, vol. 37, no. 1, pp. 392-403, 2022.

[99] Y. Yang, H. Wen, M. Fan, M. Xie and R. Chen, "Fast Finite-Switching-State Model Predictive Control Method Without Weighting Factors for T-Type Three-Level Three-Phase Inverters," *IEEE Transactions on Industrial Informatics*, vol. 15, no. 3, pp. 1298-1310, 2019.

[100] Y. Yang *et al*., "An Efficient Model Predictive Control Using Virtual Voltage Vectors for Three-Phase Three-Level Converters With Constant Switching Frequency," *IEEE Transactions on Industrial Electronics*, vol. 69, no. 4, pp. 3998-4009, 2022.

[101] D. Zhou, L. Ding and Y. R. Li, "Two-Stage Model Predictive Control of Neutral-Point-Clamped Inverter-Fed Permanent-Magnet Synchronous Motor Drives Under Balanced and Unbalanced DC Links," *IEEE Transactions on Industrial Electronics*, vol. 68, no. 5, pp. 3750-3759, 2021.

[102] X. Chen, D. Xu, F. Liu and J. Zhang, "A Novel Inverter-Output Passive Filter for Reducing Both Differential- and Common-Mode dv/dt at the Motor Terminals in PWM Drive Systems," *IEEE Transactions on Industrial Electronics*, vol. 54, no. 1, pp. 419-426, 2007.

[103] D. Han, C. T. Morris and B. Sarlioglu, "Common-Mode Voltage Cancellation in PWM Motor Drives With Balanced Inverter Topology," *IEEE Transactions on Industrial Electronics*, vol. 64, no. 4, pp. 2683-2688, 2017.

[104] S.-K. Mun and S. Kwak, “Reducing common-mode voltage of threephase VSIs using the predictive current control method based on reference voltage,” *Journal of Power Electronics*, vol. 15, no. 3, pp. 712–720, 2015.

[105] S. Kwak and S. -k. Mun, "Model Predictive Control Methods to Reduce Common-Mode Voltage for Three-Phase Voltage Source Inverters," *IEEE Transactions on Power Electronics*, vol. 30, no. 9, pp. 5019-5035, 2015.

[106] S. K. Hoseini, J. Adabi, and A. Sheikholeslami, “Predictive modulation schemes to reduce common-mode voltage in three-phase inverters-fed AC drive systems,” *IET Power Electronics*, vol. 7, no. 4, pp. 840–849, Apr. 2014.

[107] M. Preindl, E. Schaltz and P. Thogersen, "Switching Frequency Reduction Using Model Predictive Direct Current Control for High-Power Voltage Source Inverters," *IEEE Transactions on Industrial Electronics*, vol. 58, no. 7, pp. 2826-2835, 2011.

[108] C. Qin, C. Zhang, A. Chen, X. Xing, and G. Zhang, “A space vector modulation scheme of the quasi-z-source three-level t-type inverter for common-mode voltage reduction,” *IEEE Transactions on Industrial Electronics*, vol. 65, no. 10, pp. 8340–8350, 2018.

[109] S. Kwak and S. Mun, “Common-mode voltage mitigation with a predictive control method considering dead time effects of three-phase voltage source inverters,” *IET Power Electronics*, vol. 8, no. 9, pp. 1690– 1700, 2014.

[110] P. Liu, S. Duan, C. Yao, and C. Chen, “A double modulation wave CBPWM strategy providing neutral-point voltage oscillation elimination and CMV reduction for three-level NPC inverters,” *IEEE Transactions on Industrial Electronics*, vol. 65, no. 1, pp. 16–26, 2018.

[111] H. Yang, Y. Zhang, and M. Li, “Duty-cycle correction-based model predictive current control for PMSM drives fed by a three-level inverter with low switching frequency,” *IEEE Transactions on Power Electronics*, vol. 38, no. 6, pp. 6841–6850, 2023.

[112] Y. Zhang, Y. Bai, H. Yang, and B. Zhang, “Low switching frequency model predictive control of three-level inverter-fed IM drives with speed-sensorless and field-weakening operations,” *IEEE Transactions on Industrial Electronics*, vol. 66, no. 6, pp. 4262–4272, 2019.

[113] X. Wang, J. Zou, L. Ma, J. Zhao, C. Xie, K. Li, L. Meng, and J. M. Guerrero, “Model predictive control methods of leakage current elimination for a three-level t-type transformerless PV inverter,” *IET Power Electronics*, vol. 11, no. 8, pp. 1492–1498, 2018.

[114] M. L. Parvathy and T. V. Kumar, "An Enhanced Predictive Current Control Scheme for Common Mode Voltage Alleviation and Improvement of Torque Response of PMSM Drive," *IEEE Journal of Emerging and Selected Topics in Power Electronics*, vol. 11, no. 2, pp. 2139-2150, 2023.

[115] C. Zhang, C. Gan, K. Ni, S. Wang, J. Sun, Z. Yu, and R. Qu, “Modelfree predictive voltage control of the floating capacitor in hybridinverter open-

winding permanent magnet synchronous motor,” *IEEE Transactions on Industrial Electronics*, vol. 71, no. 10, pp. 11 925–11 935, 2024.

[116] S. Wang, Y. Zhang, Q. Zhang, J. Zhao, and Q. Zhang, “Model predictive torque control for dual three-phase PMSM based on novel virtual voltage vector,” *IEEE Transactions on Energy Conversion*, vol. 39, no. 3, pp. 1488–1496, 2024.

[117] F. Guo, T. Yang, A. M. Diab, S. S. Yeoh, S. Bozhko, and P. Wheeler, “An enhanced virtual space vector modulation scheme of threelevel NPC converters for more-electric-aircraft applications,” *IEEE Transactions on Industrial Electronics*, vol. 57, no. 5, pp. 5239–5251, 2021.

[118] P. Cortes, M. P. Kazmierkowski, R. M. Kennel, D. E. Quevedo and J. Rodriguez, "Predictive Control in Power Electronics and Drives," *IEEE Transactions on Industrial Electronics*, vol. 55, no. 12, pp. 4312-4324, 2008.

[119] A. R. Beig, G. Narayanan and V. T. Ranganathan, "Modified SVPWM Algorithm for Three Level VSI With Synchronized and Symmetrical Waveforms," *IEEE Transactions on Industrial Electronics*, vol. 54, no. 1, pp. 486-494, 2007.

[120] D. Zhou, C. Jiang, Z. Quan and Y. R. Li, "Vector Shifted Model Predictive Power Control of Three-Level Neutral-Point-Clamped Rectifiers," *IEEE Transactions on Industrial Electronics*, vol. 67, no. 9, pp. 7157-7166, 2020.

[121] C. Liu, X. Xing, C. Du, B. Zhang, C. Zhang and F. Blaabjerg, "An Improved Model Predictive Control Method Using Optimized Voltage Vectors for Vienna Rectifier With Fixed Switching Frequency," *IEEE Transactions on Power Electronics*, vol. 38, no. 1, pp. 358-371, 2023.

[122] S. Yan, Y. Cui and C. Li, "Modulated FCS-MPC Based on Zero-Sequence Component Injection Algorithm and Vector Synthesis Algorithm With NPP Deviation Suppression," *IEEE Transactions on Industrial Electronics*, vol. 71, no. 6, pp. 6095-6106, 2024.